Alma Mater Studiorum – Università di Bologna

School of Science
Department of Physics and Astronomy
Master Degree Programme in Astrophysics and Cosmology

High frequency JVLA observations of the radio mini-halo in the galaxy cluster RBS 797

Graduation Thesis

Presented by:
Alessandra Barba

Supervisor:
Chiar.ma Prof. Annalisa Bonafede
Co-supervisor:
Dott. Francesco Ubertosi

Academic year [2024–2025]
Graduation date [V]

Abstract

Galaxy clusters are the most massive gravitationally bound systems in the Universe and they host both thermal and non-thermal components in the intracluster medium. In relaxed cool-core clusters, a diffuse synchrotron source known as a radio mini-halo is often observed surrounding the central radio galaxy. The physical origin of mini-halos is still debated, and different scenarios involving particle re-acceleration have been proposed.

In this Thesis, we studied the radio mini-halo hosted in the galaxy cluster RBS 797. The cluster is known to host a powerful central Active Galactic Nucleus (AGN), X-ray cavities, and multiple shock fronts produced by the AGN feedback. These properties make RBS 797 an interesting system to investigate the connection between AGN activity and the non-thermal emission observed in the cluster core.

The analysis presented in this work is based on multi-frequency radio observations, combining archival LOFAR data at 144 MHz and JVLA observations at 1.4 GHz, with new high-frequency JVLA data at 5.5 GHz. The central AGN emission was subtracted in the uv-plane in order to isolate the diffuse emission of the mini-halo.

The goal of this work is to investigate the spectral properties of the mini-halo and to constrain the possible mechanisms responsible for the acceleration of relativistic electrons. In particular, the analysis focuses on the possible role of shock fronts generated by AGN activity in re-accelerating particles in the cluster core.

The thesis is organized as follows:

- In Chapter 1, the general properties of galaxy clusters are introduced, including the thermal and non-thermal components of the intracluster medium and the origin of diffuse radio emission in clusters. The different classes of diffuse radio sources are presented, with particular focus on radio mini-halos and on the main scenarios proposed for their origin.

- Chapter 2 introduces the galaxy cluster RBS 797 and summarizes the main results from previous observational studies of the cluster and of its mini-halo.

- Chapter 3 describes the radio datasets used in this work and the procedures adopted for the data reduction. The procedures adopted for imaging of the observations are presented, including the subtraction of the central AGN emission in the uv-plane in order to isolate the diffuse mini-halo emission.

- Chapter 4 presents the scientific analysis of the source. The spectral properties of the mini-halo are studied through an integrated spectral index analysis using the three available frequencies, and through a spatially resolved spectral study based on spectral index maps and radial spectral profiles. In addition, a double-component model is fitted to the brightness distribution in order to investigate the presence of different electron populations contributing to the emission.

- Chapter 5 summarizes the results of this thesis work, and presents a discussion of the interpretations; finally it describes the prospects of possible future progress that can be made on the topic and on the object of study.

Contents

1 Introduction **3**
- 1.1 General properties of galaxy clusters . . . 3
  - 1.1.1 The intracluster medium and thermal emission . . . 5
  - 1.1.2 Cool core clusters and AGN feedback . . . 6
- 1.2 Non-thermal emission in galaxy clusters . . . 9
  - 1.2.1 Synchrotron emission . . . 9
  - 1.2.2 Diffuse radio emission . . . 11
- 1.3 Mini Halos overview . . . 12
  - 1.3.1 Origin of mini-halos . . . 17

2 Scientific Object **21**
- 2.1 The galaxy cluster RBS 797 . . . 21
- 2.2 Instruments overview . . . 25
  - 2.2.1 JVLA . . . 26
  - 2.2.2 JVLA configurations . . . 26
  - 2.2.3 LOFAR . . . 27

3 Data Reduction **28**
- 3.1 Datasets . . . 28
- 3.2 Imaging and *uv* coverage . . . 29
- 3.3 Source subtraction in the *uv*-plane . . . 34

4 Scientific Analysis **40**
- 4.1 Spectral Index fit from integrated flux . . . 40
- 4.2 Spectral index maps . . . 42
- 4.3 Radial spectral profile . . . 46
  - 4.3.1 Separated radial profile for the AGN lobes region . . . 49
- 4.4 Analytic profile: double fit . . . 54
- 4.5 Spectral Index comparison . . . 57
- 4.6 Radiative age constraints . . . 58

5 Conclusions and Future prospects **61**
- 5.1 Conclusions . . . 61
- 5.2 Future prospects . . . 63

A Theory of synchrotron **64**

B Radio telescopes: Single dish and principles of Interferometry **67**
B.1 Single dish response 67
B.1.1 Angular Resolution of Single Dish Telescope 69
B.2 Aperture Synthesis or Interferometry 70
B.2.1 UV-plane and Visibilities 71
B.2.2 Characteristic scales of a multi-element Interferometer 72
B.3 Sensitivity 73

C Basic concepts of Radio Imaging **75**
C.1 Imaging 75
C.1.1 CLEAN algorithm 75
C.1.2 Weighting 78

Chapter 1

Introduction

1.1 General properties of galaxy clusters

Galaxy clusters are the most massive gravitationally bound systems in the Universe; they are made predominantly of dark matter, whose mass fraction is about 75–80%, and baryonic matter bound within a gravitational potential well dominated by dark matter (Kaastra et al., 2008). The baryonic matter is composed of a $\lesssim 20\%$ mass fraction of diffuse hot gas, and a minor fraction ($\sim$ 3–5%) of dust and cold gas locked in stars and galaxies (Diaferio et al., 2008). Galaxy clusters also contain a non-thermal component of cosmic rays and magnetic fields. Figure 1.1 shows images of different components forming the galaxy cluster Abell 2744, presented in the review of Van Weeren et al. (2019).

Galaxy clusters have typical sizes of $1-5$ Mpc, hosting a number of member galaxies that can vary from the hundreds up to the thousands; the characteristic ranges of virial masses for galaxy clusters are $M_{\rm vir} \sim 10^{14}$–$10^{15} M_{\odot}$ with velocity dispersion of the member galaxies that can reach up to $\sigma \sim 1000\,{\rm km/s}$ (Cimatti et al., 2019).

The intracluster medium has typical electron densities around $10^{-3}\,{\rm cm}^{-3}$ and temperatures of 2–10 keV. It emits thermal X-rays primarily via bremsstrahlung (Sarazin, 1986).

More precisely, during the formation of galaxy clusters, the diffuse gas collapses in the potential well of the dark matter and is heated up to a virial temperature of:

$$T_{vir} \sim \frac{\rm GM\,\mu m_p}{\rm kR} \sim 10^8\,{\rm K} \tag{1.1}$$

where M is the total mass, k is the Boltzmann constant, $\mu \sim 0.6$ is the mean molecular weight and R is the virial radius (Gitti et al., 2012). The gas is thus heated to X-ray emitting temperatures and it reaches hydrostatic equilibrium; the X-ray emissivity is proportional to the square of the density of the gas (see Section 1.1.1).

Besides the thermal gas, clusters host relativistic particles and magnetic fields, revealed by diffuse synchrotron emission at radio wavelengths (van Weeren et al., 2019) (see Section 1.2.2).

A central role in galaxy clusters is played by the Brightest Cluster Galaxy (BCG), usually a massive elliptical galaxy located at the centre of the cluster and whose surface brightness in the optical band is the highest of the cluster (the centre of a

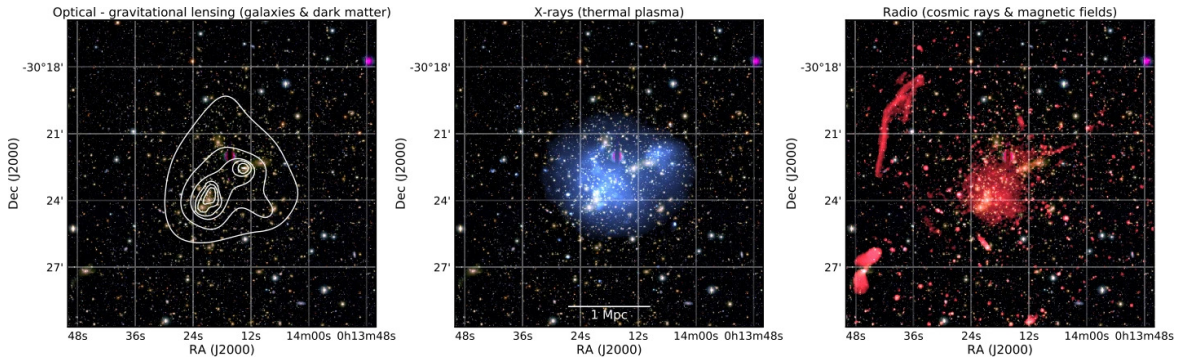

Figure 1.1: Images of the different components observed in the galaxy cluster Abell 2744.
The left panel shows an optical view of the cluster (adapted by Van Weeren et al. (2019) from Medezinski et al. (2016)); the white contours represent the mass surface density derived from a weak lensing study (from Merten et al. (2011); Lotz et al. (2017)).
The middle panel shows the X-ray emission from the thermal ICM (Chandra 0.5–2.0 keV band) in blue.
In the right panel a 1–4 GHz Very Large Array (VLA) image is shown in red, tracing cosmic rays and magnetic fields (Pearce et al., 2017).

cluster generally corresponds to the peak of the gravitational potential well); the BCG is usually also the most massive galaxy of the cluster (Cimatti et al., 2019). Most of relaxed cool-core clusters (which will be explained thoroughly in Section 1.1.2) have a BCG, and it is often a bright radio galaxy, otherwise known as an Active Galactic Nucleus (AGN), a galaxy with a supermassive black hole at its centre that is accreting matter and whose mechanical output produces heating of the surrounding environment (McNamara and Nulsen, 2007; Gitti et al., 2012).

In a subset of clusters the core also hosts a diffuse, steep-spectrum synchrotron source known as a radio mini-halo, the object of study of this thesis, which extends on scales of $\sim$ 100–500 kpc around the central radio galaxy (Gitti, 2016).

The 'centre' of a cluster is not uniquely defined and may depend on the context. Common choices are:

- the peak of the X-ray surface brightness, which traces the densest intracluster gas;
- the minimum of the gravitational potential, inferred from mass modelling or gravitational lensing;
- the position of the BCG.

In relaxed cool-core clusters these definitions usually coincide within a few kpc (McNamara and Nulsen, 2007).

1.1.1 The intracluster medium and thermal emission

A component emitting radiation is defined as thermal if the energy distribution of the particle producing it follows a Maxwellian profile.
This thermal component in galaxy clusters is the hot plasma filling the volume of the cluster, called the Intra Cluster Medium (ICM).

The ICM is a low-density, high-temperature plasma which is approximately in hydrostatic equilibrium within the cluster potential, with typical values of $T \sim 10^8$K and $n_e \sim 10^{-3}\mathrm{cm}^{-3}$ (Sarazin, 1986).

Assuming spherical symmetry and hydrostatic equilibrium, the ICM satisfies the hydrostatic equilibrium equation:

$$\frac{1}{\rho_\mathrm{g}}\frac{\mathrm{d}P}{\mathrm{d}r} = -\frac{GM(<r)}{r^2}, \tag{1.2}$$

where P is the gas pressure, ρ_g the gas mass density and $M(<r)$ the total mass enclosed within radius r (Sarazin, 1986).

Clusters are the most luminous extended X-ray sources in the sky and typical values of X-ray luminosity in the soft X-ray band (0.1–2.4 keV ROSAT) are $L_X \sim 10^{42-43}$ erg/s, corresponding to the values of temperature and number density previously cited.

The origin of the X-ray luminosity was interpreted early on as thermal bremsstrahlung emission from hot plasma, generally described by the following equation:

$$L_x = \int n_e(r) n_{ions}(r) \Lambda[T(r)] d^3r \tag{1.3}$$

with n_e and n_{ions} number density in the ICM and $\Lambda(T)$ is the cooling function of the gas (Diaferio et al., 2008). Figure 1.2 shows the comparison between an optical and an X-ray image of the galaxy cluster Abell 2029; the X-ray luminosity traces mainly the thermal ICM emission.

The frequency-integrated bremsstrahlung emissivity per unit volume can be written as (Sarazin, 1986)

$$\epsilon_{ff} \simeq 1.4 \times 10^{-27}\, Z^2\, n_e\, n_i\, T^{1/2} \quad erg\, s^{-1}\, cm^{-3}, \tag{1.4}$$

where n_i is the ion number density, Z the ionic charge and T the temperature in Kelvin. In practice, the emissivity is often expressed as

$$\epsilon_X = n_e n_i \Lambda(T). \tag{1.5}$$

For $kT \gtrsim 3$ keV, when the ICM is almost fully ionized, bremsstrahlung dominates and $\Lambda(T) \propto T^{1/2}$ (Diaferio et al., 2008), so that $\epsilon_X \propto n_e^2 T^{1/2}$. This strong dependence on n_e^2 explains why X-ray images show centrally peaked surface brightness profiles in clusters with dense cores.

The radiative cooling time of the gas is the ratio between its thermal energy content and its emissivity:

$$t_\mathrm{cool} = \frac{\frac{3}{2}\left(n_\mathrm{e} + n_\mathrm{i}\right) kT}{n_\mathrm{e} n_\mathrm{i}\, \Lambda(T)}. \tag{1.6}$$

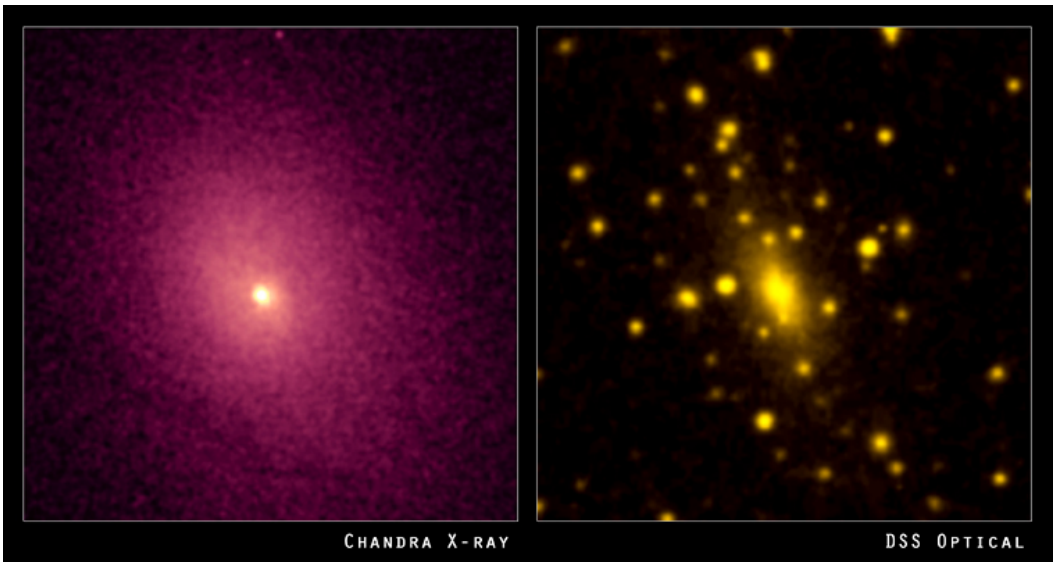

Figure 1.2: Optical and X-ray images of the galaxy cluster Abell 2029. Left panel: X-ray radiation that traces the hot intracluster medium emitting primarily via thermal bremsstrahlung. Right panel: optical image that shows the cluster member galaxies in the same region. Image adapted by Peterson and Fabian (2006) from `http://www.chandra.harvard.edu/` (X-ray: NASA/CXC/UCI/A. Lewis et al. Optical: Pal.Obs. DSS).

Using approximate values appropriate for a fully ionized plasma with cosmic abundances and bremsstrahlung cooling, one obtains the convenient expression (Sarazin, 1986)

$$t_{\rm cool} \simeq 8.5 \times 10^{10}\ {\rm yr} \left(\frac{n_{\rm e}}{10^{-3}\,{\rm cm}^{-3}}\right)^{-1} \left(\frac{T}{10^{8}\,{\rm K}}\right)^{1/2}. \tag{1.7}$$

The radius within which the cooling time is $t_{\rm cool} \lesssim 10^{10}\,{\rm yr}$ is called the cooling radius $r_{\rm cool}$ (Peterson and Fabian, 2006).

1.1.2 Cool core clusters and AGN feedback

Some galaxy clusters have a peculiar feature: a cool core. The ICM in their centres is cooler than the rest of the cluster, it is denser and therefore according to 1.6 it cools faster. Corresponding to the densest regions at the very centre, there is the peak of the X-ray emission according to 1.4. In typical cool-core clusters the cooling radius is of the order of $r_{\rm cool} \sim 50$–$150\,{\rm kpc}$, with the cooling time approaching values below $5 \times 10^{8}\,{\rm yr}$ (Peterson and Fabian, 2006; Hudson et al., 2010).

In principle, the presence of this cool core would lead to what is known as a *cooling flow*, a flow of gas headed towards the centre of the cluster, which would consequently become denser and denser. In the explanation of this phenomenon from Fabian et al. (1991), the flow takes place because the gas density has to rise to support the weight of the overlying gas, so it is essentially pressure-driven: the gas pressure at r_{cool} is determined by the weight of the overlying gas, in which cooling is not important. Within r_{cool}, cooling reduces the gas temperature and so the gas density must rise in order

to maintain the pressure, therefore the only way for the density to rise is for the gas to flow inward (Fabian et al., 1991). Assuming steady-state cooling under isobaric conditions, the X-ray luminosity from the cooling region $L_{\rm cool}$ would lead to mass deposition rates of $\dot{M} \sim 100$–$1000\ M_{\odot}\,{\rm yr}^{-1}$. This enormous implied mass deposition has not been observed in cooled form (the 'mass sink' problem), and many observations of BCGs showed total star formation rates and gas mass fractions one or two orders of magnitude below such a large value; additionally, a simple cooling flow spectrum had proven to be a poor fit to the data in the soft X-ray band (Peterson and Fabian, 2006). These discrepancies between model predictions and observations became known as the *cooling flow problem*, indicating that the model was an oversimplification of what happens in cool cores.

Competing heating processes are therefore required to keep the balance with the cooling within the central region and to quench the star formation activity, keeping the cool-cores stable. Today, the main known heating cause is the central AGN feedback: indeed the majority of cool-core clusters host active galactic nuclei in the centre; it was already known from the early 90s that central dominant galaxies of cool-core clusters have a high incidence of radio activity, showing the presence of central FR-I radio galaxies in 70% of the cases (Burns, 1990). Added to that, turbulence and sloshing motions are thought to contribute in keeping the cool core stable without triggering excessive star-formation (McDonald et al., 2018).

The importance of radio galaxies in cool cores began to emerge after the discovery, with the X-ray satellite ROSAT, of deficits in the X-ray emission of the Perseus and Cygnus A clusters, which were spatially coincident with regions of enhanced synchrotron emission, the so-called X-ray cavities: these are produced by the flowing of gas into the central regions of the cluster, which powers the AGN that then heats the surrounding ICM, without destroying the cool-core. This heating is often due to energetic outflows in the form of radio jets which inflate the observed cavities.

It became therefore clear that the central radio sources have a profound, persistent effect on the ICM and it was deemed crucial to study the link between the AGN feedback, the thermal component of the intracluster gas and the non-thermal diffuse emission found in cool-core clusters (for related reviews, see, e.g.,Gitti et al. 2012; McNamara and Nulsen 2012; Eckert et al. 2021).

The key features of cool core clusters are the following:

- The drop of the temperature profile in the centre compared to the other regions of the cluster, corresponding to higher density profiles.
- Very recognisable features in the X-ray emission ascribable to the central AGN activity, such as ripples and shocks in the gas and cavities.
- Their usually smooth and symmetric profiles that indicate that the clusters haven't recently undergone major mergers.

To segregate between cool core and non-cool-core clusters the central cooling time, t_{cool}, is usually the preferred parameter for low redshift clusters (Hudson et al., 2010); modern X-ray studies distinguish between *cool–core* (CC) clusters, where the central

cooling time is short, and *non–cool–core* (NCC) clusters, where the core is hotter and less dense. CC clusters show sharply peaked X-ray surface brightness profiles, significant central drops in temperature (by factors of $\sim$ 2–3), high central densities and often bright central radio sources and optical line emission; non-cool-core clusters have flatter profiles and are more frequently undergoing major mergers (Peterson and Fabian, 2006).

Another quantity used to describe galaxy clusters is the radial entropy profile, defined as $K(r) = kT_X(r)\, n_e(r)^{-2/3}$ (Cavagnolo et al., 2009) where $T_X(r)$ and $n_e(r)^{-2/3}$ are the temperature and density profiles, respectively. Given a model for the entropy profile such as $(r) = K_0 + K_{100}(r/100kpc)^{\alpha}$, K_0 is what is known as the *core entropy*, and it is an additional quantity that provides as a useful diagnostic tool (Cavagnolo et al., 2009). Hudson et al. (2010) report a division between the two subgroups at $K_0 \sim 25\,\mathrm{keV\ cm^2}$.

Mechanical AGN feedback

High resolution X-ray images revealed deficits in the surface brightness of many cool-core clusters coincident with the radio lobes of the central AGN. These X-ray cavities are interpreted as bubbles of relativistic plasma inflated by radio jets (Gitti et al., 2012). The heating is thought to occur through the dissipation of the cavity enthalpy and through shocks driven by the AGN outburst; the energy required to create a cavity with pressure p and volume V is the sum of the pV (work done by the jet to displace the X-ray emitting gas while it inflates the radio bubble) and the internal energy of the lobes, that is, the enthalpy given by:

$$E_{cav} \simeq \frac{\gamma}{\gamma - 1} pV \approx 4pV \tag{1.8}$$

where γ is the ratio of the specific heats of the cavity content (for a relativistic plasma $\gamma = 4/3$); when divided by the cavity age, t_{cav}, the observational measurements give an estimate of the so-called 'cavity power', P_{cav} (Gitti et al., 2012) .

Systematic studies of samples of clusters show that P_{cav} is typically comparable to, and often exceeds, the X-ray cooling luminosity of the core L_{cool}. This demonstrates that AGN mechanical feedback can in principle balance radiative cooling.

Additional energy channels include weak shocks and sound waves driven by the expanding bubbles, which can dissipate and heat the ICM on larger scales; these bubbles in the hot gas appear to be inflated by the radio jets of the AGN itself (Gitti et al., 2012; McDonald et al., 2018). Figure 1.3 (from Gitti et al. 2012), is a perfect visual example of the radio emission filling the regions of emission deficit in the X-ray.

These observations have led to a picture in which cool-core clusters undergo a self-regulated feedback cycle: cooling of the ICM promotes accretion onto the central supermassive black hole, triggering a radio-loud AGN outburst; jets inflate bubbles and cavities, driving shocks and turbulence that heat the gas and reduce the cooling rate; once the gas is stabilized, accretion declines and the AGN activity fades, until cooling again becomes important (Gitti et al., 2012).

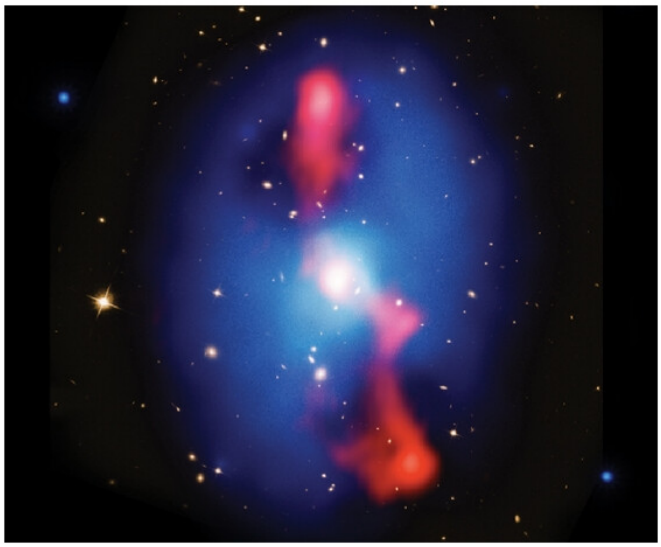

Figure 1.3: Composite image of the galaxy cluster MS0735 + 7421. Chandra X-ray image (blue) and Very Large Array 330 MHz radio image (red) are superposed with the Hubble Space Telescope optical image of the cluster. The giant X-ray cavities visible as deficit in the (blue) thermal emission are filled with radio emission (red), and they are surrounded by a cocoon shock visible in the Chandra image as an elliptical edge. The image has a size of roughly 800 kpc by 800 kpc. Credit: (Gitti et al., 2012).

1.2 Non-thermal emission in galaxy clusters

Galaxy clusters also host a non-thermal component in addition to the hot thermal ICM. Observations at radio wavelengths reveal the presence of relativistic particles known as Cosmic Rays (CR), and large scale magnetic fields filling the whole volume of clusters. These electrons are relativistic, with typical Lorentz factors $\gamma \gtrsim 10^3$–10^4, and they are accelerated by cluster magnetic field lines, emitting synchrotron radiation. The result is diffuse radio emission that can extend on scales from a few hundred kiloparsecs up to megaparsec scales (Feretti et al., 2012; Van Weeren et al., 2019).

1.2.1 Synchrotron emission

The total emission produced by a population of relativistic electrons has the shape of a power law such as

$$J_s \propto \nu^{-(\delta-1)/2} = \nu^{-\alpha} \tag{1.9}$$

with α known as the spectral index, defined as $\alpha = \dfrac{\delta - 1}{2}$ (detailed explanation of the theory of synchrotron emission can be found in Appendix A). The most frequent value observed in radiosources is $\alpha \sim 0.75$ ($\delta = 2.5$) (Fanti and Fanti, 2012)

Radiative losses and spectral break

The energy spectrum of a radiosource can show an evolution in time if processes of radiative losses are present. The most observed feature is what's called a 'break' in the power-law profile observed at a characteristic frequency called ν_{break}: in the range of frequencies below ν_b the spectrum remains unchanged, while above ν_b the radiative losses bring the profile rapidly to zero therefore having a much steeper spectral index in that range (Fanti and Fanti, 2012).

The radiative losses that produce the steepening of the spectral index are indicative of the ageing of the emitting particles: if cosmic rays are produced in a single event with a power law energy distribution

$$N(E)dE = N_0 E^{-\delta} dE \tag{1.10}$$

following the emergence of electrons from their sources (or acceleration sites), their spectrum steepens as result of high energy electrons having a shorter radiative lifetime (Ferrari et al., 2008).

The more time passes, the more radiative losses the radiosource is subject to, the more the break is shifted at lower values of energy and lower values of frequency.
The value of ν_{break} defined as the frequency at which the steepening of the spectral index is observed is therefore related to the radiative age of a radiosource, given a known value of the magnetic field $H(\mu G)$, as in the following equation (Fanti and Fanti, 2012):

$$\nu_{break} \approx 2.56 \times 10^{18} (H/\mu G)^{-3} (t/yrs)^{-2} \tag{1.11}$$

$$t \propto \frac{H^{1/2}}{H^2 + 8\pi u_f} \nu^{-1/2} (yrs) \tag{1.12}$$

where u_f is the photon energy density responsible for Inverse Compton losses.

Diffusion problem

Relativistic electrons loose energy via synchrotron radiation and Inverse Compton (IC) scattering off the cosmic microwave background (CMB).

The combined synchrotron plus IC loss time for an electron radiating at frequency ν is (Brunetti and Jones, 2014)

$$t_{rad} \simeq 1.3 \times 10^8 (yr) \left(\frac{B_{eff}}{5\,\mu G} \right)^{-3/2} \left(\frac{\nu}{1\,GHz} \right)^{-1/2}, \tag{1.13}$$

where $B_{eff}^2 = B^2 + B_{CMB}^2$ and $B_{CMB} \simeq 3.2(1+z)^2\,\mu G$ is the equivalent magnetic field of the CMB. For typical cluster conditions this leads to $t_{rad} \sim 10^8\ yr$ or less for electrons emitting at the GHz frequencies. Since this is much shorter than the time required for electrons to diffuse over scales of $\gtrsim$ 100Kpc, the diffuse radio emission observed in clusters cannot be explained by simple diffusion of electrons from a central AGN: in-situ (re)acceleration and/or continuous injection throughout the emitting volume is required. This is the so called *slow-diffusion problem* (Brunetti and Jones, 2014; van Weeren et al., 2019).

1.2.2 Diffuse radio emission

The first detection of diffuse and extended radio emission in galaxy clusters dates back to 1959, when Large et al. (1959) mapped for the first time the Coma cluster at radio wavelengths, detecting an extended radio source (Coma C) at its centre (Ferrari et al., 2008).

As of today we understand that the ICM contains a non-thermal component of CR which is not directly associated with cluster radio galaxies (Large et al., 1959): these GeV CR electrons (with Lorentz factors of $\gamma > 10^4$) emit synchrotron radiation in the presence of ICM magnetic fields of the order of $\sim \mu$Gauss (van Weeren et al., 2019).

There are several physical mechanisms that could in principle accelerate or re-accelerate electrons in the ICM, and produce the CR electrons emitting synchrotron, that will be briefly summarized as follows (detailed description of the processes relevant to mini-halos origin will be given in Section 1.3.1):

- First order Fermi acceleration (Fermi-I): this process is also known as diffusive shock acceleration (DSA)(Krymskii, 1977; Axford et al., 1977; Bell, 1978a,b; Blandford and Ostriker, 1978; Drury, 1983; Blandford and Eichler, 1987; Malkov and Drury, 2001), and it consists of particles accelerated diffusively by a shock, crossing back and forth the shock front as they scatter from magnetic inhomogeneities in the downstream and upstream regions of the shock. At each crossing, particles gain additional energy, forming a power-law energy distribution of CR.

- Second order Fermi acceleration (Fermi-II): it is a stochastic process where particles scatter from magnetic inhomogeneities, for example from magneto-hydrodynamical (MHD) turbulence (Schlickeiser et al., 1987; Schlickeiser and Achatz, 1993; Brunetti et al., 2001; Petrosian, 2001). Particles can either gain or lose energy when scattering and because of its random nature, second-order Fermi acceleration is an inefficient process.

- Adiabatic compression: 'old' relativistic radio plasma already present in the region from an AGN is adiabatically compressed by a shock wave, and due to the compression, the CR electrons regain energy boosting the radio synchrotron emission (Enßlin and Gopal-Krishna, 2001; Enßlin and Brüggen, 2002).

- Secondary models: the CR electrons are produced as secondary particles, namely products of decay of other particles, such as the hadronic model, where the secondary CR electrons are produced by collisions between relativistic protons and the thermal ions (Dennison, 1980; Blasi and Colafrancesco, 1999; Dolag and Enßlin, 2000; Miniati et al., 2001; Keshet and Loeb, 2010; Donnert et al., 2010; Enßlin et al., 2011).

Diffuse radio sources in galaxy clusters have historically been divided into three main classes: radio-halos, relics, and mini-halos (van Weeren et al., 2019).

Radio-halos are a kind of diffuse emission on the Mpc-scale usually found in the central regions of clusters with a quite regular morphology, steep spectrum $\alpha \sim 1 - 2$ and lack of observed polarization; they are usually found in clusters that show signatures of a disturbed dynamical state and without a cooling core

(Ferrari et al., 2008). Another property of the radio-halo class is that particle (re-)acceleration (or production) occurs throughout a significant volume of the cluster and is not associated with a particular shock whose location can be pin-pointed; therefore the plausible interpretation of the origin of these sources should be Fermi-II processes and/or secondary electrons (van Weeren et al., 2019).

Relics are an arc-like shaped emission found at the outskirts of clusters, with steep spectrum values $\alpha \gtrsim 1$ (Ferrari et al., 2008) and high values of polarization fraction (20–60% van Weeren et al. 2019); their elongated morphology traces particles that are (re-)accelerated by shock waves (van Weeren et al., 2019); this kind of emission is also found commonly in merging clusters (Ferrari et al., 2008).

Mini-halos are the kind of emission investigated in this thesis work, they differ from the above described radio-halos not only for their sizes as the name suggests, but more importantly for the properties of their host clusters: they are found in the centre of non-merging cool-core clusters and extended on quite small scales (few 100 kpc, comparable to the size of the cooling region) around powerful radio-galaxies (Ferrari et al., 2008); they also have steep spectrum values $\alpha \sim 1 - 1.3$.

1.3 Mini Halos overview

Mini Halos are a kind of non-thermal emission found in relaxed cool-core clusters, located in the centre of such clusters and usually surrounding an AGN. Figure 1.4 shows examples of mini-halos found in cool-core galaxy clusters, precisely RXJ 1347.5–1145 and the Perseus cluster.

No mini-halos have ever been found in non-cool-core (merging or disturbed) clusters, indicating a strong association with this population of clusters. Indeed, observational surveys like the one of Giacintucci et al. (2017) found that for clusters above $M_{500} \sim 6 \times 10^{14} M_{\odot}$, almost all galaxies with a cool core ($\sim 80\%$) host a radio mini-halo. The existence of mini-halos is therefore evidently tied to the presence of a cooling core. Another positive correlation observed is the one between mini-halo radio power and the cluster's X-ray luminosity: more massive, more luminous cool-core clusters tend to host the more powerful mini halos, like for example the RX J1347.5–1145 cluster or the Phoenix cluster (van Weeren et al., 2019).

Due to the combination of small angular size and the bright radio emission of the central radio galaxy, the detection of a mini-halo requires high resolution and high dynamic range, making its detection complicated (Murgia et al., 2009). The classification of a mini-halo is also difficult without X-ray data, therefore mini-halo detection is limited by observational biases: a bright central radio source can outshine the faint mini-halo, and only with high-dynamic-range radio images can the mini-halo be isolated. The work of Ignesti et al. (2020), for example, analysed a sample of mini-halos comparing the non-thermal emission with the X-ray luminosity, to better constrain the

origin scenario. Over the past decade, the number of known mini-halos has steadily grown, from a dozen or so to a few dozen confirmed cases, thanks to improved radio facilities (GMRT, JVLA, LOFAR, MeerKAT) targeting cluster cores.

The emission of mini-halos is not always uniform, and they often show filamentary or clumpy features. For example, the mini-halo in the Perseus Cluster, considered the prototypical mini-halo, contains multiple radial filaments and irregular shapes detected at low frequencies, as can be seen in Figure 1.4a

These structures tend to follow certain ICM features: notably, mini-halo emission is often bounded by or confined within X-ray cold fronts (sharp density discontinuities from sloshing cool gas). In Perseus, for instance, the radio mini-halo is mostly enclosed by cold fronts, with only faint 'leakage' of radio emission beyond them: this suggests that the dynamic of the ICM strongly influences the shape and extent of the mini-halo (van Weeren et al., 2019).

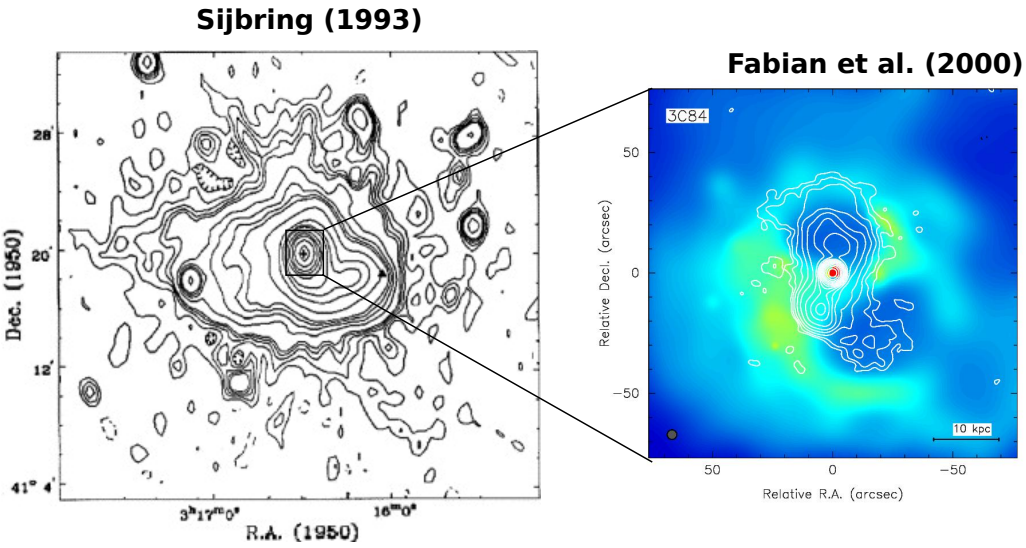

(a)

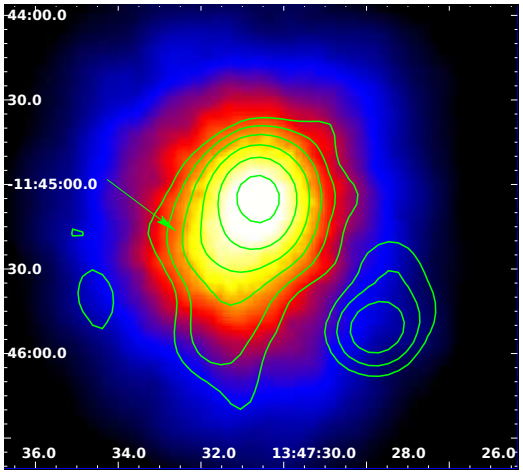

(b)

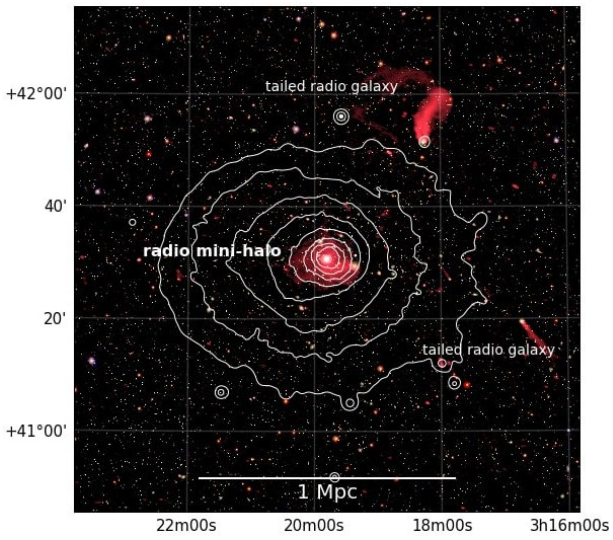

(c)

Figure 1.4: Examples of radio mini-halos in galaxy clusters. **(a)** 327 MHz map of the Perseus mini-halo centred on NGC 1275, with radio contours overlaid on the central X-ray emission (adapted by Feretti et al. (2012); originally based on Sijbring (1993) and Fabian (1994b)). **(b)** 1.4 GHz radio contours of the mini-halo in RXJ 1347.5–1145 superimposed on the XMM-Newton image (adapted by Feretti et al. (2012); originally from Gitti et al. (2007)). **(c)** VLA 230–470 MHz image of the relaxed Perseus cluster with XMM-Newton X-ray contours overlaid; the system hosts a radio mini-halo and prominent tailed radio galaxies (adapted by Van Weeren et al. (2019); originally from Gendron-Marsolais et al. (2017)).

Mini-halos show similarities with radio halos, such as the position in the central areas of their host clusters, low surface brightness and a steep spectrum, but also significant differences: one relevant difference being that mini-halos are detected only

in relaxed, cool-core clusters where recent major merger activity has not taken place (Feretti et al., 2012).

Mini-halos usually do not extend much further from the dominant radio galaxy at the cluster centre, or from the cooling region, reaching scales of $\simeq 500kpc$. The Perseus mini-halo is one of the largest (fig. 1.4c), reaching $\sim$ 300–400 kpc across (Gendron-Marsolais et al., 2017); its maximum extension, about 1.3 million light-years, is ten times the Milky Way's size [1].

The radio power of mini-halos at 1.4 GHz ranges from $P_{1.4} \sim 10^{23}$ to $10^{25}W/Hz$, slightly lower than giant radio halos (van Weeren et al., 2019).

In mini-halos the non-thermal emission, originated from relativistic particles accelerated by magnetic fields, is considered to be deeply mixed with the thermal component of the intracluster gas: in fact radio sources in which the ambient thermal medium is clearly separated from the non-thermal plasma (such as radio bubbles related to AGN activity) are by definition not to be considered mini-halos (Feretti et al., 2012).

In several well-studied cases of mini-halos in cool core clusters, the spectrum is a power-law with no strong curvature across the GHz range. However, there are hints of spectral steepening at higher frequencies or toward halo edges in some clusters: a radial spectral steepening (spectral index becoming more negative with radius) was reported in the Ophiuchus cluster; the core of the mini-halo has a flatter spectrum than the outer parts. This was quantified by Murgia et al. (2009) who found the spectrum in Ophiuchus steepens with radius, consistent with aging of cosmic-ray electrons as they diffuse outward; this is also true for the work done by Giacintucci et al. (2014a) studiyng the galaxy cluster RXJ1720.1 + 2638, that showed that the spectrum of the diffuse emission of the mini-halos steepened with increasing distance from the centre, and the work of Riseley et al. (2022). Images 1.5 and 1.6 show the spectral index maps produced in the works of Giacintucci et al. (2017) and Riseley et al. (2022) respectively.

[1] VLA Gives New Insight Into Galaxy Cluster's Spectacular "Mini-Halo" - National Radio Astronomy Observatory: `https://public.nrao.edu/news/galaxy-cluster-mini-halo/`

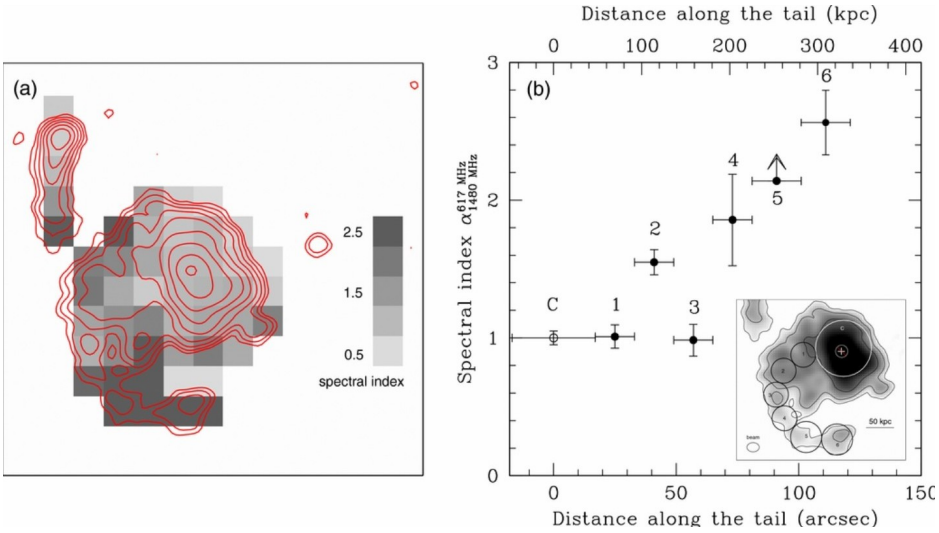

Figure 1.5: Panel (a) Spectral index map of the minihalo in RXJ1720.1 + 2638, comparing a pair of images at 617 MHz and 1.48 GHz.The image has been computed from images with similar noise (30 μJybeam^{-1}) and the same UV-range and restoring beam of $8'' \times 6''$. Overlaid are radio contours at 617 MHz.
Panel (b): spectral index between 617 MHz and 1480 MHz as a function of the distance from the cluster centre (white cross) along the mini-halo tail (black, filled points). Credit: Giacintucci et al. (2017)

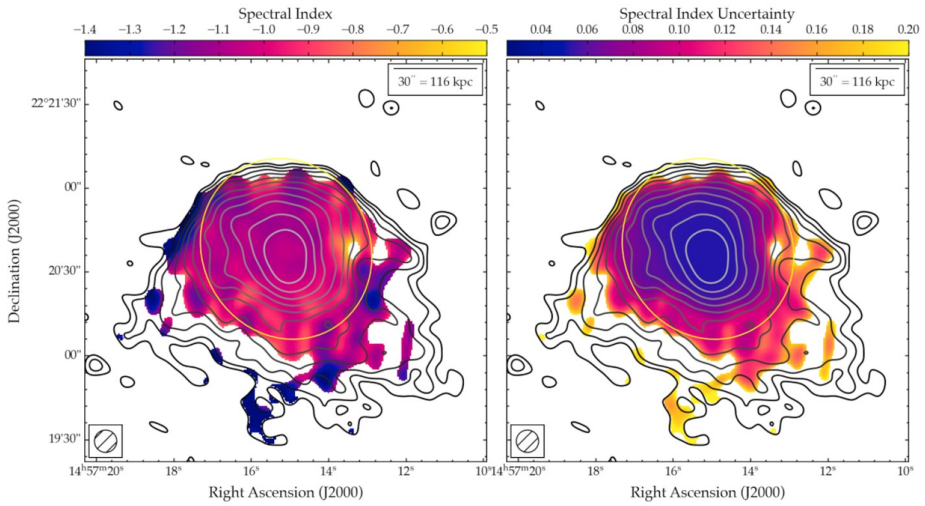

Figure 1.6: Spectral index map (left) and associated uncertainty (right) of the mini-halo in MS 1455.0 + 2232 at a resolution of 8 arcsec (top) and 15 arcsec (bottom), derived using our MeerKAT (1283 MHz) and LOFAR (145 MHz) data. Contours show MeerKAT surface brightness at 1283 MHz. Pixels below 3σ in each radio image are blanked. The yellow ellipse traces the outer boundary of the sloshing spiral. Credit: Riseley et al. (2022).

On the other hand, an inverse trend was observed in a few cases: notably, the mini-halo in RBS 797 shows a spectral index flattening with radius – from $\alpha \approx -1.1$ at the center to about –0.7 in outer regions $\sim$ 100 kpc out (Bonafede et al., 2023).

This unusual hardening of the spectrum outward (opposite to the expected aging) was attributed to shock re-acceleration (see Section 2.1).

As of 2025, no significant polarized emission had been detected from the majority of mini-halos observed as they appear largely unpolarized, likely due to tangled magnetic fields and Faraday depolarization in cluster cores. The only exception seems to be the work of Gitti et al. (2006) on RBS 797 which reported the detection of polarized emission at 1.425 GHz in a region extending up to $10'' \times 15''$ from the centre of the cluster; Bonafede et al. (2023) re-imaged the data at the same frequency after subtracting the central AGN emission but the results were just above the 2σ noise level and therefore not conclusive.

Despite of their differences, it is possible that mini-halos and giant halos in clusters are physically related to each other. For example, cluster merger events could transport CR from cluster cores to larger-scales where they are re-accelerated again as seen in Brunetti and Jones (2014). This could lead to "intermediate" cases where mini-halos could evolve into giant radio halos and vice-versa, or a giant radio halo and mini halo could co-exist. A situation possibly of this kind has been found in the cluster RX J1720.1 + 2638, where Savini et al. (2019) discovered extended faint diffuse steep spectrum emission beyond the cold front and mini-halo region. Similar hybrid systems have also been identified in a recent LOFAR study (Biava et al., 2024), such as the cluster *A*1068, PSZ1G139.61 + 24, MS 1455.0 + 2232, and RX J1720.1 + 2638; these systems show a central mini-halo confined by cold fronts coexisting with larger-scale diffuse emission.

Since different characteristics are observed between merging and cool core clusters and the diffuse radio emission in them, the comparison between these systems' properties may help in understanding if the origin of the radio emission is related to different physical processes (Murgia et al., 2009).

1.3.1 Origin of mini-halos

As explained in Section 1.2.1 the radiative lifetime of the electrons injected by the AGN results shorter then the time necessery for the mini-halo to reach the external region, therefore some (re-)accelleration or an in situ production process must be in place.

So far, of the acceleration processes that have been previously mentioned, two broad classes of models have been proposed to explain the emission of mini-halos: hadronic or secondary models (Pfrommer and Ensslin, 2004) and leptonic or re-acceleration models (e.g Gitti et al. 2002; ZuHone et al. 2013).

Hadronic models describe the formation of the electrons that produce the synchrotron emission as a product of the decay from the inelastic collision of thermal and cosmic ray protons. Leptonic models, on the other hand, describe an *in-situ* re-acceleration of seed relativistic electrons.

Hadronic scenario In the hadronic scenario, cosmic-ray protons (CRp) continuously collide with the dense thermal protons in the cluster core and produce charged pion secondaries that decay into relativistic electrons and positrons. These secondary

electrons then emit the observed radio synchrotron. This model naturally provides a sustained supply of fresh electrons as long as a sufficient population of CRp is present in the ICM. The central idea is that cluster cool cores might accumulate cosmic-ray protons (injected e.g. by the central AGN over time or by past minor mergers), and those CRp produce a pervasive "sea" of secondary electrons. Because the target gas density in cool cores is high, the hadronic interaction rate is higher in core regions, yielding radio emission concentrated in the core, qualitatively consistent with mini-halo extents (van Weeren et al., 2019). In many clusters the hadronic model struggles: to explain the observed radio power, a very high energy density of CRp would be needed, often in tension with gamma-ray bounds or with the idea that CRp pressure cannot greatly exceed thermal pressure without affecting the cool core stability. Thus, a pure hadronic scenario is considered disfavored or at least not universal, especially if mini-halo spectra show cutoffs (hadronic models continuously inject electrons of all energies and predict a pure power-law spectrum).

Leptonic scenario In the leptonic or re-acceleration models, the relativistic electrons responsible for the synchrotron emission are re-accelerated *in situ*; the source of the re-acceleration can be turbulence in the cool-core region, likely the sloshing of the core gas, (i.e. oscillatory motions induced by minor mergers), or the feedback from the central AGN (Gitti et al., 2002). Gas sloshing naturally occurs in cool cores and creates the observed cold fronts; simulations show that these motions can stochastically accelerate particles. In this scenario, a population of seed relativistic electrons is required; these particles may originate from past activity of the central AGN or from other acceleration processes in the ICM. The model proposed by Gitti et al. (2002) for the Perseus cluster suggests that these seed electrons are re-accelerated by magneto-hydrodynamic (MHD) turbulence in the cool core. This re-acceleration can extend the radiative lifetime of the electrons; without any re-acceleration mechanism at work, the emission of these electrons in the radio band should not be observable for more than $\sim 10^8$ yr (Gitti et al., 2002). This short lifetime contrasts with the diffuse radio emission observed. This stochastic acceleration process is often described as second-order Fermi acceleration, a mechanism where particles gain energy through repeated interactions with moving magnetic irregularities in the turbulent medium. Several observational arguments support the turbulent re-acceleration scenario. The first is the observed spatial correlation with cold fronts: many mini-halos are bounded by cold fronts, a feature naturally explained if turbulence inside the cold-front region accelerates electrons and cannot propagate beyond the front. The second is the requirement of in-situ acceleration: the electron radiative lifespan in clusters ($\sim 10^8$ years) as previously mentioned is much shorter than the diffusion time across 100–200 kpc, thus the electrons radiating in a mini halo must be accelerated near where they are observed (Gitti et al., 2002). The third is spectral curvature: stochastic acceleration leads to a steady-state electron spectrum with a high-energy cutoff, which translates to a break in the radio spectrum (steepening at high frequencies) (Brunetti et al., 2001).

So far, a few mini-halos show hints of high-frequency steepening (e.g. RXJ1720.1+2638 Giacintucci et al. 2014b). However, the available data are still limited and no general conclusion has been reached. The central AGN likely provides the population of

seed relativistic electrons through past radio jets or lobes that deposit fossil electrons in the cluster core. These particles may have energies too low to emit observable synchrotron radiation, but they can be re-energized by turbulence to reach the GeV energies required to produce the observed radio emission. The presence of a powerful radio AGN in the centre of most mini-halo clusters is consistent with this scenario. Numerical simulations also support this picture. In particular, the simulations by ZuHone et al. (2013, 2015) show that sloshing motions in cool-core clusters can re-accelerate a population of seed electrons and reproduce radio structures similar to observed mini-halos that are confined by cold fronts. Figure 1.7 shows the results of the work of ZuHone et al. (2013): the first panel shows an image of the cluster RXJ1720.1 + 26 (one of the clusters exhibiting a sloshing core and a mini-halo), with 610 MHz radio contours overlaid on the Chandra X-ray image. Panel (b) shows the results of the simulation: the produced images represent the projected gas temperature with radio brightness contours overlaid. From these maps, it can be seen that the radio emission at lower frequencies persists over a longer period and is bounded by the core cold fronts, while the emission at $\nu = 1.4$ GHz becomes dimmer and more patchy (ZuHone et al., 2013). From the comparison, it is evident that the simulation reproduces the observed features very well.

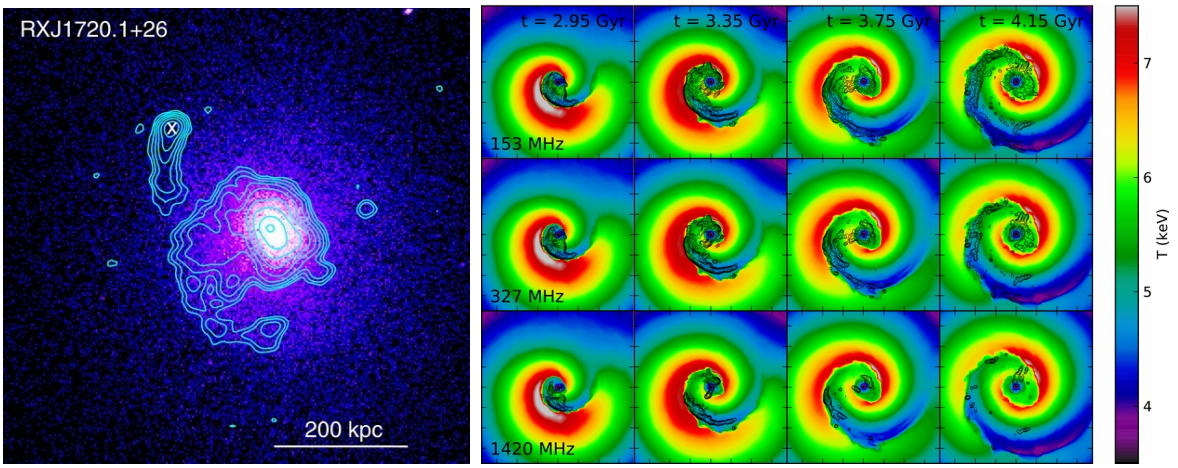

(a) (b)

Figure 1.7: Connection between radio mini-halos and cold fronts in galaxy clusters, illustrated through observations and numerical simulations (ZuHone et al., 2013).
(a): Chandra X-ray image of RXJ 1720.1+26 with 610 MHz radio contours overlaid. Contours start from 3σ and are spaced by factor two, ($\sigma = 30\mu$Jy/beam and beam size $8'' \times 6''$. The white cross marks an unrelated head–tail radio source. The mini-halo radio emission is confined within the cold fronts, visible as brightness edges in the X-ray image. Adapted by ZuHone et al. (2013) from Giacintucci et al. (2014b).
(b) Projected gas temperature maps from simulations with radio brightness contours overlaid at several epochs; simulation performed for observing frequencies of 153, 327, and 1420 MHz. The colour scale represents the gas temperature (keV). The maps show that lower-frequency emission persists for longer times and remains bounded by the cold fronts visible in the temperature structure, while the 1.4 GHz emission becomes dimmer, more patchy, and occupies a smaller projected area. Credit:ZuHone et al. (2013). Each panel is 750 kpc on a side with tick marks corresponding to 100 kpc.

Relevant for this case study is also the mechanism of particle acceleration by shocks, usually described by first-order Fermi acceleration also known as diffusive shock acceleration (DSA). In this process particles gain energy by repeatedly crossing the shock front and scattering off magnetic irregularities on both sides of the shock, producing a power-law distribution of particle energies $N(E) \propto E^{-\delta}$ (Krymskii, 1977; Axford et al., 1977; Bell, 1978a,b; Blandford and Ostriker, 1978; Drury, 1983; Blandford and Eichler, 1987; Malkov and Drury, 2001). The change of momentum associated with the crossing of the shock is

$$\Delta p \approx \frac{p\,(u_- - u_+)}{v} \tag{1.14}$$

where u_- and u_+ are the upstream and downstream flow velocities in the shock rest frame and v is the particle velocity (Blandford and Eichler, 1987). The resulting synchrotron spectral index is related to the particle index through $\alpha = (\delta - 1)/2$, and in the case of diffusive shock acceleration the slope δ depends on the Mach number M of the shock, and can be expressed as

$$\delta = \frac{3(\gamma + 1)M^2}{2(M^2 - 1)} = \frac{4M^2}{M^2 - 1} \tag{1.15}$$

where the second equality holds for $\gamma = 5/3$, the usual assumption in astrophysical shocks (Blandford and Eichler, 1987). This relation implies that stronger shocks produce flatter radio spectra, while weaker shocks result in steeper spectra.

In Richard-Laferrière et al. (2020) it is suggested that AGN feedback may be one of the dominant mechanisms responsible for the origin of radio mini-halos, as it can inject energy into the ICM and re-accelerate an existing population of relativistic particles, while sloshing motions may influence the overall morphology of mini-halos within cold fronts.

More recent works such as Riseley et al. (2022) point out to the incompleteness of the two models and their inability, taken in their individual simplest versions, to describe the observed phenomena thoroughly. In particular, spatially resolved spectral studies suggest that a combination of mechanisms may be required, where turbulence driven by gas sloshing re-accelerates relativistic electrons while AGN activity provides a reservoir of seed particles and energy injection into the core region. This hybrid scenario is consistent with the numerical simulations where sloshing-induced turbulence re-accelerates the particles, such as those by ZuHone et al. (2013, 2015).

Chapter 2

Scientific Object

2.1 The galaxy cluster RBS 797

In this thesis we analysed the mini-halo found in the centre of the cluster of galaxies named RBS 797.
The first evidence of X-ray cavities in RBS 797 was found by Chandra observation by Schindler et al. (2001), with a diameter of $\sim$ 20kpc, suggesting an interaction between the central AGN and the surrounding ICM. Other more recent works have given us an in-depth overview of many RBS 797 characteristics (Schindler et al., 2001; Gitti et al., 2006; Doria et al., 2012; Ubertosi et al., 2023; Bonafede et al., 2023): it is a massive cool-core cluster hosting a radio mini-halo and a powerful AGN in its centre.

In Table 2.1 the main properties of the cluster are shown. The cosmology assumed is $H_0 = 70 kms^{-1}Mpc^{-1}$, $\Omega_m = 0.3$, $\Omega_\lambda = 0.7$ corresponding to a conversion factor of $1'' = 4.9\,\mathrm{kpc}$.

The activity of the central AGN has been studied in many researches such as Gitti et al. (2006, 2012); Doria et al. (2012); Ubertosi et al. (2024), showing two pairs of jets oriented orthogonally with respect to each other, one main pair in the east-west direction and one in the north-south direction; observations done with Chandra (Ubertosi et al., 2021) have shown that both pairs of jets and corresponding lobes are co-spatial with X-ray cavities, making this cluster the only known so far with four equidistant radio-filled X-Ray cavities (Bonafede et al., 2023). The observations in the X-Ray have shown the presence of three pairs of slightly elliptical concentric shock fronts likely produced by the AGN feedback activity. In Table 2.2 the projected distances and angular ranges of the shock fronts are shown, as detected in Ubertosi et al. (2023). Figure 2.1 shows the projected shocks and the related discontinuities in the ICM.

Table 2.1: Main characteristics of RBS 797

RA (J2000)	Dec (J2000)	z	M_{500} ($10^{14} M_{\odot}$)
09h47m13.0s	+76d23m14s	0.354	5.6 ± 0.5

Notes. Columns 1 and 2: cluster right ascension and declination. Column 3: cluster redshift (Sander et al., 2011). Column 4: cluster mass within R_{500} (Planck Collaboration XXVII 2016).

Table 2.2: Shock fronts' projected positions

Shock	$r_{sh}(kpc)$	$r_{sh}(arcsec)$	$\theta_1 - \theta_2$	t_{age} (Myr)
S1- inner east	53.9	11.0	130°-190°	28.5 ± 2.4
S2- inner west	50.5	10.3	310-15°	32.8 ± 2.8
S_{in} - inner total	52.4	10.7	0-360	33.4 ± 1.3
S3- middle south	79.4	16.2	200°-270°	50.9 ± 4.3
S4- middle north	81.8	16.7	45°-110°	54.9 ± 4.5
S5- outer east	136	27.7	140°-252°	84.7 ± 6.4
S6- outer west	129	26.3	304°-87°	82.8 ± 6.9

Notes. Column 1: shock labels; columns 2 and 3: distance of the shock from the centre measured from the front mid-aperture; column 4: angular range intersecting the position of the edge of the shock; column 5: age of the shocks computed as $t = \frac{r_{sh}}{\mathcal{M} c_s}$ with $\mathcal{M}$ being the Mach number of the shocks and c_s the soundspeed. Credit: Ubertosi et al. (2023).

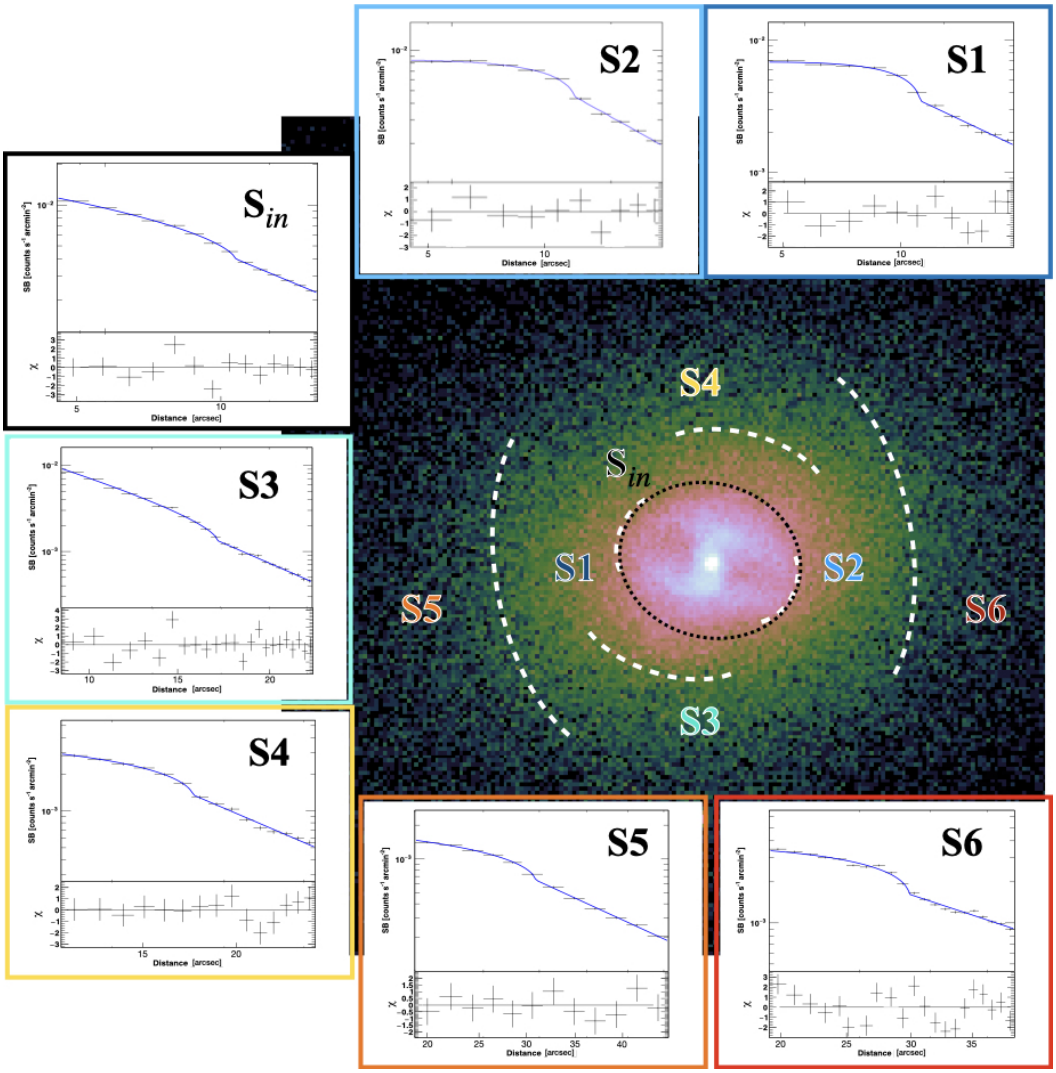

Figure 2.1: X-ray surface brightness analysis of RBS 797 (adapted from Ubertosi et al., 2023). *Central panel:* Chandra 0.5-7 keV image of the cluster. White (black) dashed regions mark the arc-like (cocoon-like) edges identified in the surface brightness analysis; coloured labels indicate the individual edges. *Subpanels:* Surface brightness profiles extracted across each edge and fitted with a broken power-law density model (blue lines). The residuals of the fits are shown in the lower panels of each plot.

Mini-halo

Previous works on RBS 797 have given us detailed information on the mini-halo in the centre of the cluster, the object of study of this thesis work. From Gitti et al. (2006) it has been found that the object has a largest angular scale of $\sim$ 200kpc at 1.425GHz and the image published by Doria et al. (2012) at the same frequency showed an elongated morphology in the north-south direction. In Bonafede et al. (2023) the image from LOFAR data at 144 MHz was slightly different, with the asymmetry showing in the east-west direction: there the largest scale was found to be $\sim 50''$ corresponding to 250kpc, while in the north-south direction the value is $\sim 30''$ corresponding to 150kpc. Figure 2.2 shows the 1.4 and LOFAR image of the mini-halo from the work of Bonafede et al. (2023).

In Ubertosi et al. (2023) it was shown that most of the emission of the mini halo at 1.4 GHz is confined within the middle pair of shock fronts previously mentioned, as shown in fig. 2.3.

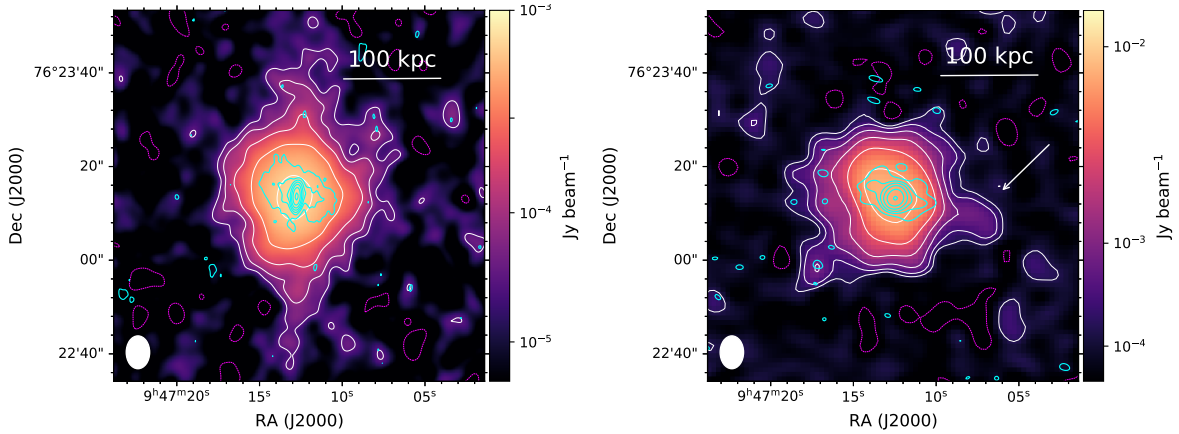

(a) VLA at 1.425 GHz.

(b) LOFAR HBA at 144 MHz.

Figure 2.2: Images of the galaxy cluster RBS 797 at VLA and LOFAR frequencies (Bonafede et al., 2023). In both panels, colours and white/magenta contours show the diffuse mini-halo emission after subtraction of the central sources and in both images white contours start at $2\sigma_{rms}$ and increase by a factor 2 each; rms noise is 0.02 $mJy/beam$ at 1.425MHz and 0.1 $mJy/beam$ at 144MHz. Both images have a resolution of $7'' \times 5''$. Cyan contours highlight the central source. The white arrow in the LOFAR panel marks the western plume detected at 144MHz.

In Figure 2.3 we can appreciate the overlay of the shocks (detected by Ubertosi et al. 2023) onto the radio X-ray and optical emission of the subtracted mini-halo (composite image produced by Bonafede et al. 2023).

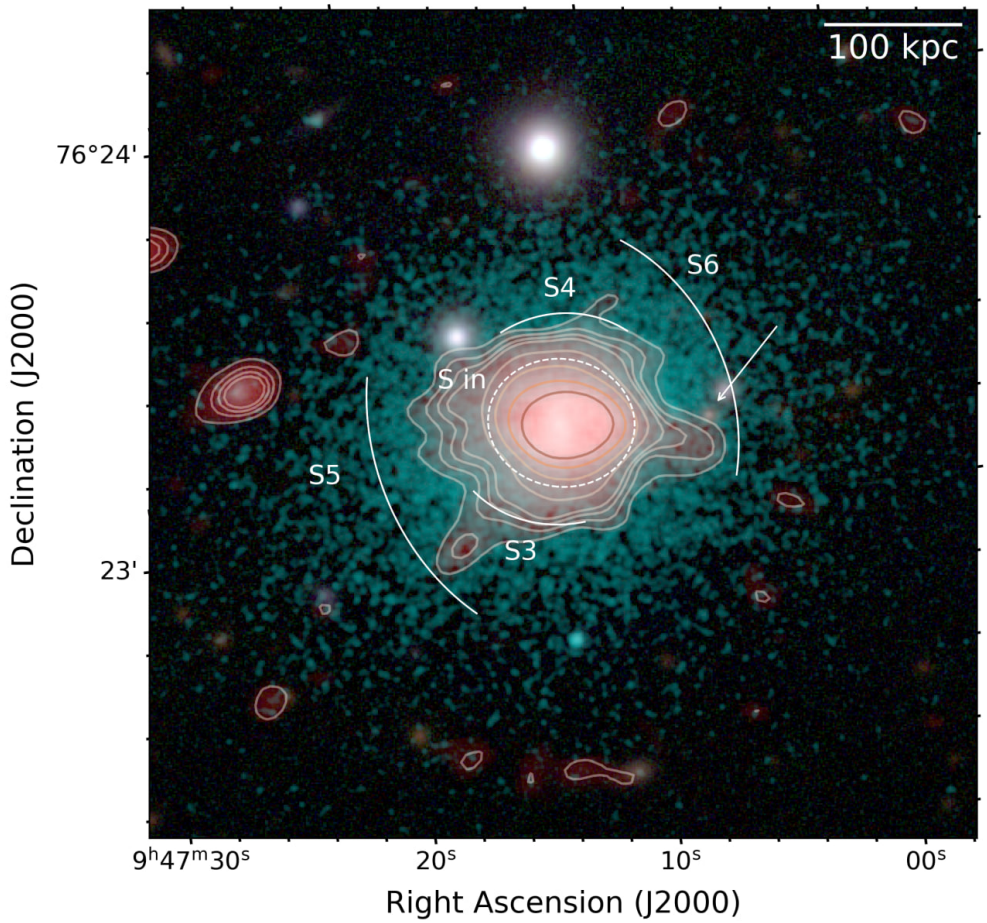

Figure 2.3: Composite optical, X-ray, and radio view of the galaxy cluster RBS 797 (adapted from Bonafede et al., 2023). The LOFAR HBA 144 MHz emission is shown in red and as contours (rms noise $\sigma_{\rm rms} = 0.1$ mJy beam^{-1}; beam size $7.0'' \times 4.7''$). Contours start at $3\sigma_{\rm rms}$ and increase by a factor of two. The Chandra X-ray image is displayed in cyan, while the optical background is a composite g, r, i image from Pan-STARRS. The arc-like structures labelled S3–S6 and the dashed ellipse labelled $S_{\rm in}$ indicate the shock fronts identified by Ubertosi et al., 2023. The white arrow marks the position of the western plume.

2.2 Instruments overview

The radio data analysed in this thesis were obtained from two major interferometric facilities: the Karl G. Jansky Very Large Array (JVLA) and the LOw Frequency ARray (LOFAR). The term VLA refers to the original Very Large Array, which has been operational since 1980 and underwent a major technological upgrade between 2010 and 2012: this upgrade involved the complete replacement of the receivers, electronics, and correlator, significantly improving the instrument's sensitivity, instantaneous bandwidth, and spectral capabilities. Following the completion of this enhancement in 2014, the facility was renamed the Karl G. Jansky Very Large Array (JVLA), while retaining the same interferometric configuration.

Specifically, we combined the LOFAR 144 MHz and JVLA 1.4 GHz observations published in Bonafede et al. (2023) with new JVLA observations at 5.5 GHz. The new data we analysed cover a high frequency range, between 4.5 and 6.5 GHz (the so-called C-band), and were taken with the JVLA in the C and D configurations. As shown below, the high angular resolution offered by these frequencies, coupled with the sensitivity of the C and D, was able to efficiently probe the diffuse emission of the radio mini-halo.

In this section, I will present a brief overview of the main characteristics of the two instruments, with a focus on the JVLA's configurations used for the dataset we analysed. For an explanation of the theory of Radio Interferometry see Appendix B.

2.2.1 JVLA

The JVLA is a 27-element (28 including the one that is a spare) interferometric array with antennas having a parabolic dish of 25 m diameter, arranged along the arms of an upside-down "Y", which produces images of the radio sky at a wide range of frequencies and resolutions [1]. It is located at an elevation of 2100 meters on the Plains of San Agustin in southwestern New Mexico.

Like all interferometers, the JVLA is sensitive only to structures on a range of angular scales between the diffraction limit, which is the smallest angular scale detectable and depends on the inverse of the biggest longest baseline (defined as the distance between two antennas), and a "Largest Angular Scale", which depends on the fringe spacing formed by the shortest baselines in the configuration (see details in Appendix B).
For emission structures smaller than the diffraction limit ($\theta_{res} \sim \lambda/B_{max}$), the JVLA acts like a single-dish instrument, smoothing the image to the resolution of the array. For emission structures larger than the detectable range, the VLA is simply blind to the emission; this is a limitation unique to interferometers. For observations taken with the 8-bit samplers, each receiver can tune to two different frequencies, each 1024 MHz wide, within the same frequency band. Right-hand circular (RCP) and left-hand circular (LCP) polarizations are received for both frequencies, except for the low-band receiver (50–500 MHz), which provides linear polarization (X and Y). Each of these four data streams follows the JVLA nomenclature and are known as IF (for Intermediate Frequency channel) A, B, C, and D. IFs A and B provide RCP (or Y when applicable), IFs C and D provide LCP (or X when applicable) [2] .

2.2.2 JVLA configurations

Any single JVLA configuration will allow accurate imaging of a range of spatial scales determined by the shortest and longest baselines; for extended and resolved sources, it

[1] NRAO – VLA Overview; `https://public.nrao.edu/telescopes/vla/`

[2] The VLA Observational Status Summary; `https://science.nrao.edu/facilities/vla/docs/manuals/oss2014B/intro/overview`

may be required to obtain observations in multiple array configurations [3]. The JVLA can vary its resolution over a range exceeding a factor of ~ 50 thanks to the movement of its component antennas which leads to the composition of four basic antenna arrangements, called configurations: they are denoted D, C, B, and A, and their scales vary respectively by the ratios $1 : 3.28 : 10.8 : 35.5$ from smallest to largest [4]. In addition, there are 3 "hybrid" configurations labelled DnC, CnB, and BnA, in which the North arm antennas are deployed in the next larger configuration than the SE and SW arm antennas.
The data analysed in this thesis work come from observation in the configurations C and D in the C frequency band (this means two distinct datasets, one for each configuration, that we label CC and DC). The use of both configurations later combined in one single dataset enables the recovery of fainter and more diffuse flux at larger scales while keeping the performance of sensitivity and resolution as high as possible.

2.2.3 LOFAR

LOFAR is a low-frequency radio interferometer composed by stations spread across Europe; it covers the low-frequency range from 10-240 MHz with high angular resolution.

LOFAR is based on an array of simple omnidirectional antennas, instead of mechanical signal processing with a dish antenna, that are connected to each other with a large Information and Communication Technology infrastructure. There are two types of antennas at each station: the High Band Antennas (HBA, 110-240 MHz) and Low Band Antennas (LBA, 10-90 MHz). To make radio pictures of the sky with adequate sharpness, these antennas are to be arranged in clusters that are spread out over Europe. In total there are around 8,000 antennas in several countries, including the Netherlands, France, Germany, Ireland, Poland, Sweden and the UK, comprising, since 2019, almost 51 individual stations. The electronic signals from the antennas are digitised, transported to a central digital processor, and combined in software to emulate a conventional antenna [5]. The data analysed in this thesis are LOFAR HBA observations, obtained without the use of the international stations.

[3] `https://science.nrao.edu/facilities/vla/docs/manuals/oss/performance/comb-conf-mosaicking`

[4] The VLA Observational Status Summary;`https://science.nrao.edu/facilities/vla/docs/manuals/oss2014B/intro/overview`

[5] https://www.lofar.inaf.it

Chapter 3

Data Reduction

3.1 Datasets

In this thesis work we studied new JVLA observations of the centre of the RBS 797 galaxy cluster. The observations were carried out in two sessions, one with the JVLA set up in the C configuration and the other with the JVLA in the D configuration, both in the receiver band C with a frequency range of $4.5 - 6.5$ GHz. The first session was on `25-Nov-2023` for configuration `DC` with a time range (UTC) `14:10:30.0 - 14:49:30.0`; the second on `24-Jan-2024` for configuration `CC`, with a time range (UTC) `08:25:10.0 - 09:34:00.0`.

The CC and DC configurations are composed of 27 antennas but at the time of the observation for configuration DC only 26 antennas were available; the antennas have all the same diameter of 25 meters, but are characterised by different baselines therefore different angular resolutions, and different sensitivities. The angular resolution of a radio image is related to the arrangement of interferometer antennas: in a compact configuration the resolution is low, while an extended configuration gives higher resolution. The angular resolution provided by an interferometer is given by:

$$\theta_{res} = k\lambda/B_{max} \quad \text{[radians]} \tag{3.1}$$

where k is a factor that depends on how the visibilities are weighted (see Appendix C.1.2 for the definition of weighting) and B_{max} is the longest baseline of the array.
A description of the basic concepts of the response of a radio telescope is given in Appendix B.1, while a treatment of the theory of interferometry is given in Appendix B.2.
The configuration DC with a smaller B_{max} has a lower angular resolution than the configuration CC with a larger B_{max}.
The arrangements of the antennas in the two configurations are shown in Figure 3.1.

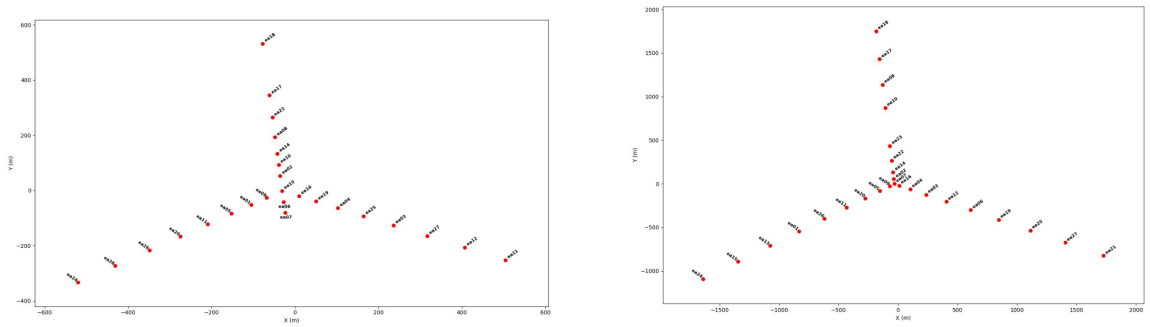

(a) (b)

Figure 3.1: Antenna arrangement in the observations of RBS 797 performed in C band with D and C configuration of JVLA telescope. Panel (a) shows the DC configuration and panel (b) shows the CC configuration.

The sensitivity can be defined as the lowest flux detectable by the instrument, with anything below such limit being classified as noise. The value of sensitivity is therefore computed looking at the regions of the image where no strong flux from a source is detectable (see Section B.3 for a detailed explanation).

The DC configuration has high sensitivity to the diffuse extended emission but can reach a maximum of $\theta_{res} \approx 9 - 12''$ of angular resolution at frequency $\nu \simeq 5\,\mathrm{GHz}$, which is too large for a resolved sampling of the mini-halo in RBS 797, which has a radius of $r_{MH} \simeq 40''$. The CC array, on the other hand, can reach up to $\theta_{res} \approx 3''$ of angular resolution but is not as sensitive to the diffuse emission, due to the reduced amount of receivers in the central region of the array which sample the most extended scales of the Field of View (FOV). The combination of the two arrays into one dataset is therefore a critical way to ensure our proposed scientific aim, keeping both high resolution and high sensitivity to extended structures.
In table 3.1 we report the summary of the main characteristics of the observations.

Table 3.1: Observations summary

Conf.	Band	ν_{ctr}	Frequency range	Bandwidth	On source time
D	C	5.5 (GHz)	4500 - 6500 (MHz)	2.0 (GHz)	1.0 (hours)
C	C	5.5 (GHz)	4500 - 6500 (MHz)	2.0 (GHz)	1.5 (hours)

Notes. Column 1: JVLA configuration; column 2: receiver band; column 3: central frequency of the receiver band; column 4: bandwidth in GHz; total integration time on source for each configuration.

3.2 Imaging and uv coverage

CASA, the Common Astronomy Software Applications package, is the primary data processing software for the JVLA and is also frequently used for other radio telescopes. The CASA software can process data from both single-dish and aperture-synthesis telescopes, and one of its core functionalities is to perform data reduction and imaging of the observed targets (NRAO education, CASA tutorial). During this thesis work

the release CASA 6.7.2 was used. See Appendix C for the explanation of the basic concepts of radio imaging.

As previously explained, the first aim of this thesis work was to merge the datasets corresponding to the two different JVLA configurations to maximize both angular resolution and sensitivity.

The data had been previously calibrated according to the standard procedure for JVLA interferometric data as described in CASA guides, VLA tutorial.

Subsequently, we inspected the datasets to check for any bad data that required flagging: flagging is a task operated on CASA that allows to remove any data that is a consequence of systematic errors in the measurement procedure. In both datasets, the only flagging necessary was that of spectral window number 10: the datasets are composed of 16 spectral windows, and for both configurations the spectral window 10 showed visibility amplitude values of more than an order of magnitude higher than those of the other spectral windows, likely indicating corrupted data.

We then proceeded with an initial basic imaging of the source in the two separate array configurations to check if the sensitivity and resolution of the observations met the expectations.
In table 3.2 we report the main characteristics of the images of the two different configurations to compare them with the expected values computed analytically in the observing application; both images have been produced with Natural weighting (see Appendix C.1.2 for definition). The expected resolutions were $\theta_{res} \approx 12''$ for the DC array and $\theta_{res} \approx 4''$ for the CC array; the same sensitivity level of $4\,\mu$Jy/beam was expected for both configurations. Both angular resolution and sensitivity were in line with the expected values, even with basic imaging parameters.

The beam and sensitivity values are characteristics of the image produced, affected by the parameters used; the uv-range on the other hand is a property of the dataset and therefore is not affected by the imaging parameters used: it refers to the minimum and maximum values of baselines in the configuration in unit of wavelength, giving therefore information on the resolution expected in the image, following Equation 3.1. The value of baseline in units of λ is defined as the distance in units of meters weighted by the central wavelength of the observation band $UV_{wave} = UV_{dist}/\lambda_{ctr}$.

Table 3.2: Characteristics of the images of the different configurations

Configuration	Band	$\nu_{\rm ctr}$ (GHz)	Beam	PA	UV-range (λ)	Sensitivity
D	C	5.5	$20.9'' \times 12.9''$	-26.2°	440–22000	4.6 μJy/beam
C	C	5.5	$5.9'' \times 3.9''$	-4.4°	640–74000	4.2 μJy/beam

Notes. Column 1: VLA configuration; column 2: receiver band; column 3: central frequency of the receiver band; column 4: angular dimensions of the synthesized beam; column 5: position angle of the synthesized beam; column 6: minimum and maximum values of baseline in unit of wavelength; column 7: sensitivity of the image; column 8: weighting scheme used for the imaging, definition of weighting in Appendix C.1.2.

Another important operation had to be performed which was the adjustment of the visibility weights: visibility weights are related to the noise of the observation

and they are self-consistent within a single continuous observation; for two separate measurement sets on the other hand it is important to adjust the weights before combining the data otherwise they would be set on different scales (CASA guides, VLA tutorial). The reason for this is that the intrinsic noise level of two distinct datasets is usually different and CASA does not automatically rescale weights when different datasets are concatenated, so it is important to do it manually beforehand. The task used to correct the data weights in the measurement set is `statwt`.

After the quality check of the data, we combined the datasets using the task in CASA called `concat` that combines different measurement sets.

In Figure 3.2 the UV-coverage of the datasets before and after merging is shown. In Figure 3.3 we show the arrangement of the antennas of the combined dataset, while in Table 3.3 we report the characteristics of the combined dataset. The combined dataset has a wider UV-range that enables both a high angular resolution and high sensitivity to the diffuse emission.

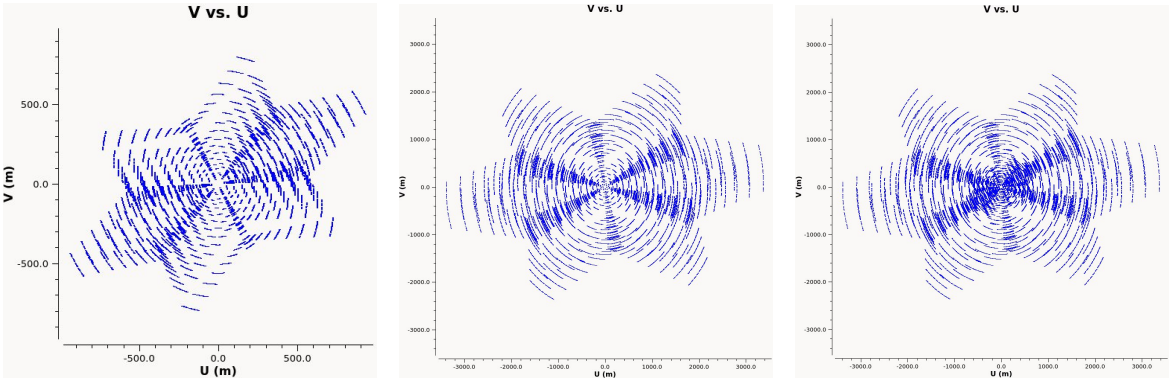

(a) (b) (c)

Figure 3.2: UV coverage of the VLA C-band observations of RBS 797. Panel (a) shows the UV-coverage for the DC configuration, panel (b) for the CC configuration, and panel (c) for the combined DC + CC dataset after concatenation. Details of the individual observations are reported in Table 3.2, while the properties of the merged dataset are listed in Table 3.3.

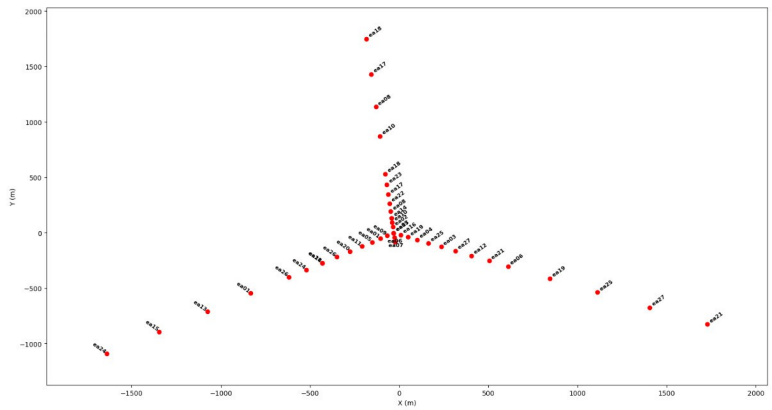

Figure 3.3: Antenna arrangement of the combined observations of RBS 797 in D and C configuration of JVLA telescope.

Table 3.3: Merged dataset characteristics

Configuration	Band	Frequency range	Bandwidth	UV-range (λ)
C+D	C	4500 - 6500 (MHz)	2.0 (GHz)	440–74000

Notes. Column 1: JVLA configuration; column 2: receiver band; column 3: frequency range of the receiver band in MHz; column 4: bandwidth in GHz; column 5:minimum and maximum values of baseline in units of wavelength.

Multiscale imaging

With the newly combined dataset, we proceeded with a multiscale and multi-frequency imaging of the FOV of the central region of RBS 797, which includes the central AGN, mini-halo and other unclassified smaller compact sources.
To maximize the efficiency of the deconvolution procedure, it was useful to restrict the process to the regions where flux from a source is present: to do this, we drew a mask on the initial image obtained from a basic cleaning procedure, following the contours of the sources starting at 3σ. The mask can be saved and then used with the `mask` parameter in the CLEAN algorithm (mask shown in Figure 3.4).

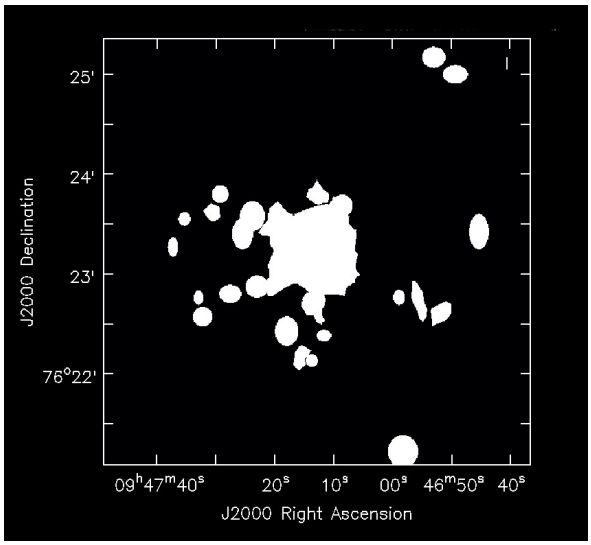

Figure 3.4: Image of the mask drawn for RBS 797 at 5.5 GHz, following the 3σ contours of the initial image obtained from the CC dataset with a basic cleaning procedure. The image has a resolution of $5.9'' \times 3.9''$ and a rms noise of 4μJy/beam.

The detailed explanation of how the CLEAN algorithm works is given in Appendix C.1.1.

For the multiscale and multi-frequency imaging we used the parameter '`mtmfs`' which stands for Multi-Term Multi-Frequency Synthesis: it is a deconvolution algorithm in `tclean` specifically designed for wideband radio data where the frequency range is broad enough that the flux density of sources varies with frequency within the band; indeed, for wideband observations (e.g., VLA or MeerKAT with GHz of

bandwidth), sources' brightness changes with frequency and also their structure can change slightly (CASA guides, tclean task). The '`mtmfs`' parameter models the wide-band sky brightness distribution through the use of a multi-term Taylor polynomial and wideband primary beam corrections. The dependence on frequency in the polynomial ensures a more realistic distribution of flux along frequency, contrary to the assumption of constant flux along the bandwidth, which is characteristic of default parameters.

The dependence on frequency is set with the parameter `nterms`; in this case `nterms`= 2, which is a second-degree polynomial that results in a realistic model of the flux and spectral index.

The parameter `scales` sets the spatial scales at which the flux is searched during the deconvolution process; during the restoring step, when the clean components are convolved with the synthesized beam, these scales are taken into account, starting from 0 (correspondent to the delta gaussian that usually suits a point source) up to the value corresponding to the maximum physical scale of the object of study. The residuals are therefore not convolved with the same beam but iteratively with multiples of the beam until all the flux from the source is inside the beam. The value selected for the maximum physical scale in the `scales` parameter is $\sim 200\,\mathrm{kpc} \simeq 40''$, which is the maximum value of extension of the mini-halo as detected from previous works.

In Figure 3.5 the result can be appreciated; the image was obtained by selecting Briggs weighting with $R = 0.5$ (see Appendix C.1.2), and a maximum angular scale of multiscale parameter equal to $40''$. The angular resolution of the image is $\theta_{beam} = 5.3'' \times 3.5''$, with a noise of $\sigma_{rms} = 3.6\mu\,\mathrm{Jy/beam}$.

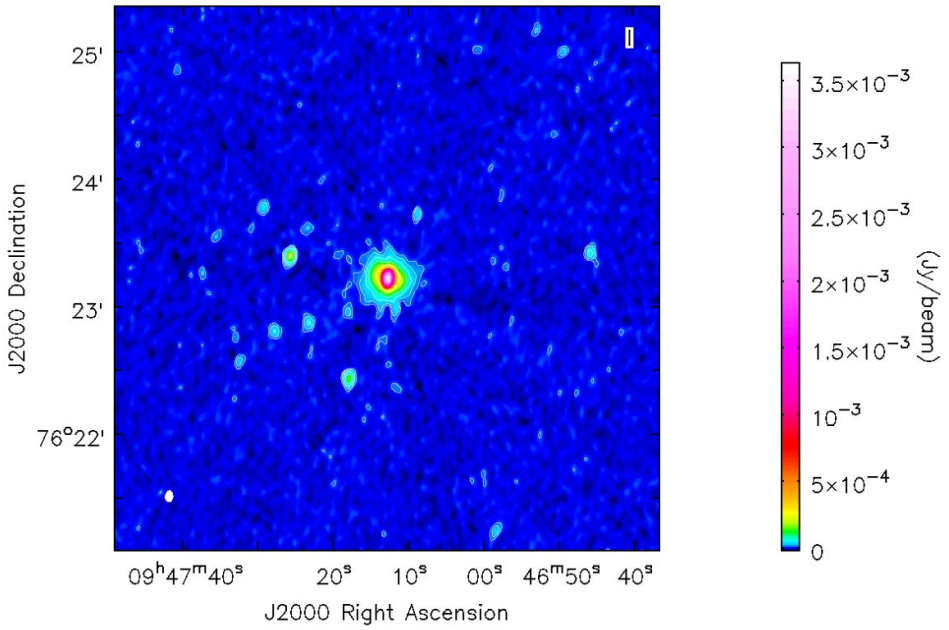

Figure 3.5: JVLA image of the FOV of RBS 797 obtained from the combination of the two configurations of JVLA, DC and CC, in C band with central frequency 5.5 GHz; the FOV includes the radio source in the BCG, the diffuse emission of the mini-halo, and background/foreground compact radio sources. The synthesized beam is shown in the lower-left corner, $\theta_{beam} = 5.3'' \times 3.5''$. $1''$ corresponds to 4.98 kpc at cluster redshift. The noise is $\sigma_{rms} = 3.6\,\mu$Jy/beam; contours start at 3σ and increase by a factor of 2 each. Imaging parameters are: Briggs weighting with $R = 0.5$ (see Appendix C.1.2) and maximum value of multiscale parameter equal to $40''$.

3.3 Source subtraction in the uv-plane

After the imaging of the full source, we proceeded with the non-trivial task of subtracting the central radio galaxy and the other compact sources from the data, to be able to focus solely on the diffuse emission of the mini-halo and study it without the contamination from the AGN.
RBS 797 is among the most complicated cases of mini-halos with respect to the disentanglement of the diffuse emission from the central AGN, since they are extended over very close scales: the AGN has a largest linear size of $\sim 20''$ and $\sim 10''$ of radius, while the mini-halo has a largest linear size of $\sim 40''$ and a radius of $\sim 20''$. Nonetheless, the success of this operation is crucial to the reliability of the analysis and it is necessary to accurately subtract the compact sources to be able to study the target with precision.

We followed the method of source subtraction in the uv-plane, as explained in the literature (e.g. Venturi et al. 2008; Vacca et al. 2014; van Weeren et al. 2016; Savini et al. 2019; Bonafede et al. 2023). The emission from the compact source can be removed by modelling the corresponding visibilities in the uv-plane and then subtracting them from the image of the FOV of RBS 797. The AGN has an extension of $r \simeq 10''$ so we created a model of the compact sources imaging only visibilities

with $uvrange > 10^4\lambda$, which corresponds to a physical scale of 100 kpc $\simeq 20''$; the model (extrapolated to all baselines included the shorter ones) is saved into the `MODEL` column of the dataset. The `MODEL` column is then subtracted from the `DATA` column, producing an additional dataset that contains all baselines but only flux components related to physical scales larger than $\sim 20''$, which therefore represents only the diffuse emission of the mini-halo.

The value of Robust = 0.7 was found to be the best for modelling the compact sources as a compromise between the compact sizes of the smallest sources and the extension of the AGN lobes, in order to be sure not to leave any of the most extended diffuse emission behind. The comparison was done by looking at the residual images after the subtraction of the model with different robust values. Figure 3.6 shows the image of the compact sources in panel (a), and the residual emission of the FOV after the subtraction for $uv \geq 10^4\lambda$ in panel (b); the fact that in the residual emission only noise is present is a confirmation that the subtraction of the compact sources was successful.

The final subtracted dataset was then used to produce images of the mini-halo. A first image was produced with tapering to better appreciate the diffuse emission (fig. 3.7). Tapering is an imaging procedure used in radio astronomy to highlight diffuse emission: tapering applies a Gaussian smoothing function to down-weight long baselines (which correspond to high spatial frequencies); it affects the outer baselines in the uv-plane so that higher spatial frequencies are weighted down relative to lower spatial frequencies. This is obtained with parameter `uvtaper` in the CLEAN algorithm, defined as either the Half Width Half Maximum (HWHM) of the Gaussian function in the UV-space (in units of lambda) or as the Full Width Half Maximum (FWHM) of the Gaussian function in the image domain (in angular units like arcseconds). The latter is the unit method used in our work. The final effect is equivalent to the smoothing of the PSF obtained by other weighting schemes that aim at enhancing the diffuse emission (section `uvtaper` of CASA Documentation Team, Synthesis Imaging).

An additional image without tapering is produced to investigate the morphology of the source with higher angular resolutions; the results are shown in Figure 3.8.

The imaging parameters for the compact sources and subtracted mini-halo are in Table 3.4, along with the main features of the images produced; Robust values refer to Briggs weighting for both images (definition of weighting found in Section C.1.2).

For both images we computed the integrated flux density, a value given automatically in the statistics of the CASA image viewer, once a region is selected: the region selected for this case is the area where the emission of the source is above 3σ in both images.

The uncertainty on the measure of flux density is given by the formula

$$\sigma_F = \sqrt{(rms * N_{beams})^2 + (\delta F * F)^2}\,, \tag{3.2}$$

with N_{beams} being the number of beams in the area, and δF being the systematic

Table 3.4: Imaging parameters and features

Source	Uv-range (λ)	Robust	UV-taper	Beam	PA	Sensitivity
Compact Sources	$> 10^4$	0.7	–	$4.4'' \times 2.9''$	$-5.0°$	$3.6\,\mu$Jy/beam
Subtraction residual	$> 10^4$	0.7	–	$4.4'' \times 2.9''$	$-5.0°$	$3.6\,\mu$Jy/beam
Subtracted mini-halo	440–74000	0.5	$5''$	$8.1'' \times 6.7''$	$-9.3°$	$3.7\,\mu$Jy/beam
Subtracted mini-halo	440–74000	0.5	–	$5.3'' \times 3.5''$	$-5.3°$	$3.9\,\mu$Jy/beam

Notes. Column 1: source shown in the image; column 2: range of visibility wavelengths included in the image; column 3: robust parameter for Briggs weighting (see AppendixC.1.2 for the definition); column 4: FWHM of the Gaussian smoothing function applied in the image domain; column 5: size of the synthesized beam; column 6: position angle of the synthesized beam (in degrees); column 7: image rms noise.

calibration uncertainty on the flux density scale, a value that is assumed to be 5% for the JVLA telescope.

For the image obtained with tapering, the integrated flux density of the mini-halo as a result of source subtraction is 2.05 ± 0.10mJy, within contours starting at 3σ with $\sigma_{rms} = 4\,\mu$Jy/beam. The morphology is slightly asymmetrical with the largest angular scale equal to $41.8''$ in the EW direction and $41.4''$ in the NS direction, corresponding respectively to 204.82 kpc and 202.86 kpc at the cluster redshift. At frequencies of 5.5 GHz, the mini-halo appears more centrally symmetric than at 144 MHz and 1.4 GHz based on the images presented in Gitti et al. (2006); Doria et al. (2012); Bonafede et al. (2023). The asymmetry in morphology is less pronounced than it was seen in Bonafede et al. (2023) at 144 MHz.

For the image obtained without tapering, the value of flux density is 1.96 ± 0.10mJy, with $\sigma_{rms} = 3.9\,\mu$Jy/beam; contours start at 3σ and increase by a factor of 2 each. Maximum extension in the EW direction is $30.5''$ and in the NS direction is $33.7''$; the slight asymmetry is therefore enhanced with higher angular resolution. The integrated flux density is consistent with and without tapering.

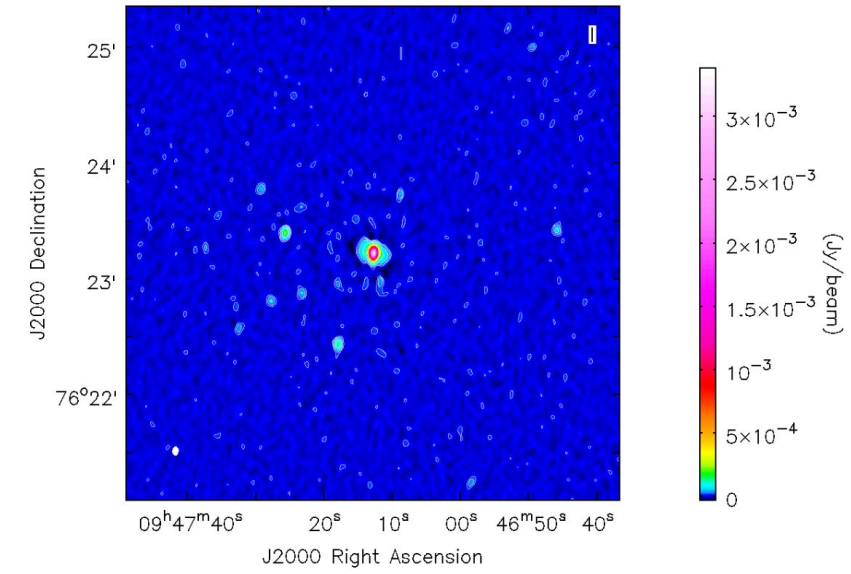

(a)

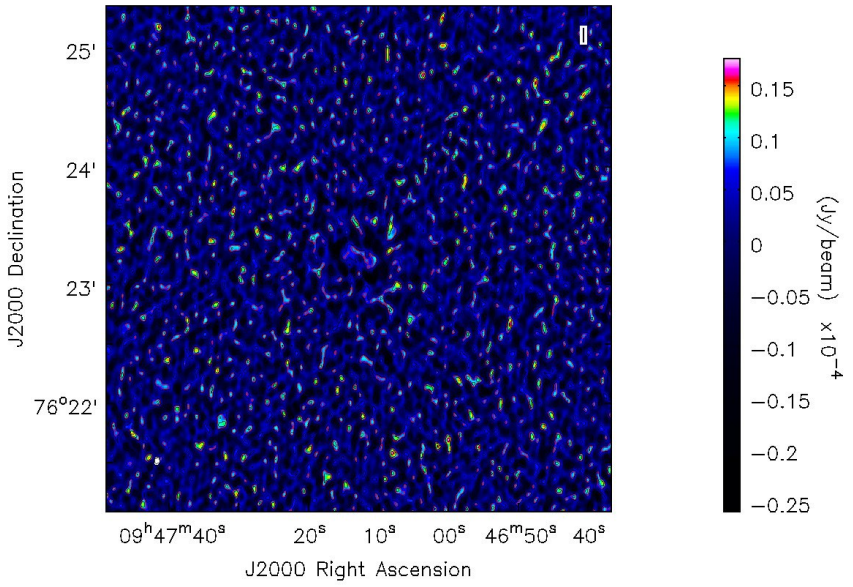

(b)

Figure 3.6: Panel (a): 5.5 GHz JVLA image of the compact sources in the centre of RBS 797 cluster. Image modelled for $uv \geq 10^4\lambda$, with Briggs weighting and Robust= 0.7. The beam has an angular size of $\theta_{beam} = 4.4'' \times 2.9''$ and is shown in the bottom-left part of the image; the rms noise of the image is $\sigma_{rms} = 3.6\mu$ Jy/beam; contours start at 3σ and increase by a factor of 2 each. Panel (b): residual emission of the FOV of RBS 797, imaged with uv-range $uv \geq 10^4\lambda$ after source subtraction. Sensitivity of the image is $\sigma_{rms} = 3.6\mu$ Jy/beam, contours in red are at 2σ.

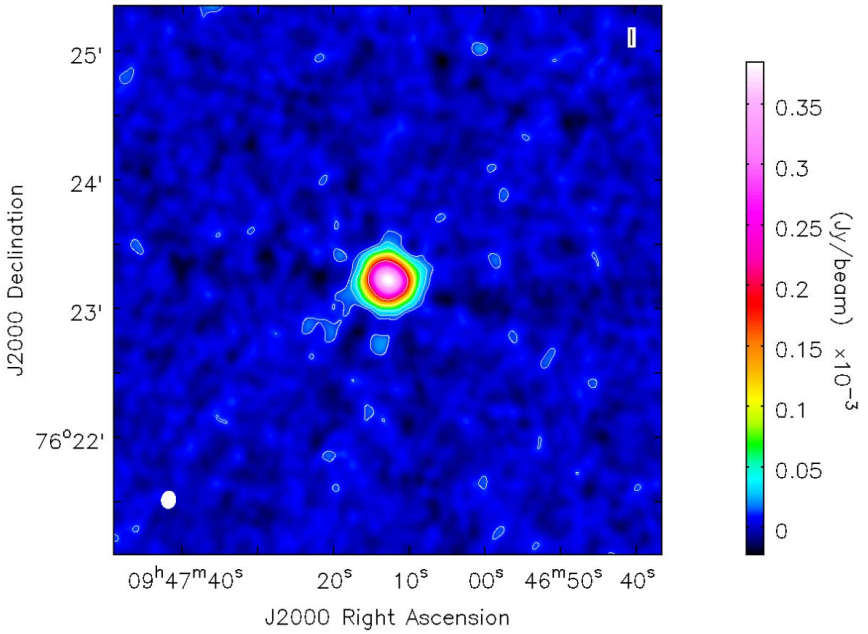

(a)

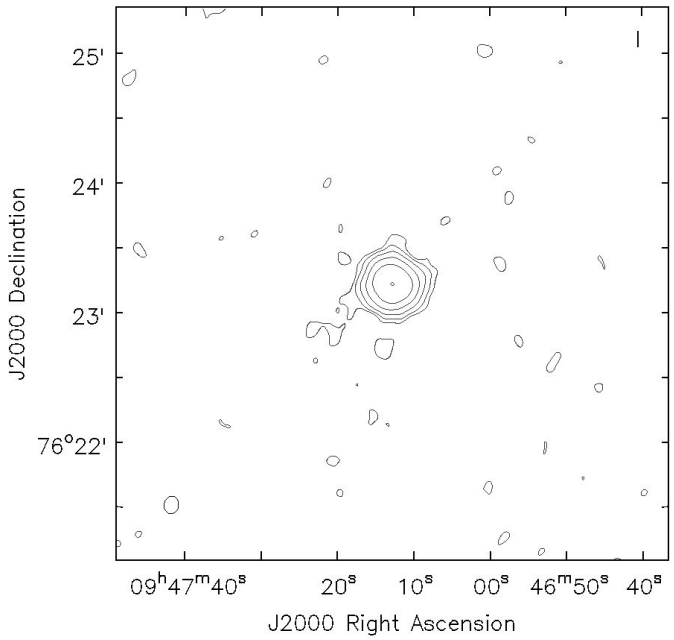

(b)

Figure 3.7: 5.5 GHz JVLA image of the mini-halo in the centre of RBS 797, imaged after source subtraction, with tapering to enhance diffuse emission. The beam has an angular size of $\theta_{beam} = 8.1'' \times 6.7''$ and is shown in the bottom-left part of the image; the sensitivity is $\sigma_{rms} = 3.6\mu$ Jy/beam; contours start at 3σ and increase by a factor of 2 each. Maximum extension in the EW direction is $41.8''$ and in the NS direction is $41.4''$. Panel (b) shows the contour map.

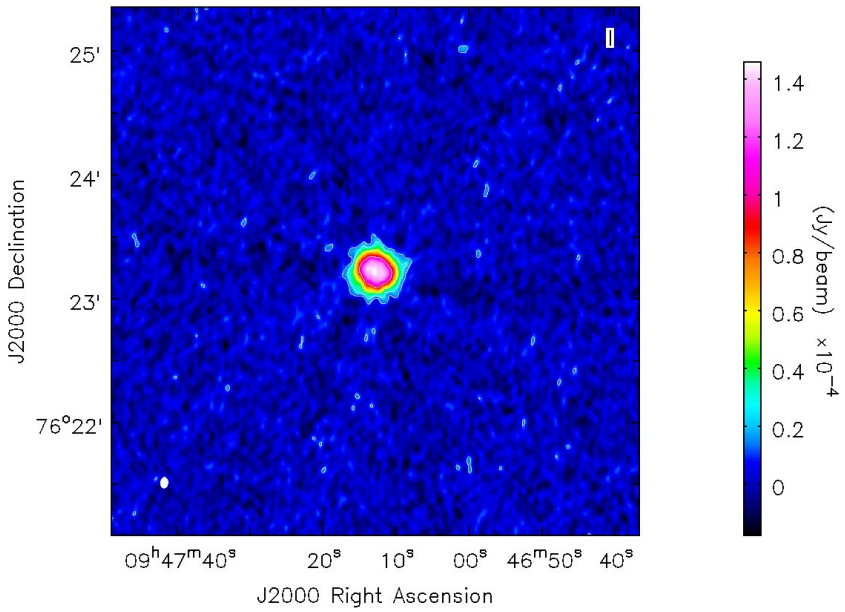

(a)

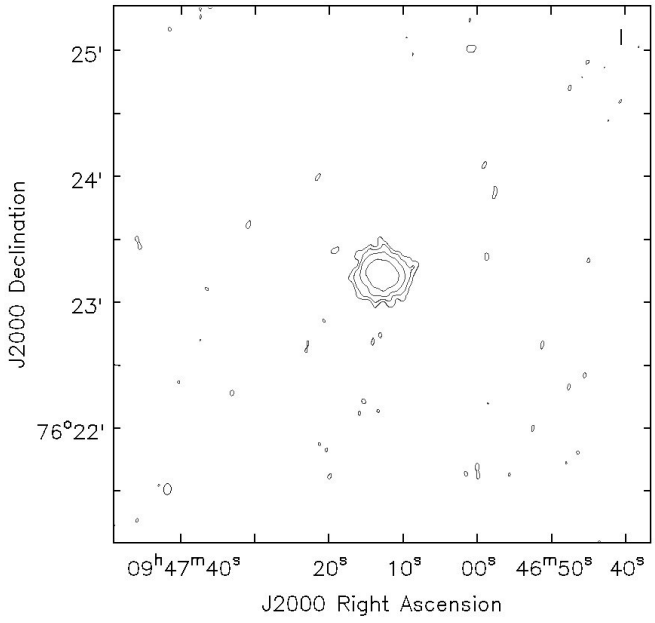

(b)

Figure 3.8: 5.5 GHz JVLA image of the mini-halo in the centre of RBS 797, imaged after source subtraction without tapering. The beam has an angular size of $\theta_{beam} = 5.3'' \times 3.5''$ and is shown in the bottom-left part of the image; the rms noise is $\sigma_{rms} = 3.9\mu$ Jy/beam; contours start at 3σ and increase by a factor of 2 each. Maximum extension in the EW direction is $30.5''$ and in the NS direction is $33.7''$. Panel (b) shows the contour map.

Chapter 4

Scientific Analysis

4.1 Spectral Index fit from integrated flux

We have performed a data reduction that has produced an image of the mini-halo emission after the subtraction of the central AGN and other compact sources, and we therefore have a reliable value of integrated flux density of the mini-halo at 5.5 GHz. This allows us to compute the spectral index from the integrated flux of the new high-frequency measurement together with the values from the archival data at 144 MHz and 1.4 GHz.

The analytic formula for the spectral index when the synchrotron emission is a perfect power law is equation **??**, and it is sufficient to have two values of flux density at two different frequencies to compute it.

$$\alpha = \frac{log(S_1/(S_2)}{log(\nu_1/(\nu_2)} \tag{4.1}$$

Otherwise, if we cannot assume a perfect power law, the formula computed with only two frequencies would not be representative, and we would need data at three frequency values at least.
A first approximation of the value of the spectral index for more than two frequencies can be inferred by performing a simple linear fitting in logarithmic space: we took note of the integrated flux density of the source from the images (the one at 5.5 GHz produced in this thesis work, and the two archival images at 144 MHz and 1.4 GHz), then we plotted the values of flux density as a function of frequency while performing the linear fit. This method results in a best-fit power law whose index would be an estimate of the spectral index value (as seen in equation Equation (1.9)).

In order to do this, it is important to have all the images convolved with the same beam size, and with the same UV-range. The two archival images from the work of Bonafede et al. (2023) had an elliptical beam of $7'' \times 5''$ so we convolved our image with the same beam.

The integrated flux density values are given by the statistics section of the CASA image viewer, once a region is selected: for the computation of the spectral index the

region was drawn following the intersection of the 3σ contours of the three images, allowing the formula to be computed only in a region where the emission is above the 3σ threshold for all frequencies (region shown in Figure 4.1).

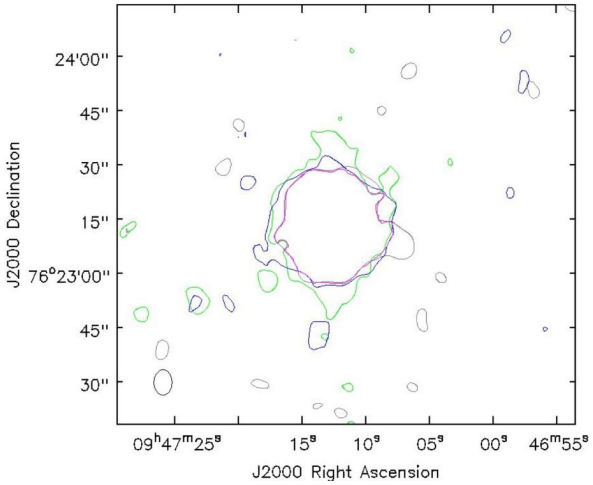

Figure 4.1: Image shows the region selected for the extraction of the integrated flux density of the mini-halo emission of RBS 797; magenta line shows the region contour, drawn following the interception of the 3σ contours of the three images; gray line shows the 3σ contours of the image at 144 MHz; green line shows the 3σ contours of the image at 1.4 GHz; blue line shows the 3σ contours of the image at 5.5 GHz. All images are convoluted with a beam of $7'' \times 5''$, shown in the bottom left of the picture.

The rms noise is 0.1 mJy/beam at 144 MHz, 0.02 mJy/beam at 1.4 GHz, and 4 μJy/beam at 5.5 GHz.

The uncertainty on the flux is described by Equation (3.2); δF in this case is assumed to be 5% for the JVLA images (1.4 GHz and 5.5 GHz) and 10% for the LOFAR image at 144 Mhz.

The fit is a linear best-fit of $S_\nu = S_0\,\nu^{-\alpha}$ for the three values of flux density; Figure 4.2 shows the fit in a logarithmic scale, Table 4.1 provides a table of fluxes and best fit values.

Table 4.1: Integrated flux densities and spectral index fit

S_{144} (mJy)	$S_{1.4}$ (mJy)	$S_{5.5}$ (mJy)	α_{fit}	χ^2
74.6 ± 7.4	7.4 ± 0.3	1.9 ± 0.1	-1.007 ± 0.001	0.001

Notes. Column 1: flux density of subtracted mini-halo computed on archival image at 144MHz; column 2: flux density of subtracted mini-halo computed on archival image at 1.4GHz; column 3: flux density of subtracted mini-halo computed on image at 5.5GHz produced during this thesis work; column 4: best-fit spectral index. At all frequencies the region where flux density is computed is an area where emission is above 3σ for all frequencies. At all frequencies the images are convoluted with a beamsize of $7'' \times 5''$; column 5: reduced chi-square of the fit.

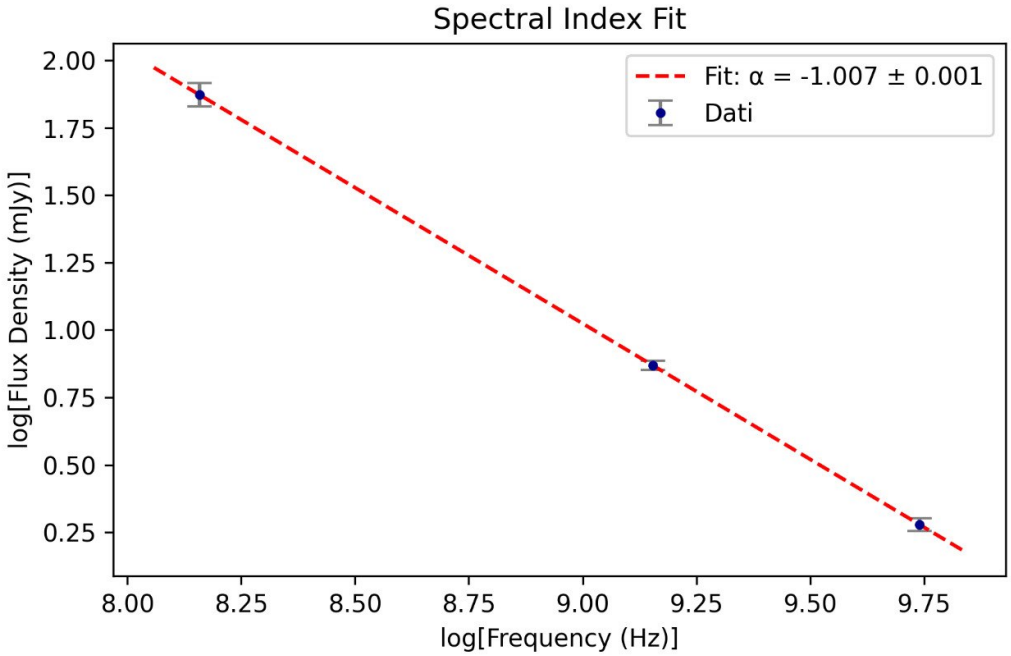

Figure 4.2: Radio spectrum from linear fit of the mini-halo in RBS 797 after discrete source subtraction. The red line shows a power-law result of the best-fit of the data. The data are values of integrated flux density extracted from the subtracted images at 144 MHz, 1.4 GHz and 5.5 GHz. The region where flux density were computed is an area where the emission is above 3σ for all frequencies. All images were convoluted with a beam of $7'' \times 5''$.

We can see from this first estimate of α, integrated over the whole area of the source, that no spectral steepening is observed and the error on the measure is very small, indicative of little deviation of the data points from the best-fit line.

4.2 Spectral index maps

A spectral index map represents the spatial distribution of the radio spectral index α across the area of an extended source; it allows for the spectral index to be studied on spatially resolved scales, revealing regions with flatter or steeper spectral index values that would otherwise be averaged out in the integrated measurement.

In this case study, we are looking for a radial trend of the spectral index value to constrain the relation between the mini-halo emission and the AGN-driven shocks. Previous work on (Bonafede et al., 2023) showed a spectral flattening with radius towards the outskirts of the mini-halo, suggesting that the shock fronts co-spatial with the emission accelerated the particles in those regions. A spectral index map was not provided in such work so we produced one (Figure 4.3), utilizing the archival images at 144 MH and 1.4 GHz.

The spectral index map is produced using the images at the two different frequencies, and computing pixel by pixel the analytic formula for α, as in Equation (4.1).

Since the operation is done pixel by pixel, we have to make sure that the coordinate reference frames of the images are aligned; to achieve this, the task `imgrid` on CASA

allows to center the coordinates of an image onto those of another one.

The CASA task `immath` is used for performing mathematical operations on images and on specific channels within images, including computing the spectral index [1].

Along with the spectral index map, a spectral index error map is produced; the propagated uncertainty on α assuming error on the fluxes ΔS_1 and ΔS_2 is given by:

$$\Delta_\alpha = \frac{1}{ln(\nu_1/(\nu_2)} \sqrt{(\Delta S_1/S_1)^2 \times (\Delta S_2/S_2)^2} \ , \tag{4.2}$$

where the value of ΔS is assumed to be the statistical noise in the pixel and therefore the value of σ_{rms}. The rms noise is 0.1 mJy/beam at 144 MHz, 0.02 mJy/beam at 1.4 GHz, and 4 μJy/beam at 5.5 GHz.

For all maps produced values are computed within a threshold of flux emission of 3σ.

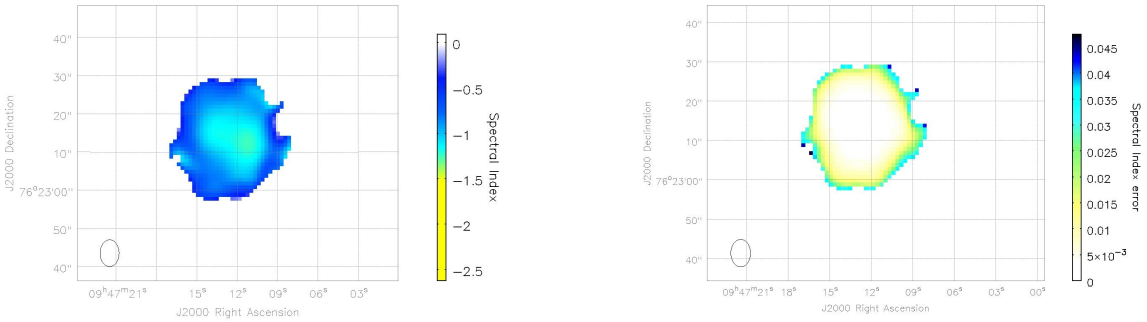

Figure 4.3: Spectral index map between 144 MHz and 1.4 GHz of mini-halo in RBS 797 after source subtraction, with related error map; the spectral index is computed between 144 MHz and 1.4 GHz with a threshold of 3σ for both frequencies; at 144 MHz $\sigma_{rms} = 0.1$ mJy/beam, at 1.4 MHz $\sigma_{rms} = 0.02$ mJy/beam. The beam angular size is $7'' \times 5''$ and is shown in the lower-left.

In Figure 4.3 wee see the confirmation of the flattening trend of spectral index, with values around $\alpha \simeq 1.2$ in the central area with related error $\alpha_{err} \simeq 5 \times 10^{-3}$, and in the peripheral area values rising to $\alpha \simeq 0.6 \pm 0.03$. Some fluctuations in the fairly uniform radial trend are seen only in regions at the very edge of the map where error values are higher.

With the additional data at C band, we were able to investigate the higher frequency part of the spectrum, computing the spectral index map between 1.4 GHz and 5.5 GHz to analyse the radial trend using a large frequency range.

[1] `https://casadocs.readthedocs.io/en/v6.5.4/notebooks/image_analysis.html`

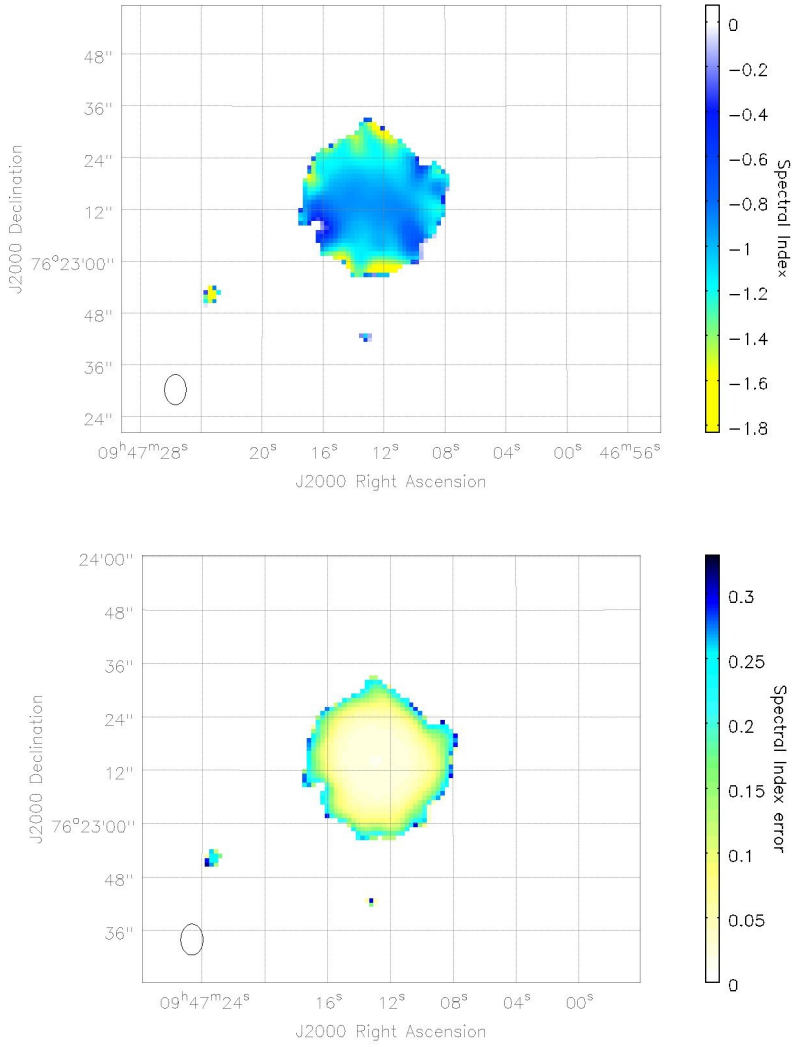

Figure 4.4: Spectral index map between 1.4 GHz and 5.5 GHz of mini-halo in RBS 797 after source subtraction, with related error map; spectral index computed within a threshold of 3σ for both frequencies; at 1.4 MHz $\sigma_{rms} = 0.02\,\mathrm{mJy/beam}$, at 5.5 GHz $\sigma_{rms} = 4\,\mu\mathrm{Jy/beam}$. The beam angular size is $7'' \times 5''$ and is shown in the lower-left.

The result are shown in Figure 4.4: in the higher frequency band we saw a radial trend that is opposite to that of the lower band. The spectral index has values of $\alpha \simeq 0.9 \pm 0.05$ in the central area and it steepens towards the outskirts up to values of $\alpha \simeq 1.2 \pm 0.1$, and $\alpha \simeq 1.6 \pm 0.2$ at the very edge (note that the edge of the map has higher error values throughout the whole perimeter). An azimuthal fluctuation of the spectral index is observed in the EW direction, with flatter values of $\alpha \simeq 0.8 - 0.7$ and error values ranging from $\alpha_{err} \simeq 0.1$ to $\alpha \simeq 0.025$, signalling that we are looking at regions with a lower signal-to-noise ratio.

An image of the $1.4 - 5.5\,\mathrm{GHz}$ map, overlayed with the AGN emission contours, is shown in Figure 4.5, indicating that the flatter regions are located at radii larger than the central source maximum extension ($r_{max,AGN} \approx 10''$), reassuring us that there should not be contamination from the AGN left from the subtraction procedure. As

shown in Figure 2.3 the inner and middle shocks found in the X-Ray are co-spatial with the mini-halo emission, with the inner shocks found at radius of $r_{sh} \simeq 11''$ in the EW direction just outside the region of the maximum extension of the AGN, and the middle shocks found at $r_{sh} \simeq 16''$ in the NS direction (see Table 2.2).

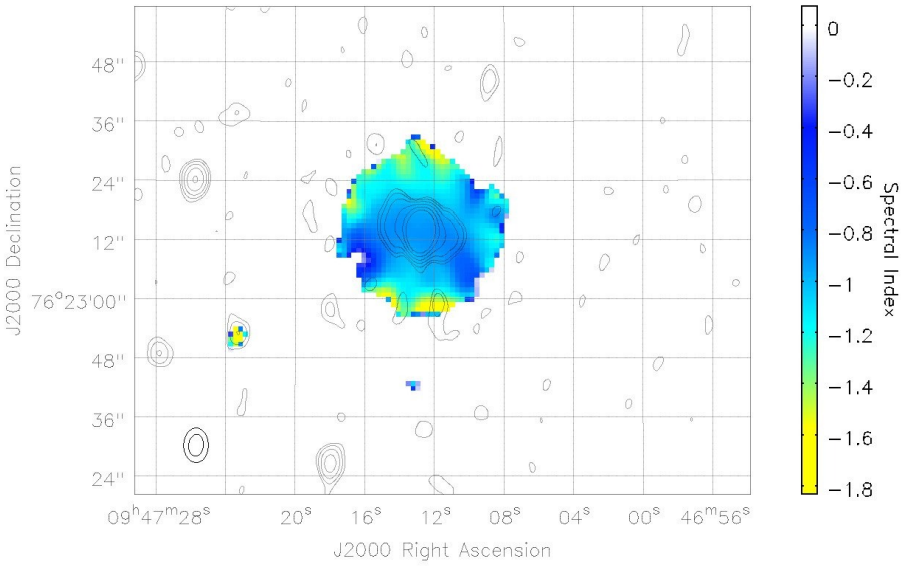

Figure 4.5: Composite image of the spectral index map between 1.4 GHz and 5.5 GHz with overlayed AGN emission contours; spectral index computed between 1.4 GHz and 5.5 GHz with a threshold of 3σ at both frequencies; at 1.4 MHz $\sigma_{rms} = 0.02$ mJy/beam, at 5.5 GHz $\sigma_{rms} = 4\,\mu$Jy/beam. The beam angular size is $7'' \times 5''$ and is shown in the lower-left. Contours of the AGN emission start at 3σ and increase by a factor 2 each.

Finally, the spectral index map with related error between 144MHz and 5.5GHz is produced, as shown in Figure 4.6.

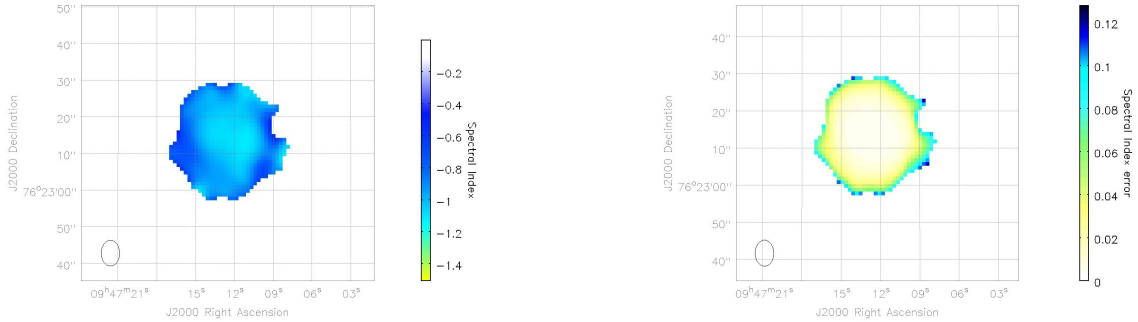

Figure 4.6: Map of spectral index between 144 MHz and 5.5 GHz and related error map, with a threshold of 3σ at both frequencies; at 144 MHz $\sigma_{rms} = 0.1$ mJy/beam, at 5.5 GHz $\sigma_{rms} = 4\,\mu$Jy/beam. The beam angular size is $7'' \times 5''$ and is shown in the lower-left.

The same flattening observed in the 144 MHz − 1.4 GHz map is observed in the map between 144 MHz − 5.5 GHz; the radial trend is slightly less uniform but with no

major subfeatures.

The flattening of the spectral index would suggest a role of the AGN-driven shock fronts in re-accelerating the particles; the steepening, on the other hand, is a feature observed in ageing populations.

In the work done by Bonafede et al. (2023), a model of the theoretical profile that would result from shock re-acceleration was provided, compared to a best-fit mini-halo profile: the two profiles were not consistent, showing a difference of a factor 6 at a distance of 10 kpc from the cluster centre. The result suggested that shock re-acceleration alone could not fully reproduce the mini-halo profile, implying that ongoing turbulent re-acceleration or continuous injection was also needed.

The results from the spatially resolved spectral index analysis seem to confirm that the scenario of a simple re-acceleration due to AGN-driven shocks, on its own, is not enough to explain the observations, which would need a more complex model than a single population of re-accelerated electrons.

To better understand the unexpected results of the high-frequency band, an analysis of the radial profiles of the spectral index has been performed, as shown in the following section 4.3.

4.3 Radial spectral profile

In this section, we show the radial profile of the spectral index, computed according to Equation (4.1) between each pair of frequencies, using values of mean brightness extracted from the images in concentric annuli. As a first test we computed the radial profile over the whole area of the mini-halo, while as a secondary check we ensured that the difference in the observed trend was not a consequence of a residual AGN emission: we did so by computing the radial profile in two distinct areas, a conical area co-spatial with the AGN-lobes in the EW direction, and another conical area free from possible contamination in the NS direction.

Spectral index profiles (radial variation) require measuring flux in concentric annuli at each frequency. This was done, for instance, by Murgia et al. (2010) for Ophiuchus and by Ignesti et al. (2020) for Perseus (LOFAR data) – typically revealing a modest steepening with radius in many mini-halos, except the anomalous flattening in RBS 797 as previously mentioned.

To compute the spectral index over the whole area we followed the method explained in Bonafede et al. (2023): we divided the surface brightness map in 7 concentric circular regions with a width equal to half the beam FWHM ($3''$) centered on the coordinates of RBS 797 centre; then we took note of the value of mean brightness of each region and computed the spectral index for each frequency pair. As a result, we had one profile for $\alpha^{144\mathrm{MHz}}_{1.4\mathrm{GHz}}$, one for $\alpha^{1.4\mathrm{GHz}}_{5.5\mathrm{GHz}}$, and one for $\alpha^{144\mathrm{MHz}}_{5.5\mathrm{GHz}}$, all plotted as a function of the radial distance from the centre. The radial profile was plotted together with the projected distances of the shock fronts reported in Table 2.2.

In Figure 4.7 we show the result of the radial profile for all frequency pairs, while in 4.8 we show the radial profile of the mean brightness for each frequency.

The spectral index profile doesn't have values in the outer regions of the mini-halo

emission corresponding to the outer shocks ($r \gtrsim 20''$), because the low brightness in those regions is too close to the sensitivity limit to be able to compute the spectral index. Observations with increased sensitivity would be needed to have data in the peripheral regions dominated by the faint diffuse emission. Moreover, the lack of data in the outer annulus for the $144 - 1425$ MHz frequency range is due to the presence of negative values in the image at 144 MHz, in a small subregion of the outer ring.

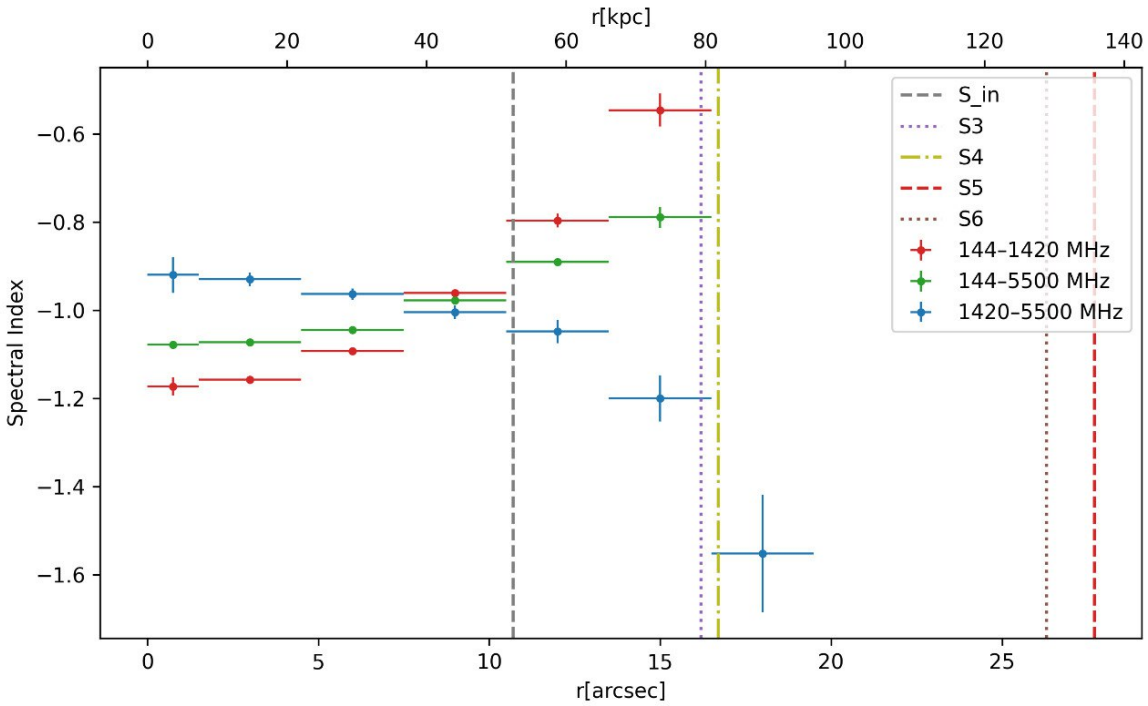

Figure 4.7: Radial spectral index profile as a function of distance from the centre, computed within concentric annuli of $3''$ of width. The data represent the values of spectral index in the three frequency ranges: red for $\alpha_{1.4\mathrm{GHz}}^{144\mathrm{MHz}}$, blue for $\alpha_{5.5\mathrm{GHz}}^{1.4\mathrm{GHz}}$ and green for $\alpha_{5.5\mathrm{GHz}}^{144\mathrm{MHz}}$. The vertical error bars represent the error on the measure computed as $\sigma_{rms}/\sqrt{N_{beams}}$, while the horizontal error bars represent the annuli's radii. The vertical lines indicate the projected distance of the shock fronts detected in the work of Ubertosi et al. (2023) whose characteristics are listed in Table 2.2. The lack of data in the outer annulus for the $144 - 1420$ MHz frequency range is due to the presence of negative values in the image at 144 MHz, in a small subregion of the outer ring (as can be seen by the error bar of the outer data point of the 144 MHz brightness profile in Figure 4.8).

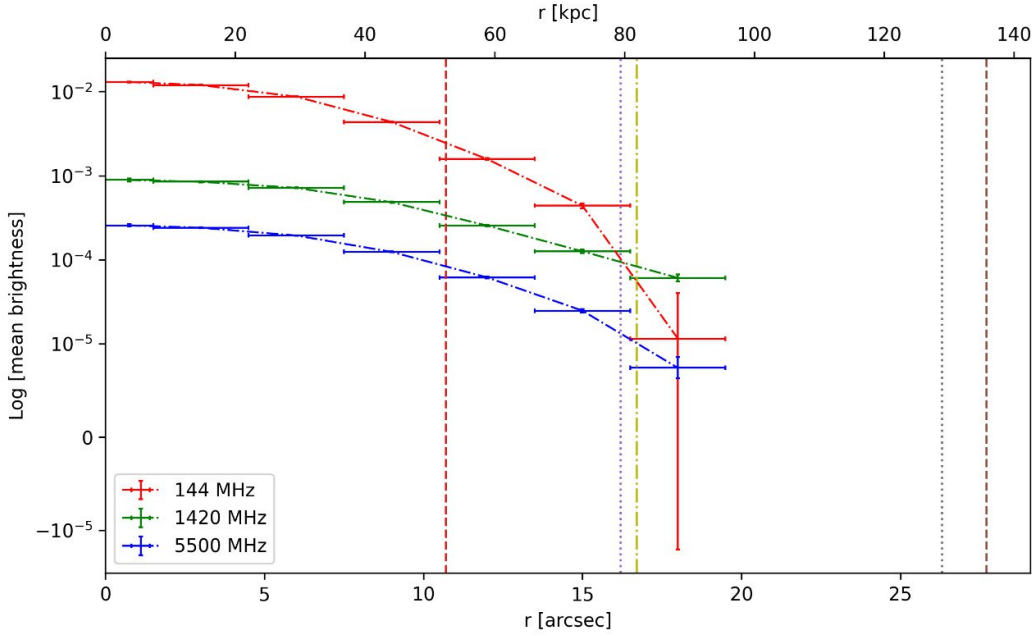

Figure 4.8: Radial brightness profile of the subtracted mini-halo emission in RBS 797, plotted as a function of distance from the centre. The red line shows the brightness profile at 144 MHz, the green line shows the brightness profile at 1.4 GHz, and the blue line shows the brightness profile at 5.5 GHz.

Looking at Figure 4.7 we can clearly see two distinct regions marked by the inner shock at 10″: the central region is the one correspondent to the location of the AGN radio lobes and jets, and it shows the spectral index $\alpha_{1.4\mathrm{GHz}}^{144\mathrm{MHz}}$ as steeper than $\alpha_{5.5\mathrm{GHz}}^{1.4\mathrm{GHz}}$. Outside the inner shock, the data is related only to the diffuse emission of the mini-halo, and there the $\alpha_{1.4\mathrm{GHz}}^{144\mathrm{MHz}}$ spectral index has a flattening trend with respect to the higher frequency range ($\alpha_{5.5\mathrm{GHz}}^{1.4\mathrm{GHz}}$) that becomes steeper towards the outside.

It is clear that the behaviour of the spectral index radial trend cannot be explained by a single electron population. We do not have any model that could describe a single electron population with two radial profiles with opposite trends, with flatter values corresponding to the lower frequency band. Given the complexity of the environment, the hypothesis of two distinct populations could be reasonable, even though it would require an additional component in the model other than the mini-halo plus the AGN; this additional component could derive from the AGN or from the mini-halo itself.

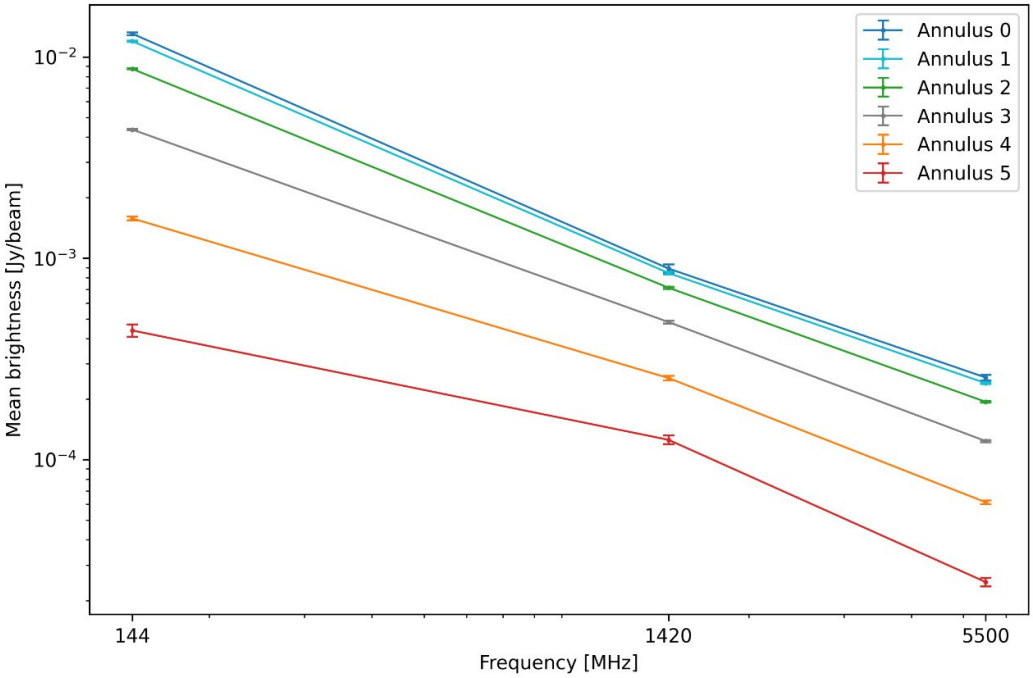

Figure 4.9: Mean brightness as a function of frequency, plotted for each concentric annulus in a logarithmic scale. Annuli $0-3$ are within $10''$ of distance from the centre, a region where the emission of the mini-halo is co-spatial with the emission of the AGN; annuli 4 and 5 are at $r \approx 11''$ and $r \approx 15''$ respectively, in a region where the emission is due only to the mini-halo.

Figure 4.9 shows the mean brightness as a function of frequency computed for each concentric annulus; in addition to Figure 4.7 this plot gives a clear visual understanding of the radial trend of the spectral index. It is evident that the deviation from the typical power law is a radial trend, with the strongest curve found in the outermost rings. The spatial scales corresponding to the two outer rings (annuli 4 and 5) are larger than the AGN extension ($r_{AGN} \approx 10''$), therefore the emission should not be influenced by the central source.

4.3.1 Separated radial profile for the AGN lobes region

A further check for a possible leftover AGN emission was to repeat the computation of the radial profile, this time dividing the area in two conical subregions, one co-spatial with the AGN lobes in the East-West direction, and one where no lobes emission is detected in the North-South direction, as can be seen in Figure 4.10. This test enabled us to check whether there were systematic differences between the two regions that could suggest a correlation between the different trend and a leftover AGN emission.

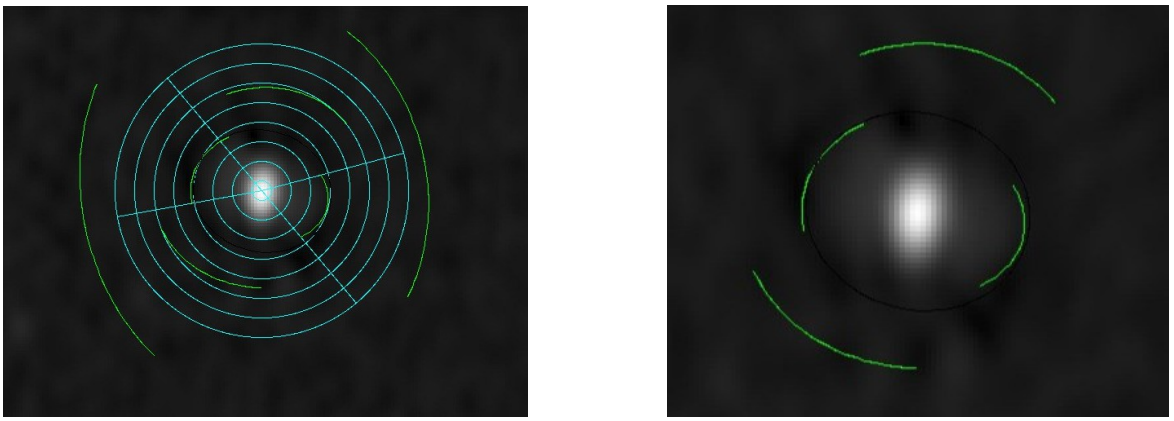

(a) (b)

Figure 4.10: Panel (a): conical subregions drawn onto the image of the compact sources of RBS 797 FOV, overlaid with projected shock fronts detected in Ubertosi et al. (2021).
Panel (b): projected inner and middle shock fronts overlaid onto the image of the compact sources of RBS 797.

We know from Ubertosi et al. (2023) that the AGN lobes emission is confined within the eastern and western inner shock fronts: the conical region co-spatial with the lobes has been drawn therefore within the angular range intersecting the position of the edge of the shocks (shocks' characteristics listed in 2.2, conical regions shown in Figure 4.10). Table 4.2 lists the precise angular ranges of the quadrants corresponding to the two conical regions.

Table 4.2: Angular ranges of conical regions

	$Lobes_W$	$Lobes_E$	$No-lobes_N$	$No-lobes_S$
$\theta_1-\theta_2$	310°-15°	15°-130°	130°-190°	190°-310°

Notes. Column 1: angular range in degrees of western quadrant of the region co-spatial with the lobes emission; column 2: angular range in degrees of eastern quadrant of the lobes region; column 3: angular range in degrees of northern quadrant of the region where no lobes emission is detected; column 4: angular range in degrees of northern quadrant of the region without lobes.

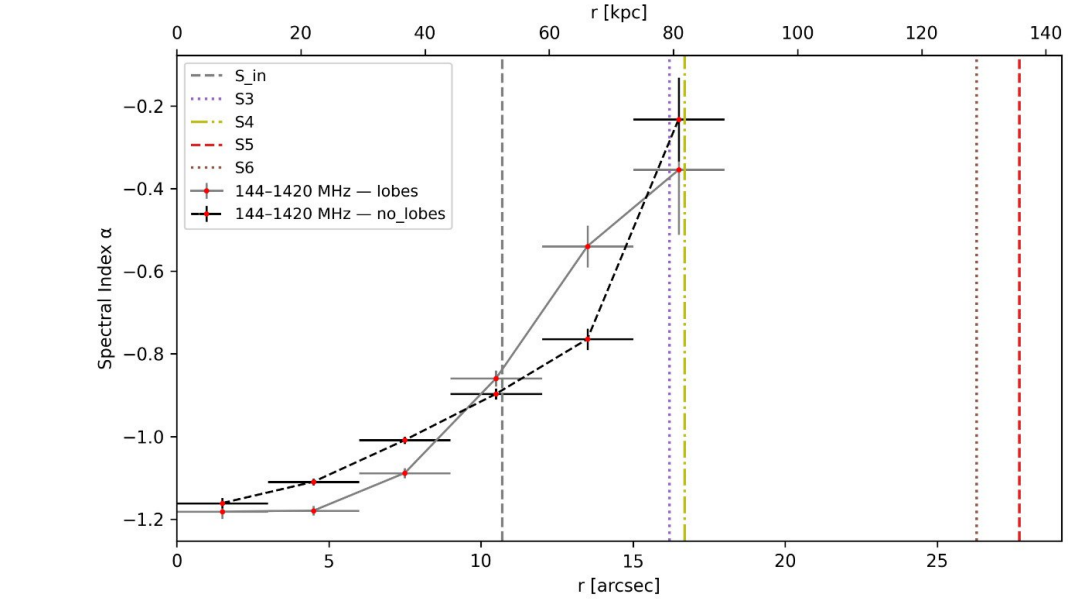

(a)

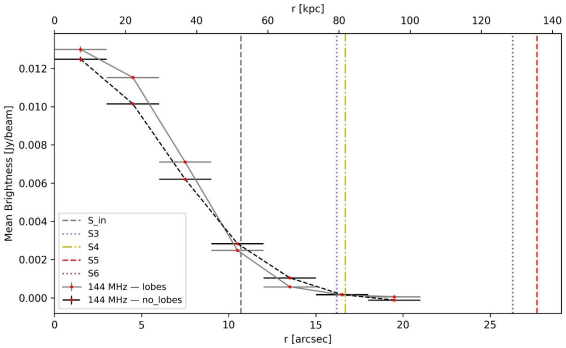

(b)

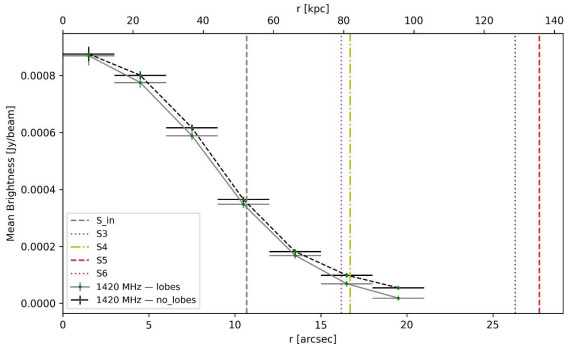

(c)

Figure 4.11: Panel (a): spectral index radial profile between 1.4 GHz and 144 MHz, computed separately in the east–west sector co-spatial with the AGN lobes (gray solid line) and in the north–south sector where no lobe emission is detected (black dotted line). Panel:(b) mean surface-brightness radial profile at 1.4 GHz for the two distinct regions (line colours are the same). Panel (c): mean surface-brightness radial profile at 144 MHz.

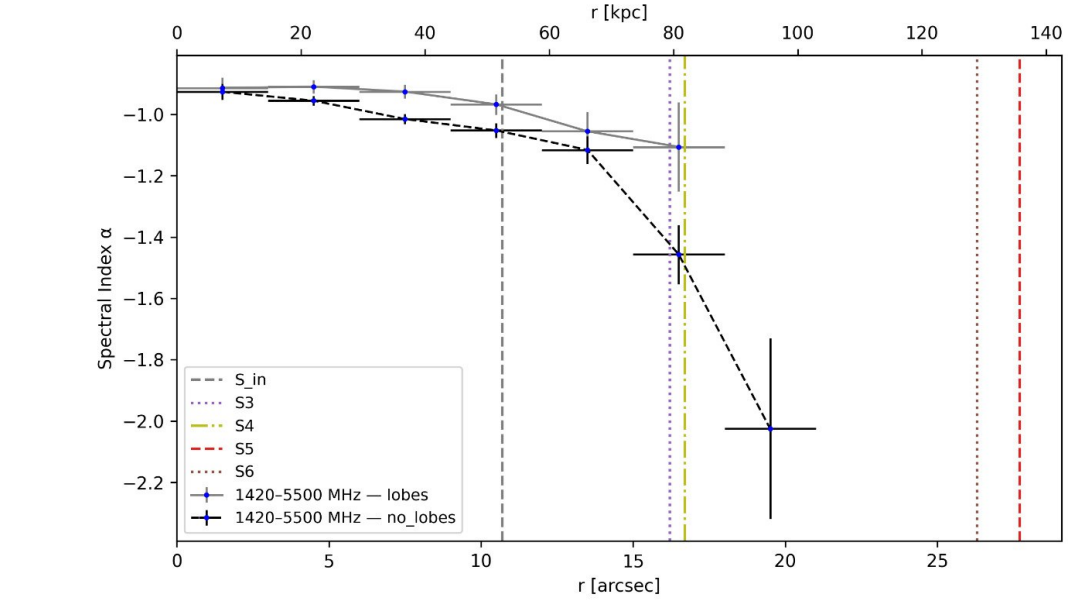

(a)

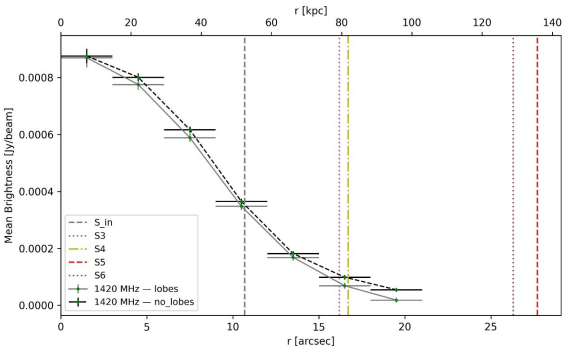

(b)

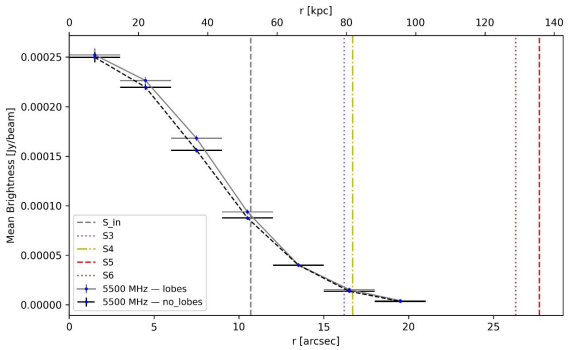

(c)

Figure 4.12: Panel (a): spectral index radial profile between 1.4 GHz and 5.5 GHz, computed separately in the east–west sector co-spatial with the AGN lobes (grey solid line) and in the north–south sector where no lobe emission is detected (black dotted line). Panel:(b) mean surface-brightness radial profile at 1.4 GHz for the two distinct regions (line colours are the same). Panel (c): mean surface-brightness radial profile at 5.5 GHz.

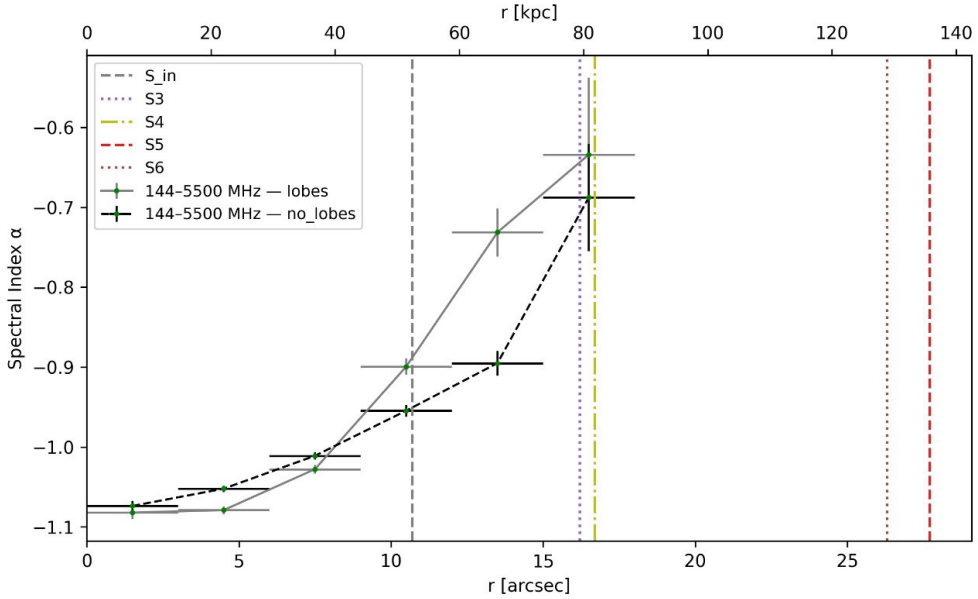

(a)

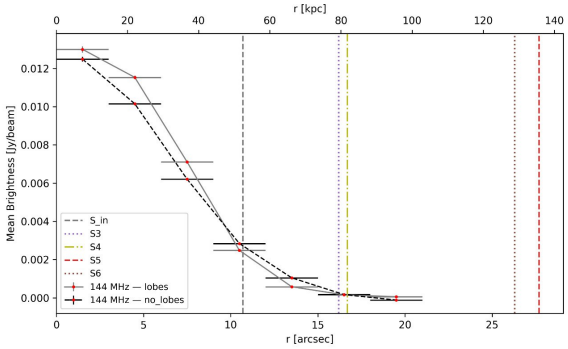

(b)

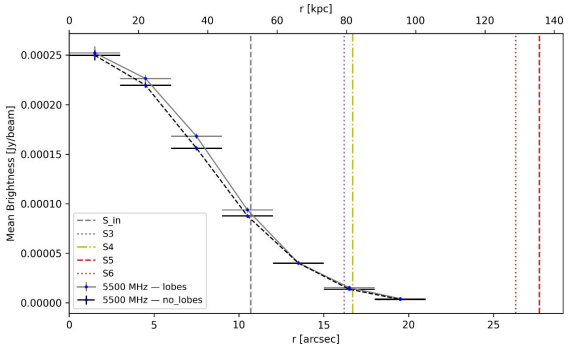

(c) panel (a)

Figure 4.13: Panel (a): spectral index radial profile between 144 MHz and 5.5 GHz, computed separately in the east–west sector co-spatial with the AGN lobes (grey solid line) and in the north–south sector where no lobe emission is detected (black dotted line). Panel:(b) mean surface-brightness radial profile at 144 MHz for the two distinct regions (line colours are the same). Panel (c): mean surface-brightness radial profile at 5.5 GHz.

The trends of the brightness profile and spectral index are similar for the two subregions in all the frequency ranges. The lack of clear systematic differences suggests that the opposite trend of the spectral index radial profile cannot be ascribed to an AGN emission left from the subtraction procedure: if that were the case we would observe a clear flattening in the lobes subregion at all frequencies, and the steepening would be observed in the no-lobes subregion at all frequencies as well. The difference in the radial trend, instead, is not related to the location of the emission, but rather to the frequency range at which the emission is observed. It is interesting to note that the spectral index values in the outer ring of $\alpha_{1.4\mathrm{GHz}}^{144\mathrm{MHz}}$ are very flat, in a region precisely corresponding to the projected distance of the middle shock fronts; despite the region having a low signal-to-noise ratio, the correlation seems present.

4.4 Analytic profile: double fit

To understand what kind of model better describes the emission observed, we performed a double-fit on the central region of RBS 797, within a range of around 30″ from the cluster centre, fitting the brightness distribution of the image with both the mini-halo and the compact sources emission (Figure 3.5); the model used is made of two components, one to account for the unresolved AGN emission in the form of a gaussian function, and one for the mini-halo in the form an exponential profile. The model choice and procedure follow the work done by Bonafede et al. (2023) at frequencies 144 MHz and 1.4 GHz.
The equations are the following:

$$I(r) = I_{MH}(r) + I_{AGN}(r) \tag{4.3}$$

$$I_{MH}(r) = I_0 \, exp^{-(r/r_e)} \tag{4.4}$$

$$I_{AGN}(r) = I_{AGN,0} \, exp^{-(r^2/2\sigma^2_{AGN})} \tag{4.5}$$

where $I_{MH}(r)$ is the mini halo brightness profile, $I_{AGN}(r)$ is the gaussian profile and I_0, $I_{AGN,0}$, σ_{AGN}, r_e are the free parameters of the fit. I_0 and $I_{AGN,0}$ are the central brightness values of the mini-halo and the AGN respectively, σ_{AGN} is the standard deviation of the gaussian profile, and r_e is the e-folding radius of the mini-halo (defined as the radius at which the surface brightness decreases by a factor e with respect to the central value).

Deconvolved double-fit

The observed radio image has a finite angular resolution given by the beamsize, therefore it does not represent the intrinsic sky brightness distribution; as a consequence, intrinsic source properties cannot be measured directly from the image without taking into account this effect.

Since the restoring beam modifies the brightness distribution, it is necessary to first construct a two-dimensional model of the AGN and mini-halo that represents the intrinsic emission, and then convolve it with the beam before averaging the brightness over a one-dimensional radial profile (as explained in Murgia et al. (2009) Bonafede et al. (2023)). This approach ensures that the effects of beam smearing are treated properly; as noted in Peng et al. (2002), convolution alters a two-dimensional brightness distribution in a way that cannot be reproduced by first creating a one-dimensional model and then smoothing it.

The code starts by creating the two-dimensional model of the intrinsic brightness distribution of the source, as it would be without the effect of beam smearing; the model is made of two components, one that describes the AGN profile and one that describes the mini-halo, given by Equation (4.3). The model image is then convolved with a Gaussian kernel that matches the restoring beam, therefore recreating the same instrumental response that affects the data. Once the two-dimensional, convolved,

model image is created, the code produces a one-dimensional radial profile obtained after azimuthally averaging the brightness distribution over concentric annuli.

This one-dimensional averaged model is then compared with the one-dimensional observed radial profile, and the model parameters are tuned until the best fit is found; the model parameters defined in Section 4.4 describe the brightness distribution 'before' the smearing caused by the beam convolution, therefore allowing intrinsic source properties to be inferred while properly accounting for observational effects.

Procedure and results

The observed radial profile was extracted from the image at 5.5 GHz by computing the mean brightness in concentric annuli; the width of the annuli was set to $3.5''$, corresponding to approximately half of the beam FWHM to be able to ensure statistically independent measurements.

Only radial bins with mean surface brightness above a signal-to-noise threshold of $3\sigma_{rms}/\sqrt{N_{beams}}$ were included in the fit, where σ_{rms} is the image noise and N_{beams} is the number of independent beams within each annulus. In addition, the fit was restricted to radii where the mini-halo emission is detected, excluding outer regions dominated by noise fluctuations.

The best-fit parameters shown in Table 4.3 were obtained through non-linear least-squares minimization, and they provide the quantities that describe the two components (the intrinsic values before the beam convolution). Figure 4.14 shows the result of the fit compared with the archival work produced by Bonafede et al. (2023) at 144 MHz and 1.4 GHz.

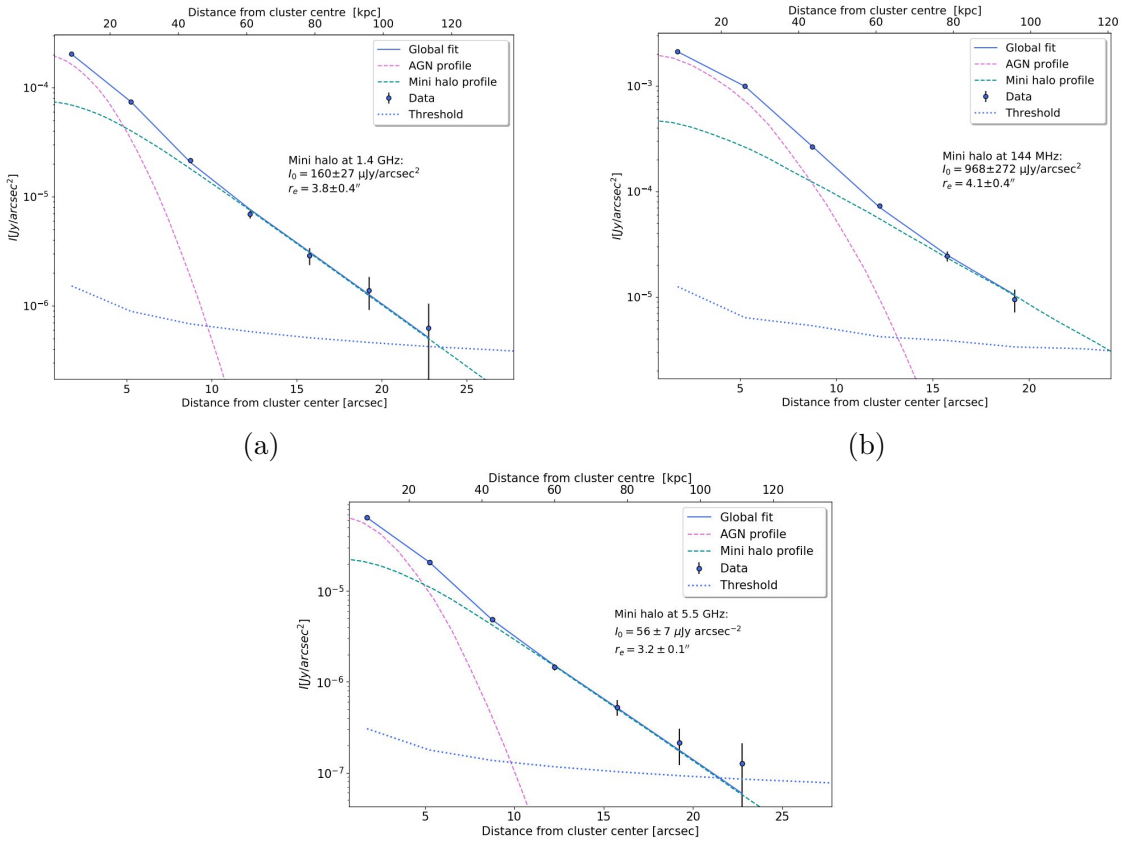

Figure 4.14: Exponential plus Gaussian decomposition of the azimuthally averaged radio surface-brightness profiles of RBS 797. Panels (a) and (b) show the JVLA 1.4 GHz and LOFAR profiles, respectively, reproduced from Bonafede et al. (2023), while panel (c) shows the JVLA 5.5 GHz profile derived and analysed in this thesis. Blue points represent the mean surface brightness measured in concentric annuli. The solid blue line indicates the total best-fit model, while the dashed lines shows the individual AGN (Gaussian) and mini-halo (exponential) components. The dotted line marks the detection threshold defined as $3\sigma_{\rm rms}/\sqrt{N_{\rm beams}}$, where $N_{\rm beams}$ is the number of independent beams within each annulus. Best-fit parameters are reported in Table 4.3.

Table 4.3: Best-fit parameters of the mini-halo and central AGN at 5.5 GHz.

I_0 (μJy arcsec^{-2})	$I_{\rm AGN}$ (μJy arcsec^{-2})	r_e (arcsec)	$\sigma_{\rm AGN}$ (arcsec)	χ^2_r
55.6 ± 7.2	825.5 ± 253.5	3.18 ± 0.15	0.76 ± 0.14	0.36

Notes. Col. 1: central surface brightness of the mini-halo (I_0); col. 2: central surface brightness of the Gaussian AGN component; col. 3: e-folding radius of the exponential mini-halo profile; col. 4: Gaussian standard deviation of the AGN component; col. 5: reduced chi-square of the fit.

We compare the values of the central brightness, e-folding radius, and flux within three times the e-folding radius of the mini-halo with the ones listed in Bonafede et al. (2023) ($I_{\rm AGN}$ and $\sigma_{\rm AGN}$ are not reported in the paper). Results are listed in Table 4.4.

Table 4.4: Exponential fit results comparison

Observation	$I_{0,\mathrm{MH}}$	$r_e(arcsec)$	S_{3r_e} (mJy)	χ^2_r
LOFAR-144MHz	970 ± 270	$4.1 \pm 0.4''$	82 ± 23	0.9
VLA-1.4GHz	160 ± 27	$3.8 \pm 0.4''$	11 ± 2	1.2
VLA-5.5GHz	55.6 ± 7.2	$3.2 \pm 0.1''$	2.8 ± 0.3	0.3

Notes. Column 1: observing instrument and frequency. Column 2: central surface brightness of the mini-halo (μJy arcsec^{-2}). Column 3: e-folding radius of the exponential profile. Column 4: mini-halo flux density integrated within $3r_e$. Column 5: reduced chi-square of the fit.

The value of the e-folding radius is consistent with the values provided by the previous work. Even more notably, the chi-squared of the fitting is very good, as also seen in the previous tests at 144 MHz and 1425 MHz. This result shows that the model fitting of the brightness distribution doesn't require the additional component theorized in Section 4.3, describing the data very well with only the mini-halo and the central AGN. This fit does not help us constrain what this component could be, or if it is even needed; nonetheless, the results of the spectral analysis clearly highlight the limits of the single population model.

4.5 Spectral Index comparison

The model for the mini-halo emission is an exponential profile of the kind

$$I_{\mathrm{MH}}(r) = I_0\, e^{-r/r_e} \tag{4.6}$$

with I_0 being the central brightness of the mini-halo and r_e being the e-folding radius.

The Flux density within a given radius R is given by :

$$S_{\mathrm{MH}}(< R) = 2\pi \int_0^R I_0\, e^{-r/r_e}\, r\, dr \tag{4.7}$$

which, for the case of $R = 3r_e$, gives the flux of the mini-halo within three times the e-folding radius.

This value can be used to compute another estimate of the fitted spectral index for the three frequencies, and compare it to the one computed with the values of integrated flux density extracted from the subtracted images (see Section 4.1).

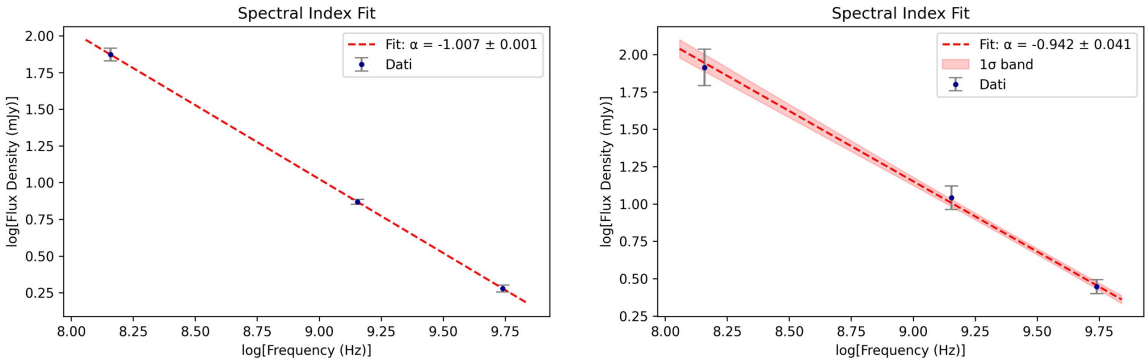

(a) (b)

Figure 4.15: Spectral index fit comparison for the mini-halo emission of RBS 797. Panel (a): spectral index computed with values of integrated flux density extracted from the subtracted images of the mini-halo at 144 MHz, 1.4 GHz and 5.5 GHz; values of the integrated flux density for the three frequencies are listed in table 4.1.
Panel (b): spectral index computed from values of flux density integrated within $3r_e$, given as a result of the double-component fit seen in section 4.4; values of flux density within $3r_e$ for the three frequencies are listed in table 4.4.

Table 4.5: Spectral Index fit comparison

Method	$S_{144\,MHz}$ (mJy)	$S_{1.4\,GHz}$ (mJy)	$S_{5.5\,GHz}$ (mJy)	α_{fit}	χ^2
Subtracted image	74.6 ± 7.4	7.4 ± 0.3	1.9 ± 0.1	-1.007 ± 0.001	0.001
Double-fit	82 ± 23	11 ± 2	2.8 ± 0.3	-0.942 ± 0.041	0.279

Notes. Column 1: method used to compute the flux density of the mini-halo; column 2 and 3 and 4: flux density values at 144 MHz 1.4 GHz and 5.5 GHz ; column 5: best-fit spectral index value (for the subtracted images the spectral index was computed considering only emission detected above 3σ for all frequencies); column 6: reduced chi-square of the fit.

The resulting value is $\alpha = -0.942 \pm 0.041$, very compatible within uncertainties with the previous result, as shown in Figure 4.15 and Table 4.5. This confirms that the spectral profile of the integrated mini-halo emission is well represented by a power law even up to frequencies of 5.5 GHz, a frequency range not frequently explored in mini-halo studies that usually have measurements around 1 GHz. Moreover, the compatibility of the results proves that the discrete source subtraction was performed reasonably well.

4.6 Radiative age constraints

To better understand the origin of the radio emission, it is useful to estimate the radiative loss timescale of the relativistic electrons, which gives an indication of how long the particles can emit before losing energy through synchrotron and Inverse-Compton losses (see Section 1.2.1). The resulting timescale can then be used as a comparison

with the radiative ages of the AGN-driven shocks observed in the cluster (as computed in the work of Ubertosi et al. (2023)) in order to check whether there may be a connection between the AGN feedback and the re-acceleration of the emitting particles.

The integrated radio spectrum of the diffuse emission is well described by a single power law between 144 MHz and 5.5 GHz, with spectral index values of $\alpha = -1.007 \pm 0.001$ (computed within 3σ of the subtracted images), and of $\alpha = -0.942 \pm 0.041$ (computed within $3r_e$ by the double-component fit). No evidence for spectral curvature is observed within the explored frequency range. On the other hand, the results of the spatially resolved spectral analysis show that the central region of the mini-halo (up to $\sim 10''$) has a power-law type spectrum consistent with the integrated spectrum, while the outer region up to $15'' - 16''$ shows a steepening in the $1.4 - 5.5\,\mathrm{GHz}$ frequency range Figure 4.9.

For the region within $\sim 10''$ we can assume, within the uncertainties of our spectral index fit, that if a spectral break is present it must occur at higher frequencies, i.e. $\nu_b > 5.5$ GHz.

For the outer regions at $15'' - 16''$, we can assume $\nu = 1.4$GHz to be the break frequency.

In standard synchrotron-loss theory (Pacholczyk 1970 sec 6.2), radiative losses due to synchrotron emission and Inverse-Compton scattering off the cosmic microwave background (CMB) produce a characteristic break frequency in the radio spectrum of a population of relativistic electrons (see Section 1.2.1). The break frequency depends on the magnetic field strength and on the radiative age of the electron population as

$$\nu_b \propto \frac{B}{(B^2 + B_{CMB}^2)^2 t^2}, \tag{4.8}$$

where B is the magnetic field strength and $B_{CMB} = 3.25(1+z)^2$ μG represents the equivalent magnetic field of the CMB (Van Weeren et al., 2019).

The associated synchrotron plus Inverse-Compton radiative-loss timescale can be written as

$$t_{rad} = 1.61 \times 10^3 \frac{\sqrt{B_{\mu G}}}{B_{\mu G}^2 + B_{CMB,\mu G}^2} \frac{1}{\sqrt{(1+z)\nu_{GHz}}} \text{ Myr} \tag{4.9}$$

(Parma et al., 1998).

For a fixed break frequency, the radiative lifetime is maximized when $B = B_{CMB}/\sqrt{3}$, which therefore provides a conservative estimate of the electron lifetime.

At the cluster redshift $z = 0.354$, the equivalent CMB magnetic field is

$$B_{CMB} \simeq 5.96\,\mu\mathrm{G}$$

which results in

$$B = \frac{B_{CMB}}{\sqrt{3}} \simeq 3.44\,\mu\mathrm{G},$$

Although magnetic fields in cool core clusters are largely unconstrained, having a central magnetic field $B > B_{CBR}\sqrt{3} \sim 3.44\mu G$ at the redshift of RBS 797, is in

agreement with current works (e.g., Taylor et al. 2002; Bonafede et al. 2011; Vacca et al. 2012; Osinga et al. 2022).

We can therefore constrain the radiative lifetime of the regions discussed, using the values of the break frequency deduced from the spectral analysis.

For the region within $10''$ (where the integrated spectrum does not show evidence of spectral steepening), we can adopt the conservative magnetic field value that maximizes the radiative lifetime, and assume a break frequency $\nu_b > 5.5$ GHz, to infer an upper limit on the radiative lifetime; this limit must not be interpreted as the physical age of the mini-halo but rather as the time passed since the last significant event of re-acceleration or particle injection.

Equation 4.9 yields an upper limit on the synchrotron plus inverse-Compton radiative-loss timescale

$$t_{rad} \lesssim 23 \text{ Myr}.$$

The region within $10''$, corresponding to projected distances $r \lesssim 50$ kpc from the cluster centre, interestingly, is comparable to the position of the innermost X-ray shock detected in RBS 797 in the work of Ubertosi et al. (2023). The age of this shock, derived from X-ray observations, is estimated to be $t_{sh} \sim 30$ Myr (see Table 2.2 for detailed shocks properties). The radiative-loss constraint $t_{rad} \lesssim 23$ Myr derived from the integrated radio spectrum is therefore broadly consistent with the dynamical timescale of the innermost shock.

At larger radii, the radial spectral profiles begin to steepen in correspondence to a spectral break of around $\nu_b \sim 1.4$ GHz, in the region at $10'' - 16''$, corresponding to projected distances of approximately $50 - 80$ kpc from the cluster centre. Equation 4.9 gives a radiative timescale of approximately

$$t_{rad} \sim 46 \text{ Myr}.$$

This region lies immediately behind the middle shock identified in the X-ray observations, whose estimated age is $t_{sh} \sim 55$ Myr (see Table 2.2). Within the uncertainties of the spectral measurements and of the assumed magnetic field strength, the radiative-loss timescale inferred from the radio spectrum is therefore compatible with the dynamical age of the shock.

Given the limitations of the method used and the assumptions made necessary, the results are still compatible with the values inferred in the work of Ubertosi et al. (2023), suggesting that, although the shocks are unlikely to be responsible for the origin of the mini-halo itself, they may still have an influence on the mini-halo emission, modifying its spectral properties.

Chapter 5

Conclusions and Future prospects

5.1 Conclusions

This thesis investigated the radio mini-halo in the cool-core galaxy cluster RBS 797, with the goal of extending the spectral coverage to higher frequencies and computing both integrated and spatially resolved spectral analysis to constrain the physical processes responsible for the diffuse emission. New JVLA C-band data were combined with archival LOFAR 144MHz and VLA 1.4GHz observations.

Care was taken to disentangle the mini-halo emission from the central AGN and other compact sources present in the FOV of the centre of RBS 797.

It was also ensured that the images used for the spectral analysis were comparable, matching the angular resolution and UV-range at the different frequencies.

The main results of this work can be summarized as follows:

- *Morphology and flux after subtraction of the compact sources.* We successfully subtracted the central compact sources, obtaining images of the mini-halo emission imaged both with and without tapering. The integrated flux density within $3\sigma_{rms}$ of the tapered image is 2.05 ± 0.10mJy, with $\sigma_{rms} = 3.7\,\mu$Jy/beam. The morphology is centrally symmetric, with the largest angular scale equal to $41.8''$ in the EW direction and $41.4''$ in the NS direction, corresponding respectively to 205 kpc and 203 kpc at the cluster redshift. For the high-resolution image, the morphology turned out slightly less centrally symmetric, with maximum extension in the EW direction being $30.5''$ and in the NS direction being $33.7''$. The integrated flux density within $3\sigma_{rms}$ is 1.96 ± 0.10mJy, with $\sigma_{rms} = 3.9\,\mu$Jy/beam, showing that the flux density value is consistent with and without tapering.

- *Power-law from integrated spectral index fit.* We combined the image at 5.5GHz with archival images at 144MHz and 1.4GHz. We set the same angular resolution and UV-range, we extracted the integrated flux density within a region with emission above 3σ for all frequencies, and computed the spectral index profile. The resulting fit is consistent with a single power law with $\alpha = -1.007 \pm 0.001$ ($S_\nu \propto \nu^\alpha$), showing no evidence for curvature within the available frequency range.

- *Contrasting radial trend from spatially resolved spectral index analysis.* We computed spectral-index maps, and radial profiles of the spectral index, between the

three frequency ranges available: $144-1425$ MHz, $1425-5500$ MHz and $144-5500$ MHz. The results showed that the low-frequency range ($144-1425$ MHz) confirms the flattening radial trend found in Bonafede et al. (2023) work, while the higher-frequency range ($1.4-5.5$ GHz) has an opposite radial trend, showing a steepening towards the outskirts with the exception of an azimuthal fluctuation of flatter values in the EW direction. A consequent test for the radial profile was done, separating a conical region co-spatial with the AGN lobes from a region without detected lobe emission. The results led to the conclusion that the difference in the radial trend is not related to the location of the emission, but rather to the frequency range at which the emission is observed. This confirms that the contrasting trend cannot be ascribed to an AGN emission left from the subtraction procedure. The radial profile shows two distinct regions with different behaviour, one within $10''$ correspondent to the AGN extension, and one from $10''$ to $\sim 16''$ corresponding to the region where the mini-halo emission dominates. The speculation is that an additional electron population is needed to explain the observed behaviour of the spectral index at different frequency bands.

- *Two-component deconvolved fit optimally reproducing the surface-brightness distribution.* We looked for a model that could fit the surface-brightness profile of the centre of RBS 797. At 5.5GHz, the observed azimuthally averaged brightness profile is very well described by the sum of a Gaussian component (central AGN) and an exponential profile (mini-halo). This is consistent with the results found in Bonafede et al. (2023) work at 144MHz and 1.4GHz. The best-fit e-folding radius at 5.5GHz is $r_e = 3.18 \pm 0.15''$, consistent with the values of the model at lower frequencies, and the optimal fit quality suggests that the data do not need additional components to describe the brightness distribution.

- *Integrated spectral index fit comparison.* We used the values of flux density integrated within 3 times the e-folding radius, given by the double-component fit, to compute an additional estimate of the integrated spectral index. The result is $\alpha = -0.94 \pm 0.04$, consistent with $\alpha = -1.007 \pm 0.001$, value computed by extracting the integrated flux density from the subtracted images; this confirms that the AGN emission has been subtracted with good accuracy and is not affecting the spectral index results.

- *Radiative age constraints.* We constrained the radiative lifetime of the electrons producing the radio emission, following the relation $t_{rad} \propto \frac{\sqrt{B_{\mu G}}}{B_{\mu G}^2 + B_{CMB,\mu G}^2}$. We assumed a conservative estimate of the cluster magnetic field, $B = B_{CMB}/\sqrt{3}$, which maximizes the radiative lifetime. This resulted in $t_{rad} \lesssim 23$ Myr in the region within $10''$, corresponding to a projected distance $r \lesssim 50$ kpc from the cluster centre, and $t_{rad} \sim 46$ Myr for the region at $10'' - 16''$, corresponding to projected distances of approximately $50 - 80$ kpc from the cluster centre. These regions lie immediately behind the inner and middle shock, respectively, as detected in the X-ray emission, and the timescales are comparable: the inner shock's estimated age is $t \sim 30$ Myr, while the middle shock's estimated age is $t \sim 55$ Myr. We concluded that, although the AGN is not likely to be responsible

for the origin of the mini-halo, it may have a role in modifying its spectral properties.

RBS 797 was the first case of a mini-halo that showed a spectral radial flattening, suggesting, as a possible origin of the emission, a re-acceleration scenario driven by the AGN-driven shocks co-spatial with the mini-halo emission.

The spectral steepening at high frequency, on the other hand, is a feature observed in a few mini-halos, and it is interpreted as turbulent re-acceleration, theorized in Gitti et al. (2002), where the re-acceleration of the electrons is produced by the MHD turbulence in the cool core.

Detailed modelling in Bonafede et al. (2023) suggested that shock re-acceleration alone could not fully reproduce the smooth mini-halo profile. The spectral steepening observed in the mini-halo therefore reinforces the turbulent re-acceleration scenario.

The co-presence of both a spectral steepening at high frequencies and a flattening at low frequencies is a feature unique to RBS 797, never observed in other mini-halos before; few mini-halo studies, though, are performed within the same range of high frequencies we analyzed.

The observed spectral index trend remains a feature yet to be explained, suggesting that the observed complexity could be due to a combination of both AGN-driven feedback and ICM dynamics.

This new discovery points to the limits of the models we have thus far theorized to describe mini-halos, objects that we are still far from having fully understood.

5.2 Future prospects

Future progress could be achieved in many ways: additional data at multiple frequencies ranges would help search for spectral curvature, especially looking at higher frequencies; data at lower frequencies (between 144MHz and 1.4GHz) would help better understand the nature of the anomalous flattening of the spectral index radial profile; finally, better sensitivity in the peripheral regions of the diffuse emission could help provide additional data for the computation of the spectral index, and study the localized spectral features in more detail.

Another test of the different models could be provided by obtaining constraints on the mini-halo polarization properties and on the cluster's magnetic field. Unless the magnetic field in the centre were larger than $15\,\mu G$, the central AGN feedback would necessarily have a role in shaping the spectral properties of the mini-halo. A high polarization degree would then point to a shock-driven compression of the plasma. Gitti et al. (2006) reported the detection of polarized emission at 1.425 GHz in a region extending up to $10'' \times 15''$.

It could also be useful to compare these observations with simulations that include turbulence, AGN feedback, and the re-acceleration of seed electron populations, to help clarify the roles of shocks, AGN feedback and ICM dynamics in shaping the mini-halo emission in RBS 797.

Appendix A

Theory of synchrotron

The main process that produces radio waves in the Universe is called 'synchrotron emission': it was observed for the first time in 1948 at the synchrotron particle accelerator of General Electrics Entrerprise, from which it took the name, and it was the consequence of electrons being accelerated at very high energies in a magnetic field (Fanti and Fanti, 2012); the emission produced was very intense and strongly polarized, and in that case it peaked at optical wavelength. Since radio sources in the universe have magnetic fields that are much weaker, the produced emission peaks at much longer wavelengths (i.e lower frequencies as given by eq. A.3), predominantly in the radio band.

A non-relativistic electrically charged particle with charge q and momentum $\vec{p}$, subject to acceleration, produces a radiated power given by the Larmor formula:

$$w(t) = -\frac{d\epsilon}{dt} = \frac{2}{3}\frac{q^2}{m^2c^3}(\frac{d\vec{p}}{dt})^2 \tag{A.1}$$

which has an angular distribution per unit of solid angle given by the formula of the electric dipole

$$\frac{dw}{d\Omega} = -\frac{1q^2}{4\pi c^3}\vec{a}^2 sin^2(\theta) \tag{A.2}$$

with θ being the angle between a chosen direction and the acceleration vector $\vec{a}$ as shown in Figure A.1.

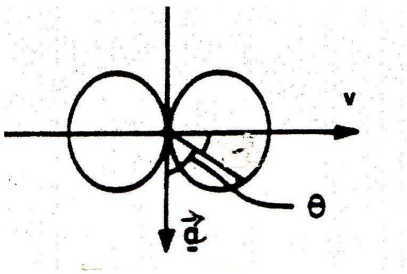

Figure A.1: Angular distribution per unit solid angle of radiated power from a non-relativistic particle. Credit: Fanti and Fanti (2012).

For the case of synchrotron emission the charged particle is accelerated by rotation along magnetic field lines, and it is always relativistic, with a Lorentz factor $\gamma \gg 1$: therefore the angular distribution has the shape of the classic electric dipole only in the rest-frame of the particle; from an external observer half of the emission is 'Doppler-boosted' along the line of sight in the shape of a cone of $2/\gamma$ amplitude with central axis parallel to the instantaneous orbital velocity vector (see Figure A.2).

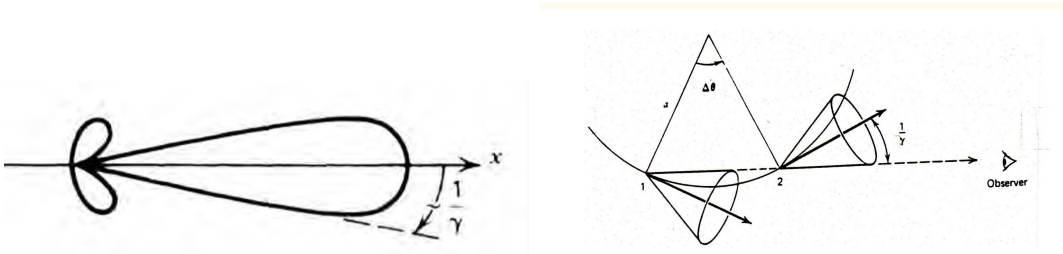

Figure A.2: Left panel: angular distribution per unit solid angle of power radiated by a relativistic particle. Right panel: geometric representation of emission along the particle's orbit concentrated in a cone with semi-amplitude $1/\gamma$ with axis parallel to the direction of instantaneous velocity $\vec{v}$. Credit: (Fanti and Fanti, 2012)

The orbit of the particle has an elicoidal shape with axis parallel to the magnetic field lines and the emission cone intercepts the l.o.s only for finite intervals of time: the effect is an impulse type radiation that has a limited spectral distribution (power emitted per unit of frequency interval) with a characteristic critical frequency given by Equation (A.3) (Fanti and Fanti, 2012):

$$\nu_s \sim \frac{3}{4\pi}\frac{1}{\tau} = \frac{3}{4\pi}\frac{eH}{m_e^3 c^5}\epsilon^2 = 6.24 \times 10^{18}\epsilon^2 H\nu_s(GHz) \approx 4.2 \times 10^{-9}\gamma^2 H(\mu G) \qquad \text{(A.3)}$$

For typical astronomical values of $H \sim 10\mu G, \gamma \sim 10^4$ the characteristic frequency is $\nu_s \sim 4.2$ GHz, a typical frequency of radioastronomy (Fanti and Fanti, 2012).

The total emission produced by a population of electrons does not follow the shape of the power spectrum of the individual electron: it can be considered as the overlap of all the individual emissions of the particles composing the population, with the shape of a power law (eq. A.4).

$$J_s \propto \nu^{-(\delta-1)/2} = \nu^{-\alpha}. \qquad \text{(A.4)}$$

The quantity α is known as the spectral index, defined as $\alpha = \dfrac{\delta - 1}{2}$; the most frequent value observed in radio-sources is $\alpha \sim 0.75$ ($\delta = 2.5$) (Fanti and Fanti, 2012).

Polarization

Synchrotron emission is naturally linearly polarized.

$$P_{lin} = \frac{P}{I} = \frac{3\delta + 3}{3\delta + 7} = 0.7 \qquad \text{(A.5)}$$

with $2 \leq \delta \leq 4$, and P equal to the total polarized signal and I to the total emitted signal. 80% of polarized signal is therefore a theoretical limit for synchrotron emission.

The observed values are yet much lower than these limits due to depolarization: in clusters, the tangled nature of the magnetic field and Faraday depolarization along the line of sight always reduce the observed polarization.

Appendix B

Radio telescopes: Single dish and principles of Interferometry

Unlike an optical telescope that measures sky brightness directly, a radio telescope measures the voltage of the radio electromagnetic signal received; the process of turning the signal into an image of the radio source is one of the main tasks of the radio astronomer. The main instrument of a radio telescope is an antenna: it is a dipole receiver that converts electromagnetic waves into an electric current, positioned in the focus of a paraboloid collector that acts as the mirror of the antenna. A single dish radio telescope has only one antenna, whereas an interferometer is a system of multiple antennae that allows the sampling of the sky brightness distribution on angular scales much smaller than those obtainable with a single antenna.

B.1 Single dish response

The most basic configuration for a radio telescope is a single dish: one paraboloidal reflector with an antenna positioned in its primary or secondary focus. Electromagnetic waves are turned into current by the dipole receiver and the power pattern of the accelerating electric particles is the same as that of the Larmor radiation. The Power pattern is the distribution of power as a function of the angle, which for the Larmor formula has a toroidal shape and an emission along the longitudinal axis equal to

$$P \sim sin^2(\theta)$$

(National Radio Astronomy Observatory, 2024) with θ being the angle between a chosen direction and the acceleration vector.

A fundamental concept in radioastronomy is the reciprocity theorem, which states that the power pattern of an antenna is the same for transmitting and receiving. An antenna can be treated either as a receiving device or a transmitting system but while the power of a receiving antenna is measured by the Effective collective area A_e, it is easier to compute the Gain of a transmitting antenna $G(\theta, \phi)$ which is defined as the power transmitted per unit solid angle by an ideal isotropic antenna. With the reciprocity theorem, the two power patterns are considered equal, and the quantities are used interchangeably via the relation

$$A_e = \lambda^2 G(\theta, \phi)/4\pi$$

.

Given a plane wave front perpendicular to the normal of the reflector, the rays converge to the focus and, even if the electromagnetic fields are oscillating, the phases of the field vectors are aligned and the paraboloidal structure keeps the phase alignment. True sources actually produce spherical waves, so the approximation to a plane wave can occur only if the source is distant enough and the radius of curvature is very big: this condition is always true for astronomical sources, so we can always make the approximation of a source at infinity (far field approximation).

We define the aperture of a reflector as the imaginary circular plane with diameter D through which the rays pass. We can then determine the power pattern of the single dish antenna with the "far field" approximation and the assumption of a uniformly illuminated aperture.

For the reciprocity theorem, we can study the electric field pattern of a transmitting antenna, knowing that it is equivalent to the receiving antenna. Integrating over the aperture the total electric field will be

$$f(l) = \int_{aperture} g(u) e^{-i2\pi lu} du$$

with $u = x/\lambda$ indicating the position along the aperture in units of wavelength. Knowing that outside the aperture the integral is zero we can integrate over infinite

$$f(l) = \int_{-\infty}^{+\infty} g(u) e^{-i2\pi lu} du$$

which shows that the electric field pattern f(l) of the antenna is the Fourier Transform (FT) of the field distribution illuminating the antenna. We therefore know that it is true also for the receiving antenna that the received electric field is the FT of the far field.

For the uniformly illuminated aperture, the electric field pattern $f(l)$ is a sine-type function

$$f(l) = sinc(l)$$

and the power pattern is the square of the field pattern

$$p(l) = sinc^2(l)$$

The power pattern, shown in Figure B.1, has a Gaussian-like primary maximum, called the "main lobe" or "primary beam" and it is the region where the antenna has the major impulse response. The external peaks are the regions of impulse response outside the main beam and are called "side-lobes".

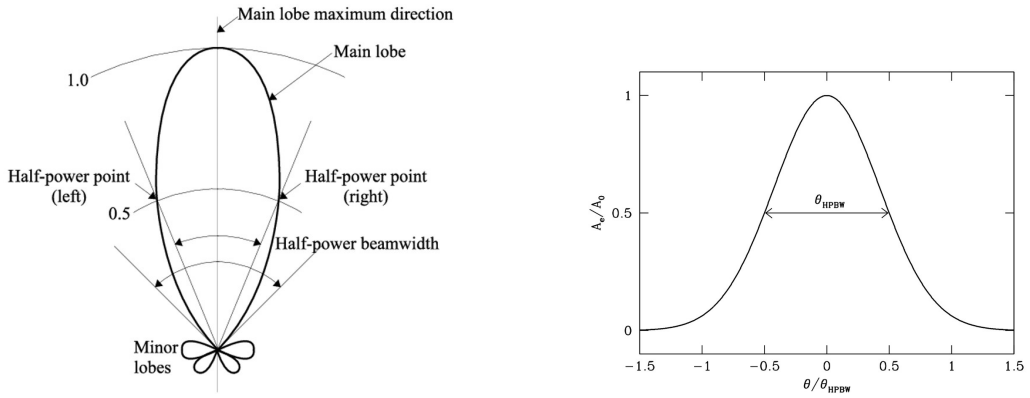

Figure B.1: Left panel: beam of a single-dish antenna, characterised by a main lobe and minor sidelobes; the half-power beam width is the angular size of the main lobe. Right panel: one-dimensional representation of a Gaussian beam, with the beamwidth identified by the angular separation between the half-power points θ_{HPBW}. The axes show the offset θ from the beam centre (in units of the HPBW) on the abscissa and the effective aperture A_e normalised to the peak effective aperture A_0 on the ordinate. Credits: (Zúñiga et al., 2009; National Radio Astronomy Observatory, 2024).

B.1.1 Angular Resolution of Single Dish Telescope

The angular resolution of the single dish radiotelescope is determined by the width of its primary beam, precisely the value of width corresponding to half of the power (so half of the primary beam maximum) as shown in fig. B.1. It is called Half Power Beam Width (HPBW) or Full Width at Half Maximum (FWHM). For a uniformly illuminated aperture of diameter D the angular resolution given by the Rayleigh criterion of diffraction is

$$\theta_{HPBW} \approx 0.89 \times \frac{\lambda}{D}$$

The ideal HPBW in astronomical applications is small enough to resolve different sources (two sources are resolved if the angular distance between two objects is large enough that they can be seen as separated) and has small side lobes to minimise the pickup of stray radiation. The angular resolution increases with bigger values of aperture diameter, therefore the single dish radio-telescope has limited resolution power due to the construction complications of building bigger paraboloidal reflectors.

The minima of the power pattern are called nulls. The angular distance between the first nulls is called Beam Width between First Nulls (BWFN), a value bigger than the HPBW and given by

$$\theta_{BWFN} = 2 \times \frac{\lambda}{D}$$

The beam width determines also the Field of View (FOV), which is the size of the section of the sky that is being observed: it's defined by the width between the first nulls, so approximately by θ_{HPBW} . In this case then, a smaller aperture diameter gives a bigger beam width and therefore a bigger FOV. The limitation of the single dish is dictated by the compromise between decent angular resolution and FOV size; whether one or the other is to be prioritized depends on the scientific aim of the observation.

B.2 Aperture Synthesis or Interferometry

As we have illustrated in section B.1.1, the beam width of a single-dish observation increases with wavelength (λ) and decreases with the diameter (D) of the antenna. For this reason, radio and sub-mm observations have typically poor resolution, compared with optical observations, because the value of λ is larger by several orders of magnitude. To achieve better angular resolutions, one has to either increase the diameter of the telescope further, which is not practical, or decrease the observing wavelength, which leads a loss of information and poorer resolution.

To solve the problem, radio astronomers use the signals from two or more physically separated antennas and then combine it through interferometry. Interferometry is a technique based on the principle of interference of incoming electromagnetic waves and it involves a coherent arrangement of sky signals received by two or more physically separated antennas pointed to the same object (Thompson et al., 2017). With this technique, it is possible to achieve a resolution that emulates the effect of having a radio telescope with a larger diameter.
Aperture synthesis means combining observations taken at different times by interferometry in such a way as to simulate the observation that could be made at one time with a large aperture configuration (Sullivan, 2004).
The distance between antennas in an interferometer is called baseline, and the angular resolution of the interferometer does not depend on the diameter of the individual antenna reflector but on the maximum distance between two antennas in the configuration.

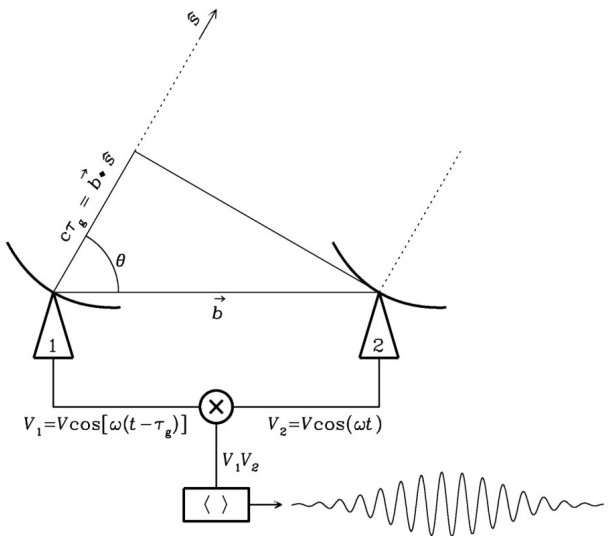

Figure B.2: Schematic representation of a two-element radio interferometer. The signals received by the two antennas are combined in a correlator after compensating for the geometric delay due to the source direction. Adapted from National Radio Astronomy Observatory (2024).

Figure B.2 shows a 2-elements interferometer. The antennas in the figure observe the same source but the signal is received at different times by the two elements: the signal arriving at antenna 1 experiences a geometrical delay given by $\tau_g = bs_0/c$,

where s_0 is the position observed by the antennas and c is the light-speed; it is therefore necessary to take this delay into account by applying an artificial delay to the signal path of antenna 2, so that the signals from both antennas arrive at the correlator with the same phase. At this point, the two voltage outputs are correlated: the correlator multiplies and time-averages the signals coming from the two receivers.

Whereas a two-element interferometer produces a single response, a multi-element interferometer of N antennas produces $N\frac{N-1}{2}$ responses, each corresponding to a baseline connecting a pair of antennas.

Each interferometer pair of the array has its own sinusoidal power response so in total there are $N\frac{N-1}{2}$ pairs; the power response of the multi-element interferometer is called the synthesised beam and it is the arithmetic mean of the individual responses of its component pairs as explained in chapter 3.7.1 of National Radio Astronomy Observatory (2024). As the number of antennas in the array increases, the synthesised beam is more accurately approximated by a Gaussian profile as shown in Figure B.3.

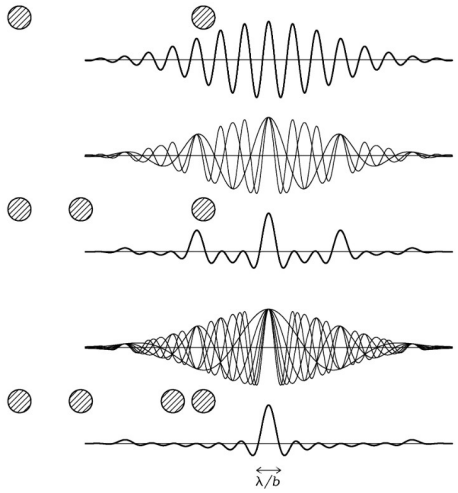

Figure B.3: Point-source responses of interferometric configurations with increasing numbers of antennas, two, three, and four antennas respectively. The synthesised beam approaches a Gaussian profile as additional baselines are added. Credits (National Radio Astronomy Observatory, 2024).

B.2.1 UV-plane and Visibilities

The response of an interferometer is more complex than the simple dish case, and is described by the complex visibility $V(u, v)$:

$$\mathcal{V}(u,v) = \int\int B(x,y)e^{2\pi i(ux+vy)}\,dx\,dy = Ae^{i\phi} \tag{B.1}$$

which is the Fourier transform of the sky brightness distribution $B(x, y)$.

It follows that the sky brightness distribution is the inverse Fourier transform of the complex visibility :

$$B(x,y) = \int\int \mathcal{V}(u,v)e^{-2\pi i(ux+vy)}\,du\,dv. \tag{B.2}$$

The correlator output is therefore a complex number, function of frequency and time, characterized by an amplitude and a phase for each antenna pair; this complex number, $\mathcal{V}$, can be expressed in terms of its amplitude A and phase ϕ, which contain information about the source brightness and its location relative to the phase centre, respectively.

The Fourier space in which visibilities are defined is commonly referred to as the *UV-plane*. In many cases the projected baselines are expressed in units of wavelength. The projected baseline vectors on the Cartesian plane are denoted by the coordinates u and v, while the third axis is chosen along the pointing direction, perpendicular to the direction of the source, and it represents the spatial distribution of projected baselines as seen from the source, measured in units of wavelength.

The coordinates u and v represent the spatial frequency components in the East–West and North–South directions, respectively and they correspond to the projected baseline lengths measured in wavelengths at the time of observation. The coordinates x and y correspond to the angular positions on the sky plane in radian units.

Each baseline corresponds to two symmetric points in the UV-plane, (u, v) and $(-u, -v)$, which are complex conjugates of each other. A single baseline is sensitive to only one spatial frequency, which is one Fourier Transform of the sky brightness distribution, and therefore provides only one visibility measurement. This is insufficient to reconstruct the full brightness distribution, necessitating an increase in the number of sampled baselines.

In addition to increasing the number of antennas, a fundamental method to improve UV coverage is to exploit Earth's rotation: since the projected baseline length changes from the perspective of the source as the Earth rotates, each baseline traces an elliptical arc in the UV-plane. The whole of the sampled points is called the *UV-coverage*, which acts as a sampling function for the sky brightness distribution (analogous to a Dirac comb). Each sampled point corresponds to a measured visibility, and a denser UV coverage improves the quality of the dirty beam; ideally, a uniform UV coverage would produce a perfect image (thorough explanation in Section C.1). The duration of the observation determines the length of the elliptical tracks traced onto the UV-plane.

By measuring the distribution of complex visibilities in the UV-plane, we can reconstruct the sky brightness distribution. An image is obtained through the inverse Fourier transform of the visibilities, where each visibility contributes with a specific amplitude and phase corresponding to emission on a given angular scale. Short baselines are sensitive to large angular-scale structures, while long baselines probe fine-scale structures.

B.2.2 Characteristic scales of a multi-element Interferometer

Regarding the FOV, the individual antenna response limits the extent of an interferometric image made with a single pointing; the HPBW of the primary beam serves as the FOV of the single-pointing interferometric image. If a map size larger than the FWHM of the primary beam is required, multiple pointings in a mosaic pattern must be observed to capture the sky emission.

The synthesized beam structure is more complex compared to single dishes because interferometers are not uniformly illuminated, thus it is not so easy to measure the

FWBN. Instead, the resolution is typically approximated to first order by the FWHM of a Gaussian fit to the central lobe of the beam. The arrangement of interferometer antennas affects the resolution: in a compact configuration, the maximum baseline is smaller and the central beam feature is wide, resulting in low resolution, while in an extended configuration the maximum baseline gives higher resolution since the central beam feature is narrow. So the scale discernible in the image is limited by these maximum baselines.

At first approximation, the angular resolution provided by an interferometer is given by:

$$\theta_{res} = k\lambda/b_{max} \quad \text{[radians]}$$

where k is a factor that depends on how the visibilities are weighted and b_{max} is the longest baseline of the array.

Interferometric observations though have a significant limitation, in that they are insensitive to the emission at large angular scales: this insensitivity occurs because the arrays cannot sample spatial frequencies smaller than those sampled by a baseline equal to an antenna diameter (because we cannot physically "overlap" two antennas). As a result, visibilities at or near the origin of the UV-plane are not sampled, which is known as the *zero-spacing problem* : total flux = zero spatial frequency. That corresponds to baseline = 0 m; interferometers never have a zero baseline. For this reason, an interferometer image has a *maximum recoverable scale*, and it can be computed by:

$$\theta_{mrs} \approx 0.6\lambda/b_{min} \quad \text{[radians]}$$

where b_{min} is the shortest baseline of the array. It is not to be confused with the FOV: the field of view is the size of the sky that is being observed, but inside it, the flux at large scales corresponding to spatial frequencies smaller than b_{min} would be missing.

B.3 Sensitivity

Sensitivity can be defined as the lowest detectable flux by our instrument, with anything below this limit being classified as noise.

The antenna Temperature is a fundamental quantity, defined as the temperature of an ideal resistor whose thermally generated power per unit frequency P_ν is equal to that produced by the antenna

$$T_A = \frac{P_\nu}{k_B} \tag{B.3}$$

with k_B as the Boltzmann constant.

In this context, noise refers to the random fluctuations caused by the variability of a data population, as determined by the root mean square (RMS), which can be estimated using the following formula:

$$\sigma_{RMS} = \frac{2k}{\eta} \frac{T_{sys}}{\sqrt{\Delta t \Delta \nu}\sqrt{N_{ANT}(N_{ANT}-1)A_e}} \tag{B.4}$$

Where k is the Boltzmann constant, η is the instrumental efficiency, ΔT is the total on-source integration time, $\Delta\nu$ is the bandwidth, N_{ANT} the number of antennas and A_e the effective area of each antenna. T_{sys} is the system temperature, which takes into account the effects of the atmosphere on the interferometer, the instrumental component of the receivers and the antenna temperature

T_{sys} is the temperature equivalent to the total noise power received by a telescope (the most important sources of noise are from the receivers and from the atmosphere), and it's given by:

$$T_{sys} \approx \frac{T_{rx} + T_A(sky)}{\eta_{eff} \times exp[-\tau_0 \mathrm{sec} z]} \tag{B.5}$$

Where T_{rx} is the electronic noise and T_A is the antenna-based temperature of the sky which includes contributions from the atmosphere, antenna response and cosmic microwave background (CMB); η_{eff} is the antenna efficiency, related to the antenna gain and its power pattern. The $exp[-\tau_0 \mathrm{sec} z]$ factor represents the fractional transmission of the atmosphere, where τ_0 is equal to the zenith atmospheric opacity and sec z is the zenith secant which gives an estimate of the airmass at transit.

Appendix C

Basic concepts of Radio Imaging

C.1 Imaging

The process of imaging is done by an algorithm called CLEAN and is due to the fact that visibilities do not correspond to an image of the brightness distribution of the source, but its Fourier Transform (FT) as seen in Equation (B.2) and Equation (B.1). Visibilities are complex numbers and in any observation they are a finite amount: for any image the number of points on the uv plane is finite, and so it is not possible to have visibilities that sample fully the FT of an ideal source; we are limited in the uv coverage by the finite number of baselines, the finite time of observation, and the finite number of channels (increasing any of these increases the number of points and so betters the coverage of the uv plane).
So the FT of the finite number of visibilities from the data is not the true, ideal, brightness distribution of the source. The coverage of the uv plane is what is known as the sampling function: it is a function that gives 1 in the points corresponding to where the visibilities can be detected in the uv plane, and 0 everywhere else; the calibrated visibilities then can be thought of as the product between the sampling function and the ideal visibilities. When we compute the Fourier Transform, passing from the real plane to the Fourier plane, a product becomes a convolution, so the result is a convolution between the Dirty Beam (FT of the sampling function, which has a main beam and some side lobes) and the Dirty Image (FT of the real visibilities).

As a consequence, for the reciprocity theorem, we know that the Dirty Image is the convolution between the True Image and the Dirty Beam, therefore in order to recover the true image we have to deconvolve the dirty image (FT transform of the sampled visibilities). This deconvolution is operated by the 'CLEAN' algorithm.

C.1.1 CLEAN algorithm

The 'CLEAN' algorithm, introduced by Högbom (1974); Clark (1980), is the most popular and widely-studied method for reconstructing a model image based on interferometer data.

It iteratively removes at each step a fraction of the flux in the brightest pixel in a defined region of the current "dirty" image, and places this in the model image. It is based on the assumption that an extended source can be represented by a collection

of point sources in an otherwise empty field of view.

It uses an iterative procedure to find the positions and strengths of these sources; at each iteration, the residual image is updated according to (Högbom, 1974; Clark, 1980):

$$I^R(x,y) = I^D(x,y) - \gamma\, B(x,y) * I^C(x,y), \tag{C.1}$$

where:

- $I^R(x,y)$ is the residual image,
- $I^D(x,y)$ is the dirty image,
- γ is the loop gain,
- $B(x,y)$ is the dirty beam,
- $I^C(x,y)$ represents the clean components,
- $*$ denotes convolution.

This operation is repeated for multiple cycles until a stopping criterion (usually a flux threshold) is reached.

After the iterative subtraction process, the final restored image is obtained as

$$I(x,y) = I^C(x,y) * B^I(x,y) + I^R(x,y), \tag{C.2}$$

where:

- $B^I(x,y)$ is the clean beam (typically a Gaussian fit to the main lobe of the dirty beam),
- $I(x,y)$ is the final cleaned image.

The final deconvolved Clean Image is the sum of: the point-source 'clean components' reconvolved, or "restored", with a 'Clean Beam' (which is usually a Gaussian function in order to de-emphasize the higher spatial frequencies), plus a residual image representing differences between the point-source model and the data [1].

$$\text{Clean Image} = \text{Clean Components} * \text{Clean Beam} + \text{Residual Image}. \tag{C.3}$$

The imaging reconstruction algorithm is made of an outer loop of major cycles and an inner loop of minor cycles: the major cycle implements FTs between the data space (uv-plane) and the image space, while the minor cycle operates purely in the image domain. Together, they implement an iterative weighted χ^2 minimization process that solves the measurement equation [2].

[1] `https://www.cv.nrao.edu/~abridle/deconvol/node7.html`

[2] `https://casadocs.readthedocs.io/en/v6.2.0/notebooks/synthesis_imaging.html`

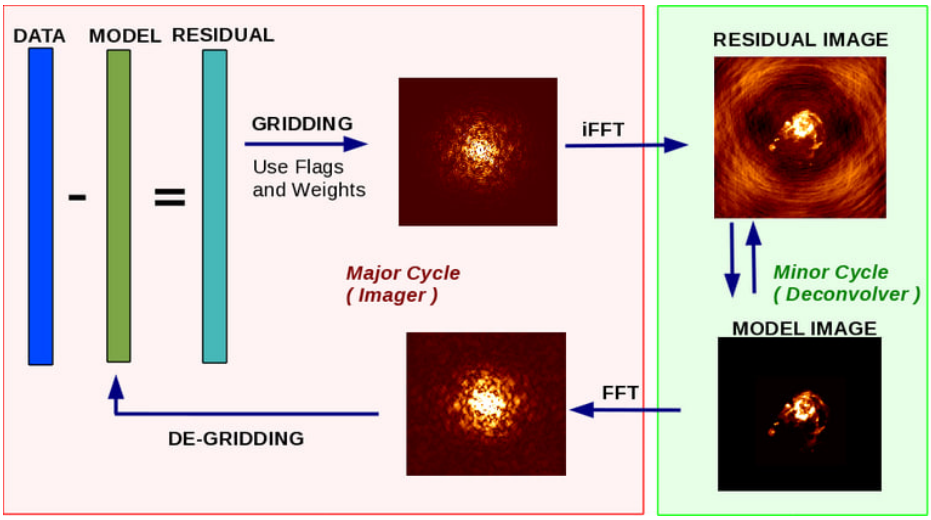

Figure C.1: Minor and major cycles of the imaging reconstruction process of the CLEAN algorithm. Credits: `https://casadocs.readthedocs.io/en/v6.2.0/notebooks/synthesis_imaging.html`

To fully understand the algorithm we describe the procedure step by step qualitatively. As a first step the algorithm takes the dirty image and it identifies for every pixel the peaks of the flux to remove them; it does so by iteratively removing at each step one fraction of those peaks in the region of the dirty image where they were identified and transposing them in the model image, saving their coordinates. The process ends when the residual flux outside the region masked is higher than inside, which means that what's left is just noise. So the dirty image at the end of the iteration is a residual image, while the model image is one composed only by the peaks of the emission and the side-lobes aren't present. The clean beam is therefore the Gaussian that fits the peak of the dirty beam without the lobes.

Parameters

In the `tclean` task is necessary to define some parameters: due to what is known as the Nyquist theorem the cellsize, which is the size of the pixel's side, should be 1/3 or 1/5 of the angular resolution of the dataset, defined as $\theta_{res} \sim \lambda/b_{max}$ (λ is inferred from the central frequency of the observations therefore it is a known value of the dataset listed in the header); the value of the longest baseline can be known from plotting the UV-coverage of the dataset and checking the maximum value.
The angular resolution is connected to the clean beam because the FWHM of the Gaussian that fits the dirty beam *is* the angular resolution of the image. Another parameter that has to be set is the image size, which relates to the Field Of View (FOV) of the instrument: the FOV is defined by the diameter D of the antennas of the radiotelescope (or interferometer), precisely $\theta_{FOV} = \lambda/D$ so the image size must be larger than the FOV in order to cover all the signal, as seen in section B.2.2.
When the instrument is looking at a source larger than the FOV it is possible to use a mosaic of different pointings, with the regions' border slightly overlapping in order to reduce the rms of the image.

The task produces several output files, all named with the prefix given as 'imagename' in the parameter settings.

These include:

- .image: final restored image, with the clean components convolved with a restoring beam and added to the remaining residuals at the end of the imaging process

  .pb: effective response of the telescope (the primary beam)

- T.mask: areas where tclean has been allowed to search for emissions
- .model: sum of all the clean components, which has also been stored as the $MODEL_{DATA}$ column in the measurement set
- .psf: dirty beam, which is being deconvolved from the true sky brightness during the clean process
- .residual: what is left at the end of the deconvolution process; this is useful to diagnose whether or not to clean more deeply
- .weight: image of un-normalized sum of PB-square (for mosaics)
- .sumwt: a single pixel image containing sum of weights per plane

[3]

C.1.2 Weighting

How much weight is attributed to the visibilities affects the resolution and sensibility of the image: during the imaging process, the visibilities can be weighted in different ways to alter the instrument's natural response function. This allows for the improvement of the dynamic range and the ability to adjust the synthesized beam associated with the produced image: the weight of each visibility sample (the 'importance' given to some visibilities with respect to others) can be adjusted to fit the desired output.

The effect on the produced image are several, like improving sensitivity to extended sources or taking into account noise variation between samples. The user can adjust the weighting in the `tclean` procedure by changing the weighting parameter with seven options: 'natural', 'uniform', 'briggs', 'superuniform', 'briggsabs', 'briggsbwtaper', and 'radial'. In this section only some of these will be explained in detail.

- Natural " weighting='natural' ". This weighting scheme provides the maximum imaging sensitivity at the expense of a possibly large beamsize with high sidelobes. It is most appropriate for detection experiments where sensitivity is most important.

  The natural weighting scheme gives equal weight to all samples: since often lower spatial frequencies are sampled more than the higher ones, the inner uv-plane

[3] `https://casaguides.nrao.edu/index.php/VLA_Continuum_Tutorial_3C391-CASA6.4.1`

will have a significantly higher density of samples than the outer uv-plane. The resulting higher density of the inner uv-plane will produce the largest angular resolution and can sometimes result in undesirable structure in the PSF which reduces the accuracy of the minor cycle. However, at the location of a source, this method preserves the natural point-source sensitivity of the instrument.

For weighting='natural', visibilities are weighted only by the data weights, which are calculated during filling and calibration and should be equal to the inverse noise variance on that visibility. Imaging weight w_i of sample i is given by (CASA Documentation Team, Synthesis Imaging):

$$w_i = \omega_i = \frac{1}{\sigma_i^2} \tag{C.4}$$

where the data weight ω_i is determined from σ_i the rms noise on the visibility i. When data is gridded into the same uv-cell for imaging, the weights are summed, and thus a higher uv density results in higher imaging weights. No sub-parameters are linked to this mode choice. It is the default imaging weight mode, and it should produce an "optimum" image with the lowest noise (highest signal-to-noise ratio).
The tradeoff of the high sensitivity is generally the poorest angular resolution of the weighting parameters.

- Uniform weighting='uniform' . This weighting scheme produces a PSF with a narrow main lobe and suppressed sidelobes, but the imaging sensitivity is not as high as with natural weighting. It is most appropriate for imaging experiments where a well-behaved PSF can help the reconstruction.

  Uniform weighting gives equal weight to each measured spatial frequency independently of sample density: the resulting PSF has the narrowest possible main lobe of all the weighting parameters, which means the smallest possible angular resolution, and suppressed sidelobes across the entire image. It is best suited for sources with high signal-to-noise ratios to minimize sidelobe contamination between sources, but the resulting sensitivity is significantly worse (typically a factor $\sim$ 20 worse for a reasonably large number of antenna interferometers), since data points in densely sampled regions have been weighted down to make the weights uniform (CASA Documentation Team, Synthesis Imaging).

  For weighting='uniform', the data weights are calculated as in 'natural' weighting and the the data is gridded to a number of cells and re-weighted to have "uniform" imaging weights: this increases the influence of data with low weights, which sharpens resolution and reduces the sidelobe level in the field-of-view, but increases the rms image noise (CASA Documentation Team, Synthesis Imaging). No sub-parameters are linked to this mode choice. So, as a first step the inverse variance ω_i is gridded for all selected data onto a grid with uv cell-size given by $2/FOV$, so we have gridded weights W_k; then the weight of the $i-th$ sample will be given by (CASA Documentation Team, Synthesis Imaging):

$$w_i = \frac{\omega_i}{W_k}. \tag{C.5}$$

- Briggs weighting "weighting='briggs'". This weighting scheme generates a PSF that can vary smoothly between 'natural' and 'uniform' and allows customized trade-offs between PSF shape and imaging sensitivity by means of the sub-parameter 'robust'.

  Briggs or Robust weighting (Briggs et al., 1995) creates a PSF that smoothly varies between natural and uniform weighting based on the signal-to-noise ratio of the measurements and a tunable parameter that defines a noise threshold called 'robust'; high signal-to-noise samples are weighted by sample density to optimize for angular resolution, and low signal-to-noise data are naturally weighted to optimize for sensitivity.

  This mode is an implementation of the flexible weighting scheme that was originally developed by Dan Briggs in his PhD thesis (Briggs et al., 1995).

  For this weighting scheme, there are two sub-parameters:

  ```
  weighting = 'briggs' Weighting to apply to visibilities
  robust = Briggs robustness parameter
  npixels = number of pixels to determine uv-cell size
  ```

  The actual weighting scheme used is (CASA Documentation Team, Synthesis Imaging):

  $$w_i = \frac{\omega_i}{1 + W_k f^2}. \tag{C.6}$$

  where w_i is the image weight for a given visibility point i; ω_i is the visibility weight for a given visibility point i; $W_k = \sum_{cell} = k\omega_k$ is the weight density of a given cell k (with ω_k the weight of a uv point that falls in cell).
  Then f^2 is a quantity that depends on R the robust sub-parameter (CASA Documentation Team, Synthesis Imaging):

  $$f^2 = \frac{(5 \times 10^{-R})^2}{\frac{\sum_k W_k^2}{\sum_i \omega_i}}. \tag{C.7}$$

  The key parameter is the robust sub-parameter, which sets R in the Briggs equations. The scaling of R is such that $robust = 0$ gives a good trade-off between resolution and sensitivity: the robust R takes a value between -2.0 (close to uniform weighting) to 2.0 (close to natural) (CASA Documentation Team, Synthesis Imaging).

Bibliography

W. I. Axford, E. Leer, and G. Skadron. The acceleration of cosmic rays by shock waves. *International Cosmic Ray Conference*, 11:132, 1977.

A. R. Bell. The acceleration of cosmic rays in shock fronts. i. *Monthly Notices of the Royal Astronomical Society*, 182:147–156, 1978a. doi: 10.1093/mnras/182.2.147.

A. R. Bell. The acceleration of cosmic rays in shock fronts. ii. *Monthly Notices of the Royal Astronomical Society*, 182:443–455, 1978b. doi: 10.1093/mnras/182.3.443.

N. Biava, A. Bonafede, F. Gastaldello, et al. First evidence of a connection between cluster-scale diffuse radio emission in cool-core galaxy clusters and sloshing features. *Astronomy & Astrophysics*, 2024.

R. D. Blandford and J. P. Ostriker. Particle acceleration by astrophysical shocks. *The Astrophysical Journal Letters*, 221:L29–L32, 1978. doi: 10.1086/182658.

Roger Blandford and David Eichler. Particle acceleration at astrophysical shocks: A theory of cosmic ray origin. *Physics Reports*, 154(1):1–75, 1987.

P. Blasi and S. Colafrancesco. Cosmic rays, radio halos and nonthermal x-ray emission in clusters of galaxies. *Astroparticle Physics*, 12:169–183, 1999. doi: 10.1016/S0927-6505(99)00044-6.

A. Bonafede et al. A deep vla study of the galaxy cluster rbs 797. *Monthly Notices of the Royal Astronomical Society*, 418:2234–2245, 2011. doi: 10.1111/j.1365-2966.2011.19630.x.

Annalisa Bonafede, M Gitti, N La Bella, N Biava, F Ubertosi, G Brunetti, G Lusetti, M Brienza, CJ Riseley, C Stuardi, et al. Shock imprints on the radio mini halo in rbs 797. *Astronomy & Astrophysics*, 680:A5, 2023.

Daniel Shenon Briggs et al. New mexico institute of mining technology. *Socorro, New Mexico, USA*, 1995.

G Brunetti, G Setti, L Feretti, and G Giovannini. Particle reacceleration in the coma cluster: radio properties and hard x-ray emission. *Monthly Notices of the Royal Astronomical Society*, 320(3):365–378, 2001.

Gianfranco Brunetti and Thomas W Jones. Cosmic rays in galaxy clusters and their nonthermal emission. *International Journal of Modern Physics D*, 23(04):1430007, 2014.

Jack O Burns. The radio properties of cd galaxies in abell clusters. i-an x-ray selected sample. *Astronomical Journal (ISSN 0004-6256), vol. 99, Jan. 1990, p. 14-30. Research supported by NASA.*, 99:14–30, 1990.

CASA Documentation Team. Synthesis imaging — uv-tapering in casa, 2026a. URL `https://casadocs.readthedocs.io/en/stable/notebooks/synthesis_imaging.html`.

CASA Documentation Team. Synthesis imaging in casa - weighting, 2026b. URL `https://casadocs.readthedocs.io/en/stable/notebooks/synthesis_imaging.html`.

Kenneth W. Cavagnolo, Megan Donahue, G. Mark Voit, and Ming Sun. Intracluster medium entropy profiles for a chandra archival sample of galaxy clusters. *The Astrophysical Journal Supplement Series*, 182:12–32, 2009. doi: 10.1088/0067-0049/182/1/12.

Andrea Cimatti, Filippo Fraternali, and Carlo Nipoti. *Introduction to galaxy formation and evolution: from primordial gas to present-day galaxies.* Cambridge University Press, 2019.

B. G. Clark. An efficient implementation of the algorithm 'clean'. *Astronomy and Astrophysics*, 89:377–378, 1980.

B. Dennison. Formation of radio halos in clusters of galaxies from cosmic-ray protons. *The Astrophysical Journal*, 239:L93–L96, 1980. doi: 10.1086/183297.

Antonaldo Diaferio, S Schindler, and K Dolag. Clusters of galaxies: Setting the stage. *Space Science Reviews*, 134(1):7–24, 2008.

K. Dolag and T. A. Enßlin. Radio halos of galaxy clusters from hadronic secondary electron injection in realistic magnetic field configurations. *Astronomy and Astrophysics*, 362:151–160, 2000.

J. Donnert, K. Dolag, G. Brunetti, R. Cassano, and A. Bonafede. Cluster magnetic fields from galactic outflows and their evolution. *Monthly Notices of the Royal Astronomical Society*, 401:47–54, 2010. doi: 10.1111/j.1365-2966.2009.15621.x.

A. Doria, M. Gitti, S. Ettori, L. Feretti, T. Venturi, and A. C. Fabian. A chandra–vla investigation of the x-ray cavity system and radio mini-halo in the galaxy cluster rbs 797. *The Astrophysical Journal*, 753:47, 2012.

L. O. Drury. An introduction to the theory of diffusive shock acceleration of energetic particles in tenuous plasmas. *Reports on Progress in Physics*, 46:973–1027, 1983. doi: 10.1088/0034-4885/46/8/002.

Dominique Eckert, Massimo Gaspari, Fabio Gastaldello, Amandine MC Le Brun, and Ewan O'Sullivan. Feedback from active galactic nuclei in galaxy groups. *Universe*, 7(5):142, 2021.

T. A. Enßlin and M. Brüggen. On the formation of cluster radio relics. *Monthly Notices of the Royal Astronomical Society*, 331:1011–1019, 2002. doi: 10.1046/j.1365-8711.2002.05235.x.

T. A. Enßlin and Gopal-Krishna. Reviving fossil radio plasma in clusters of galaxies by adiabatic compression in environmental shock waves. *Astronomy and Astrophysics*, 366:26–34, 2001. doi: 10.1051/0004-6361:20000086.

T. A. Enßlin, C. Pfrommer, F. Miniati, and K. Subramanian. Cosmic ray transport in galaxy clusters: implications for radio halos, gamma-ray signatures, and cool core heating. *Astronomy and Astrophysics*, 527:A99, 2011. doi: 10.1051/0004-6361/201015652.

A. C. Fabian. Cooling flows in clusters of galaxies. *Annual Review of Astronomy and Astrophysics*, 32:277–318, 1994a.

A. C. Fabian. Cooling flows in clusters of galaxies. *Annual Review of Astronomy and Astrophysics*, 32:277–318, 1994b. doi: 10.1146/annurev.aa.32.090194.001425.

AC Fabian, PEJ Nulsen, and CR Canizares. Cooling flows in clusters of galaxies. *The Astronomy and Astrophysics Review*, 2(3):191–226, 1991.

Roberto Fanti and Carla Fanti. Una finestra sull'universo invisibile: lezioni di radioastronomia. Lecture notes, Department of Physics and Astronomy, Università di Bologna, 2012.

L. Feretti, G. Giovannini, F. Govoni, and M. Murgia. Clusters of galaxies: Observational properties of the diffuse radio emission. *Astronomy & Astrophysics Review*, 20:54, 2012.

C Ferrari, F Govoni, S Schindler, AM Bykov, and Y Rephaeli. Observations of extended radio emission in clusters. *Space Science Reviews*, 134(1):93–118, 2008.

M Gendron-Marsolais, J Hlavacek-Larrondo, RJ Van Weeren, T Clarke, AC Fabian, HT Intema, GB Taylor, KM Blundell, and JS Sanders. Deep 230–470 mhz vla observations of the mini-halo in the perseus cluster. *Monthly Notices of the Royal Astronomical Society*, 469(4):3872–3880, 2017.

Simona Giacintucci, Maxim Markevitch, Gianfranco Brunetti, John A ZuHone, Tiziana Venturi, Pasquale Mazzotta, and Harve' Bourdin. Mapping the particle acceleration in the cool core of the galaxy cluster rx j1720. 1+ 2638. *The Astrophysical Journal*, 795(1):73, 2014a.

Simona Giacintucci, Maxim Markevitch, Tiziana Venturi, Tracy E Clarke, Rossella Cassano, and Pasquale Mazzotta. New detections of radio minihalos in cool cores of galaxy clusters. *The Astrophysical Journal*, 781(1):9, 2014b.

Simona Giacintucci, Maxim Markevitch, Rossella Cassano, Tiziana Venturi, Tracy E Clarke, and Gianfranco Brunetti. Occurrence of radio minihalos in a mass-limited sample of galaxy clusters. *The Astrophysical Journal*, 841(2):71, 2017.

M. Gitti. Radio mini–halos in galaxy clusters. *Astronomy & Astrophysics*, 593:A13, 2016. or similar review; adjust to your preferred citation.

M. Gitti, C. Ferrari, W. Domainko, L. Feretti, and S. Schindler. Radio mini-halos in galaxy clusters and the cooling flow problem. *Astronomy and Astrophysics*, 470: L25–L28, 2007. doi: 10.1051/0004-6361:20077658.

Myriam Gitti, Gianfranco Brunetti, and Giancarlo Setti. Modeling the interaction between icm and relativistic plasma in cooling flows: The case of the perseus cluster. *Astronomy & Astrophysics*, 386(2):456–463, 2002.

Myriam Gitti, Luigina Feretti, and Sabine Schindler. Multifrequency vla radio observations of the x-ray cavity cluster of galaxies rbs797: evidence of differently oriented jets. *Astronomy & Astrophysics*, 448(3):853–860, 2006.

Myriam Gitti, Fabrizio Brighenti, and Brian R McNamara. Evidence for agn feedback in galaxy clusters and groups. *Advances in Astronomy*, 2012(1):950641, 2012.

F. Govoni and L. Feretti. Magnetic fields in clusters of galaxies. *International Journal of Modern Physics D*, 13:1549–1594, 2004a.

Federica Govoni and Luigina Feretti. Magnetic fields in clusters of galaxies. *International Journal of Modern Physics D*, 13(08):1549–1594, 2004b.

J. A. Högbom. Aperture synthesis with a non-regular distribution of interferometer baselines. *Astronomy and Astrophysics Supplement Series*, 15:417, 1974.

Daniel S Hudson, Rupal Mittal, Thomas H Reiprich, Paul EJ Nulsen, Heinz Andernach, and Craig L Sarazin. What is a cool-core cluster? a detailed analysis of the cores of the x-ray flux-limited hiflugcs cluster sample. *Astronomy & Astrophysics*, 513:A37, 2010.

Alessandro Ignesti, Gianfranco Brunetti, Myriam Gitti, and Simona Giacintucci. Radio and x-ray connection in radio mini-halos: implications for hadronic models. *Astronomy & Astrophysics*, 640:A37, 2020.

Jelle Sjerp Kaastra, Andrei M Bykov, Sabine Schindler, Johannes Alphonsus Marie Bleeker, Stefano Borgani, Antonaldo Diaferio, Klaus Dolag, Florence Durret, Jukka Nevalainen, Tetsuya Ohashi, et al. Clusters of galaxies: beyond the thermal view. *Space Science Reviews*, 134(1):1–6, 2008.

U. Keshet and A. Loeb. Using radio halos and relics to measure the magnetic fields and cosmic-ray content of galaxy clusters. *The Astrophysical Journal*, 722:737–749, 2010. doi: 10.1088/0004-637X/722/1/737.

G. F. Krymskii. A regular mechanism for the acceleration of charged particles on the front of a shock wave. *Soviet Physics Doklady*, 22:327, 1977.

MI Large, DS Mathewson, and CGT Haslam. A high-resolution survey of the coma cluster of galaxies at 408 mc./s. *Nature*, 183(4676):1663–1664, 1959.

J. M. Lotz, A. Koekemoer, D. Coe, et al. The frontier fields: Survey design and initial results. *The Astrophysical Journal*, 837(1):97, 2017. doi: 10.3847/1538-4357/837/1/97.

M. A. Malkov and L. O. Drury. Nonlinear theory of diffusive shock acceleration of particles by shock waves. *Reports on Progress in Physics*, 64:429–481, 2001. doi: 10.1088/0034-4885/64/4/201.

Michael McDonald, Massimo Gaspari, BR McNamara, and GR Tremblay. Revisiting the cooling flow problem in galaxies, groups, and clusters of galaxies. *The Astrophysical Journal*, 858(1):45, 2018.

BR McNamara and PEJ Nulsen. Heating hot atmospheres with active galactic nuclei. *Annu. Rev. Astron. Astrophys.*, 45(1):117–175, 2007.

BR McNamara and PEJ Nulsen. Mechanical feedback from active galactic nuclei in galaxies, groups and clusters. *New journal of physics*, 14(5):055023, 2012.

Elinor Medezinski, Keiichi Umetsu, Nobuhiro Okabe, Mario Nonino, Sandor Molnar, Richard Massey, Renato Dupke, and Julian Merten. Frontier fields: Subaru weak-lensing analysis of the merging galaxy cluster a2744. *The Astrophysical Journal*, 817 (1):24, 2016.

J. Merten, D. Coe, R. Dupke, et al. Creation of cosmic structure in the complex galaxy cluster merger abell 2744. *Monthly Notices of the Royal Astronomical Society*, 417 (1):333–347, 2011. doi: 10.1111/j.1365-2966.2011.19286.x.

F. Miniati, D. Ryu, H. Kang, and T. W. Jones. Cosmic-ray protons accelerated at cosmological shocks and their impact on clusters of galaxies. *The Astrophysical Journal*, 559:59–69, 2001. doi: 10.1086/322363.

M Murgia, F Govoni, M Markevitch, L Feretti, Gabriele Giovannini, GB Taylor, and E Carretti. Comparative analysis of the diffuse radio emission in the galaxy clusters a1835, a2029, and ophiuchus. *Astronomy & Astrophysics*, 499(3):679–695, 2009.

Matteo Murgia, Dominique Eckert, Federica Govoni, Chiara Ferrari, M Pandey-Pommier, J Nevalainen, and S Paltani. Gmrt observations of the ophiuchus galaxy cluster. *Astronomy & Astrophysics*, 514:A76, 2010.

National Radio Astronomy Observatory. Vla tutorial, a. URL `https://casaguides.nrao.edu/index.php/VLA_Continuum_Tutorial_3C391-CASA6.4.1`.

National Radio Astronomy Observatory. Casa guides, b. URL `https://casadocs.readthedocs.io/en/v6.5.4/api/tt/casatasks.imaging.tclean.html`.

National Radio Astronomy Observatory. Casa: Common astronomy software applications, c. URL `https://casa.nrao.edu/`.

National Radio Astronomy Observatory. The vla observational status summary, 2014. URL `https://science.nrao.edu/facilities/vla/docs/manuals/oss2014B/intro/overview`.

National Radio Astronomy Observatory. Essential radio astronomy, 2024. URL `https://science.nrao.edu/opportunities/courses/era/`.

E. Osinga et al. The lofar two-metre sky survey: Deep learning for radio galaxy classification. *Astronomy & Astrophysics*, 665:A71, 2022. doi: 10.1051/0004-6361/202142577.

A. G. Pacholczyk. *Radio Astrophysics: Nonthermal Processes in Galactic and Extragalactic Sources*. W. H. Freeman and Company, San Francisco, 1970.

P Parma, M Murgia, R Morganti, A Capetti, HR De Ruiter, and R Fanti. Radiative ages in a representative sample of low luminosity radio galaxies. *arXiv preprint astro-ph/9812413*, 1998.

CJJ Pearce, RJ Van Weeren, F Andrade-Santos, C Jones, WR Forman, M Brüggen, E Bulbul, TE Clarke, RP Kraft, E Medezinski, et al. Vla radio observations of the hst frontier fields cluster abell 2744: The discovery of new radio relics. *The Astrophysical Journal*, 845(1):81, 2017.

Chien Y Peng, Luis C Ho, Chris D Impey, and Hans-Walter Rix. Detailed structural decomposition of galaxy images. *The Astronomical Journal*, 124(1):266–293, 2002.

John R Peterson and Andrew Christopher Fabian. X-ray spectroscopy of cooling clusters. *Physics reports*, 427(1):1–39, 2006.

V. Petrosian. On the nonthermal emission and acceleration of electrons in clusters of galaxies. *The Astrophysical Journal*, 557:560–572, 2001. doi: 10.1086/322243.

Christoph Pfrommer and Torsten A Ensslin. Constraining the population of cosmic ray protons in cooling flow clusters with γ-ray and radio observations: Are radio mini-halos of hadronic origin? *Astronomy & Astrophysics*, 413(1):17–36, 2004.

A Richard-Laferrière, J Hlavacek-Larrondo, RS Nemmen, CL Rhea, GB Taylor, M Prasow-Émond, M Gendron-Marsolais, M Latulippe, AC Edge, AC Fabian, et al. On the relation between mini-halos and agn feedback in clusters of galaxies. *Monthly Notices of the Royal Astronomical Society*, 499(2):2934–2958, 2020.

CJ Riseley, K Rajpurohit, F Loi, A Botteon, R Timmerman, N Biava, A Bonafede, E Bonnassieux, G Brunetti, T Enßlin, et al. A meerkat-meets-lofar study of ms 1455.0+ 2232: a 590 kiloparsec 'mini'-halo in a sloshing cool-core cluster. *Monthly Notices of the Royal Astronomical Society*, 512(3):4210–4230, 2022.

Kristen Rohlfs and Thomas L Wilson. *Tools of radio astronomy*. Springer Science & Business Media, 2013.

B. Sander, A. Schwope, G. Lamer, T. H. Reiprich, J. Kohnert, and R. Fassbender. The rosat bright survey: Ii. catalogue of all high-galactic latitude rass sources with pspc countrate cr ¿ 0.2 s1. *Astronomy & Astrophysics*, 536:A83, 2011. doi: 10.1051/0004-6361/201116429.

Craig L Sarazin. X-ray emission from clusters of galaxies. *Reviews of Modern Physics*, 58(1):1, 1986.

Federica Savini, Annalisa Bonafede, Marcus Brüggen, David Rafferty, Timothy Shimwell, Andrea Botteon, Gianfranco Brunetti, Huib Intema, Amanda Wilber, Rossella Cassano, et al. A lofar study of non-merging massive galaxy clusters. *Astronomy & Astrophysics*, 622:A24, 2019.

S. Schindler et al. Discovery of holes in the x-ray emission of the galaxy cluster rbs 797. *Astronomy & Astrophysics*, 376:L27–L30, 2001.

R. Schlickeiser and U. Achatz. Cosmic-ray transport and acceleration. ii. cosmic rays in galaxy clusters. *Journal of Plasma Physics*, 49:63–86, 1993. doi: 10.1017/S0022377800026782.

R. Schlickeiser, A. Sievers, and H. Thiemann. A stochastic acceleration model for the radio halo in the coma cluster of galaxies. *Astronomy and Astrophysics*, 182:21–30, 1987.

D. Sijbring. *A radio continuum study of cooling flow clusters of galaxies*. PhD thesis, University of Groningen, 1993.

Woodruff Turner Sullivan. *The early years of radio astronomy: Reflections fifty years after Jansky's discovery*. Cambridge University Press, 2004.

R. S. Sutherland and M. A. Dopita. Cooling functions for low-density astrophysical plasmas. *Astrophysical Journal Supplement Series*, 88:253–327, 1993.

G. B. Taylor, A. C. Fabian, and S. W. Allen. The radio source in the cooling core cluster rbs 797. *Monthly Notices of the Royal Astronomical Society*, 334:769–776, 2002. doi: 10.1046/j.1365-8711.2002.05574.x.

A. R. Thompson, J. M. Moran, and G. W. Swenson. *Interferometry and Synthesis in Radio Astronomy*. Springer, 3rd edition, 2017.

F Ubertosi, M Gitti, F Brighenti, M McDonald, P Nulsen, M Donahue, G Brunetti, S Randall, M Gaspari, S Ettori, et al. Multiple shock fronts in rbs 797: the chandra window on shock heating in galaxy clusters. *The Astrophysical Journal*, 944(2):216, 2023.

F Ubertosi, M Giroletti, M Gitti, N Biava, E De Rubeis, A Bonafede, L Feretti, M Bondi, L Bruno, E Liuzzo, et al. A jvla, lofar, e-merlin, vlba, and evn study of rbs 797: can binary supermassive black holes explain the outburst history of the central radio galaxy? *Astronomy & Astrophysics*, 688:A86, 2024.

Francesco Ubertosi, Myriam Gitti, Fabrizio Brighenti, Gianfranco Brunetti, Michael McDonald, Paul Nulsen, Brian McNamara, Scott Randall, William Forman, Megan Donahue, et al. The deepest chandra view of rbs 797: evidence for two pairs of equidistant x-ray cavities. *The Astrophysical Journal Letters*, 923(2):L25, 2021.

V. Vacca, M. Murgia, F. Govoni, et al. The mini-halo in the galaxy cluster rbs 797. *Astronomy & Astrophysics*, 540:A38, 2012. doi: 10.1051/0004-6361/201118534.

V. Vacca, M. Murgia, F. Govoni, and et al. The radio halo in abell 2256: spectral index and magnetic field properties. *Astronomy & Astrophysics*, 561:A52, 2014. doi: 10.1051/0004-6361/201322810.

R. J. van Weeren, G. Brunetti, M. Brüggen, and et al. Lofar observations of diffuse radio emission in galaxy clusters. *The Astrophysical Journal*, 818:204, 2016. doi: 10.3847/0004-637X/818/2/204.

R. J. van Weeren, F. de Gasperin, H. Akamatsu, M. Brüggen, L. Feretti, H. Kang, A. Stroe, and F. Zandanel. Diffuse radio emission from galaxy clusters. *Space Science Reviews*, 215:16, 2019.

RJ Van Weeren, F De Gasperin, H Akamatsu, Marcus Brüggen, L Feretti, H Kang, A Stroe, and F Zandanel. Diffuse radio emission from galaxy clusters. *Space Science Reviews*, 215(1):16, 2019.

T. Venturi, S. Giacintucci, G. Brunetti, R. Cassano, D. Dallacasa, and G. Setti. Gmrt radio halo survey in galaxy clusters at z = 0.2–0.4. i. the reflex sub-sample. *Astronomy & Astrophysics*, 484:327–340, 2008. doi: 10.1051/0004-6361:20079198.

J. A. ZuHone, M. Markevitch, G. Brunetti, and S. Giacintucci. Turbulent reacceleration of relativistic electrons in simulations of sloshing galaxy cluster cores. *The Astrophysical Journal*, 762:78, 2013. doi: 10.1088/0004-637X/762/2/78.

J. A. ZuHone, M. Markevitch, G. Brunetti, and S. Giacintucci. Radio minihalos in sloshing galaxy cluster cores: Effects of magnetic field amplification. *The Astrophysical Journal*, 798:90, 2015. doi: 10.1088/0004-637X/798/2/90.

V. Zúñiga, N. Haridas, A. T. Erdogan, and T. Arslan. Effect of a central antenna element on the directivity, half-power beamwidth and side-lobe level of circular antenna arrays. In *Proceedings of the 2009 NASA/ESA Conference on Adaptive Hardware and Systems*, pages 252–256. IEEE, 2009.